Theoretical Investigation of H_2 Generation Systems: From Homogenous to Heterogeneous Photo-Catalysis

---

Dissertation

zur

Erlangung der naturwissenschaftlichen Doktorwürde
(Dr. sc. nat.)

vorgelegt der

Mathematisch-naturwissenschaftlichen Fakultät

der

Universität Zürich

von

Yeliz Gürdal-Durğun

aus der

Türkei

Promotionskommission

Prof. Dr. Jürg Hutter (Vorsitz und Leitung)

Dr. Marcella Mauri-Iannuzzi

Prof. Dr. Peter Hamm

Zürich, 2017

How wonderful that we have met with a paradox. Now we have some hope of making progress.

Niels Bohr

Abstract

In the quest of renewable sources of energy one of the most promising solution is the production of molecular hydrogen from water activated by solar energy. The photo-induced reactive cycle to split water and generate H_2 with a clean and sustainable process relies on the choice of efficient photo-catalysts for both the oxidation and the reduction steps. Recent studies revealed that molecules with Cobalt (Co) active centers might achieve a commercially reasonable efficiency in reducing water, thus being candidates for the replacement of expensive transition metals, such as Platinum and Ruthenium. In this respect, we investigate H_2 production systems based on Co centered poly-pyridyl complexes in homogeneous and heterogeneous environments using density functional theory and ab-initio molecular dynamics.

Concerning the homogeneous catalysis, we explore a few differently ligated Co-based catalysts immersed in water solution. The emphasis is on the effects of structural features, i.e. the number of the pyridyl subunits, flexibility of the ligands, and coordination sphere around Co to understand the role of these structural features on the catalysts activity towards H_2 production. Heterogeneous systems, instead, are grouped in two sections: oxide and metal surfaces where the Co-based water reduction catalysts are immobilized. The adsorption of both the bare ligand and the Co-metalated poly-pyridyl complexes and their assemblies on stoichiometric rutile TiO_2(110) and reconstructed Au(111) surfaces are investigated. The optimized adsorption geometries, the effects of Co insertion on the stability, molecule/surface and intermolecular interactions, electronic properties, their potential usage as H_2 production systems are discussed for the two cases. In the case of Au(111) surface, we also address the role of herringbone reconstruction on the adsorption strength and on the modification of the molecular properties. Besides, rearrangements within the monolayer upon metalation and the possible intermediate states that hinder the metalation process are investigated.

Zusammenfassung

Einer der vielversprechendsten Lösungsansätze zur Erschliessung erneuerbarer Energiequellen stellt die Gewinnung von molekularem Wasserstoff aus Wasser mit der Hilfe von Sonnenenergie dar. Um Wasser mittels eines photoneninduzierten Prozesses zu spalten ist ein Katalysator notwendig. Die Nachhaltigkeit dieses Prozesses hängt stark von der Effizienz ab, mit welcher der Katalysator die verschiedenen Oxidations- und Reduktions-Schritte katalysiert. Aktuellen Studien haben gezeigt, dass Wasserreduktions Katalysatoren bei welchen Kobalt-Ionen das reaktive Zentrum bilden das Potential haben eine kommerziell relevante katalytische Effizienz zu erreichen. Somit stellen Kobalt-Katalysatoren möglicherweise eine Alternative zu den teuren Platin- und Ruthenium-Katalysatoren dar. In dieser Arbeit haben wir Kobalt-Poly-Pyridyl Katalysatoren zur Wasserreduktion in homogener und heterogener Umgebung mittels Dichte Funktional Theorie und ab-initio Molekulardynamik untersucht.

Die homogene Katalyse haben wir am Beispiel verschiedener Kobalt-Katalysatoren in wässriger Lösung studiert. Dabei haben wir uns insbesondere auf den Einfluss struktureller Eigenschaften wie die Anzahl koordinierender Pyridin-Substituenten, die Flexibilität des Liganden, sowie Änderungen der Koordinationssphäre des Kobalt-Zentrums auf die katalytische Aktivität fokussiert. Im Kontext der heterogenen Katalyse haben wir auf Metalloxiden oder Metalloberflächen immobilisierte Kobalt-Katalysatoren untersucht. Wir haben sowohl das Adsorptionsverhalten des nicht an Kobalt koordinierten Poly-Pyridyl-Liganden als auch des Kobalt-Komplexes auf Rutile TiO_2(110) und oberflächenrekonstruiertem Au(111) ausführlich studiert. In beiden Fällen haben wir die adsorbierten Molekülstrukturen, den stabilisierenden Effekt eines an Kobalt koordinierten Liganden, und sowohl die Molekül-Oberflächen als auch die intermolekularen Interaktionen diskutiert. Des Weiteren haben wir auch die elektronischen Eigenschaften der Systeme beschrieben, sowie ihre mögliche Verwendung zur Wasserstoff-Gewinnung. Für die Gold Au(111) Oberfläche haben wir den Einfluss der "Herringbone" Oberflächenrekonstruktion auf das Adsorptionsverhalten sowie auf die molekularen Eigenschaften der Katalysatoren analysiert. Des Weiteren haben wir die Neuanordnung innerhalb einer Monolage als Folge der Koordination des Liganden an Kobalt-Ionen untersucht. Dabei haben wir mögliche Zwischenprodukte identifiziert welche die Koordination des Liganden an Kobalt-Ionen einschränken.

Acknowledgements

I would like to express my deepest gratitude to my supervisor Prof. Jürg Hutter for the valuable advise, guidance, and insightful discussion. Thanks to him I had a chance to involve in the discussion of both code development and its applications which is, in my opinion, a great luck for a PhD student working on theoretical simulations. I appreciate Dr. Marcella Iannuzzi who has been an outstanding advisor, highly gifted teacher, a perfect role model, and a pleasant office-mate. I would like to thank to CP2K group members who have always provided a pleasant working environment. I am especially thankful to Mauro Schilling and Tiziano Müller for their help in German, and Dr. Andreas Glöss for his technical support.

During my PhD I have involved in a connective research project which has provided many experimental collaborators. I am thankful to Dr. Gerson Mette, Prof. Jürg Osterwalder, Dr. Benjamin Probst, and Prof. Roger Alberto. Thanks to their enthusiasm to work collaboratively and exchange ideas I had a chance to connect the results of my simulations to real life applications. I appreciate Prof. Peter Hamm for being a committee member and reviewing my thesis.

I appreciate financial support provided by University Research Priority Program LightChEC of the University of Zurich and the National Centers of Competence in Research– Materials Revolution: Computational Design and Discovery of Novel Materials (NCCR–MARVEL). The computing resources from the Swiss National Supercomputer Center (CSCS) under the project ID s425 and Partnership for Advanced Computing in Europe (PRACE) Marconi resource based in Italy are acknowledged.

I appreciate all my friends who shared with me the ups and downs of life as a PhD student. I am especially thankful to Dr. Noelia Fuentes Romero, Dr. Patricia García Domínguez, and Sevgi Uzungeliş. Their warm and embracing friendship always make me feel at home.

I will be always indebted to my beloved family Ziya, Şükran, Cengiz, and Gülsüm Gürdal for their endless support. I am thankful to my dearest friend Dr. Yilmaz Durğun whose presence has brought my life an extra dimension beyond the words. Thank you Yilmaz for always believing in me.

Publications

1. Y. Gurdal, S. Luber, J. Hutter, M. Iannuzzi. Non-innocent adsorption of Co-pyrphyrin on rutile(110). Physical Chemistry Chemical Physics 2015, 17, 22846–22854.

2. G. Mette, D. Sutter, Y. Gurdal, S. Schnidrig, B. Probst, M. Iannuzzi, J. Hutter, R. Alberto, J. Osterwalder. From porphyrins to pyrphyrins: Adsorption study and metalation of a molecular catalyst on Au(111). Nanoscale 2016, 8, 7958–7968.

3. Y. Gurdal, M. Iannuzzi. DFT–based theoretical simulations for photo-catalytic applications using TiO_2. In *Titanium Dioxide*, Editor: M. Janus, INTECH Publishing, accepted, 2017.

4. Y. Gurdal, J. Hutter, M. Iannuzzi. Insight into (Co)Pyrphyrin adsorption on Au(111): The effects of herringbone reconstruction and dynamics of metalation. The Journal of Physical Chemistry C 2017, 121, 11416–11427.

5. M. Graf, G. Mette, D. Leuenberger, Y. Gurdal, M. Iannuzzi, W.-D. Zabka, S. Schnidrig, B. Probst, J. Hutter, R. Alberto, J. Osterwalder. The impact of metalation on adsorption geometry, electronic level alignment and UV-stability of organic macrocycles on TiO_2(110). Nanoscale 2017, 9, 8756–8763.

6. Y. Gurdal, J. Hutter, M. Iannuzzi. How coordination pocket and ligand type affect the water reduction mechanism of Cobalt-based polypyridyl catalysts. In preparation.

Contents

1 Introduction

In the quest for renewable energy sources molecular hydrogen is one of the most favored candidate as energy carrier. Compared to other means, such as electricity, bio-fuels, or conventional fuels, hydrogen has the highest specific energy content [1], and is also environmentally preferable, because the waste product of its reaction with pure oxygen is simply water [2]. However, the large scale production and storage of molecular hydrogen is still an open issue. Several techniques can be employed for its production, such as water electrolysis [3], steam and ethanol reforming [4, 5], partial oxidation of hydrocarbons [6], dark fermentation [7], and photo-chemical water splitting [8]. The latter is of particular interest, because it emulates the photo-chemical process by absorbing photons in the energy range between 1.5 and 3.3 eV (visible spectrum). The resulting product of water splitting, H_2, has zero emission and high energy density, therefore being a highly promising candidate for replacing traditional fuels which are responsible for 90% of all CO_2 emissions. In order to decrease the demand in fossil fuels and their environmental impacts, we aim at investigating promising water splitting catalysts that can employ the easily available sunlight and convert it into chemical energy.

Photo-chemical water splitting consists of two half reactions, namely water reduction, which is also known as proton reduction and water oxidation. Overall, two water molecules are converted to one O_2 and two H_2 molecules. Since water splitting is a complex and challenging process, current research mostly focuses on half reactions, either water reduction or water oxidation. The central theme of this thesis is investigating water reduction systems from homogenous to heterogeneous catalysts towards photo-catalytic H_2 production.

Photo-catalytic water reduction can be achieved through either homogeneous or heterogeneous catalysts which have their own specific advantages and disadvantages. Considering homogeneous catalysts, which have been widely studied [9], most of the working systems uses expensive transition metals as catalytic reduction centers, such as Pt [10]. However, one has to search for alternatives of the expensive catalytic

centers to facilitate commercial implementation of the water reduction systems. The proposed cheap transition metal-based catalysts should have high turnover numbers and frequencies together with low over-potential.

It has been shown that cheap Co-based catalysts can be employed for H_2 production with low over-potentials [11]. Several Co deposited catalysts, such as porphyrin-derived molecules [12], cobaloximes [13], pyrphyrins [14], and molecules with polypyridine ligands [15], have been used for hydrogen evolution in homogeneous environment. Peters et al. [16] investigated catalytic activity of several cobalt complexes with BF_2 giglyoxime or propane bridged tetraimine ligands in acetonitrile. They concluded that with less electron donating ligands, reduction of Co-complexes can be achieved easily, leading to H_2 production. Guttentag et al. [15] studied the activity of $[Co^{III}Br_2(DO)(DOH)pn]$ with photo-sensitizer $[Re(CO)_3(bipy)(py)]^+$ in pure water and acidic environment, demonstrating that H_2 production is possible without organic solvents. Solis et al. [17] modeled several cobalt hangman porphyrins in acetonitrile solution and determined the pathway for proton coupled electron transfer for H_2 generation. Recently, several reviews on homogeneous water reduction has been published [18–21].

Among many ligand types, polypyridyl ligands have gained particular attention in literature due to their high stability and strong ligand field achieved with Co. It has been shown that polypyridyl ligands are superior to cobaloximes in terms of their higher photo-catalytic activity and stability [22, 23]. Several Co-based pentapyridyl-ligand catalysts have been screened by comparing the activities of molecules with an almost perfect octahedral arrangement and molecules with strongly distorted octahedral pockets [14, 24, 25]. Results showed that by breaking the symmetry around the metal center the activity is enhanced. Other studies also discuss the role of the distortion of the local environment and of the orientation of the ligands around the metallic center [24, 26, 27]. On the other hand, due to the complexity of water reduction reaction, there are limited spectroscopic investigations covering all the steps, from the initial catalyst's reduction to the H_2 release. Hence, theoretical investigations of the number of the pyridyl subunits, the polypyridyl and bipydiyl ligand structures, the distortion of the ligands, and also the coordination sphere around the Co center and how these features affect the water reduction mechanism and intermediate products is crucial in designing promising homogeneous water reduction catalyst. Therefore, Chapter 4 in this thesis is dedicated to exploring the effects of ligand type

and coordination environment around Co center on the water reduction mechanism of pentapyridyl and tetrapyridyl Co-complexes in water solution.

In spite of the established achievements in H_2 generation using metal complexes in homogeneous environments, the drawback is the rapid recombination of photo-generated products in solution [28]. Therefore, it has been proposed that in heterogeneous environments, where the photo-catalyst is combined with a supporting material, the back electron transfer can be prevented and the system and reaction intermediates are stabilized [29]. It is therefore of interest to study the adsorption behavior of these metal complexes on well defined surfaces, and to explore whether their catalytic activity and stability are preserved in the adsorbed state. We will mention the on-going studies on heterogeneous water reduction catalysts (WRC) in two subsections: immobilization of WRC on semiconductors, where TiO_2 will be discussed as a model system, and on metal surfaces, where the Au(111) surface will be under consideration.

Already in 1938 the first study of Goodeve et al. [30] demonstrated the photo-catalytic activity of the TiO_2 surface, which can produce oxygen by absorbing UV light thus leading to the photo-bleaching of dyes. This study has initiated many others towards discovering photo-catalytic reactions that can be catalyzed by TiO_2. The success of this material is also justified by its high stability, low cost, no side effects on humans and environment, and ease in large-scale usage. In 1972 Fujishima and Honda [31] carried out the successful and inspiring experiment of water splitting using TiO_2 as photo-anode. In a closed circuit photo-electrochemical cell, photo-generated electron and hole pairs move to TiO_2 surface, where water molecules are oxidized to generate O_2, while the protons are combined with electrons at the cathode, Pt, to generate H_2. In spite of the promising properties of TiO_2, the photo-catalytic activity of the bare surface is not optimal, due to the too large energy gap [32]. This limits the photons' absorption and induces the fast recombination of the photo-generated carriers [33]. While these drawbacks significantly hinder the effective application of the pristine material, several possible solutions have been envisioned by considering surface modifications, such as composite semiconductor coupling, metal/non-metal doping, and functionalization by means of different types of adsorbates [34, 35]. For instance, Zn-Porphyrin adsorbed on the TiO_2 surface reduces the threshold for the photons' absorption, and by allowing the fast electron injection towards the substrate, slows down the charge recombination process [36].

As alternative to the photo-electrochemical cells proposed by Fujishima and Honda [31], two other widely explored methods of water splitting using TiO_2 have been developed.

One method uses TiO_2 nanoparticles on which a transition metal (e.g. Pt) and another oxide (e.g. RuO_2) are deposited (see Figure 1.1-(a)). In this way, the photon absorption is followed by an efficient charge separation: the electrons are transported to the metal and activate the recombination of protons into H_2 molecules, whereas the holes move to the coupled oxide, favoring the O_2 evolution. This design results in substantial decrease in over-potential of the reaction [37]. The second approach employs sacrificial agents to remove one of the photo-generated charge carrier. An illustration is shown in Figure 1.1-(b), where CH_3OH is used as a sacrificial specie. While photo-generated holes are injected into CH_3OH, which afterwards oxidizes water, excited electrons in TiO_2 conduction band (CB) reduces water to H_2 [37]. This system focuses on half reactions, either water reduction via sacrificial electron donor or water oxidation via sacrificial electron acceptor [38].

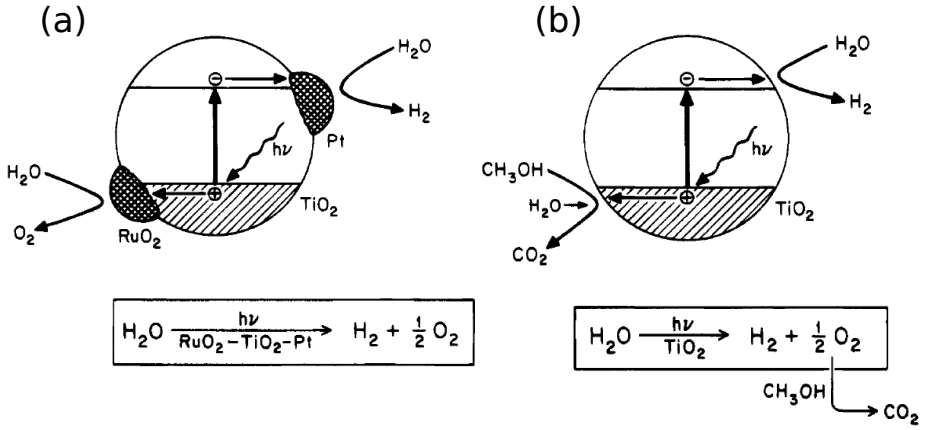

Figure 1.1: (a) Photosplitting of water on composite catalyst. (b) Photosplitting of water: sacrificial donor effect. Reprinted with the permission from Ref. [37] Copyright (1995) American Chemical Society.

Prior to reviewing theoretical studies of water reduction on functionalized TiO_2 surfaces, it is useful to give a closer examination of the interactions between water molecules and the bare TiO_2 surface. It is shown that water molecules prefers to adsorb on oxygen vacancies of the rutile(110) surface [39]. Water adsorption is followed by a proton transfer to the adjacent two-coordinated surface oxygen thus leading to a formation of hydroxy radical on the surface [40]. Zhao [41] calculated adsorption and decomposition energies of water molecules on different rutile surfaces, such as (110), (100), and (001) using Density Functional Theory (DFT). While dissociative adsorption of water is more favorable on (110) surface, the activation energy of the water dissociation is largest on the (100) surface. Calculations by Hahn et al. [42]

showed that the employed adsorbate coverage affects the adsorption geometry and the stability of the the adsorbed water molecules. While at low coverage water molecules tend to dissociate on rutile(110) surface, increasing coverage leads to an associative adsorption. Investigating the interactions between water and bare TiO_2 surface is a fundamental research, however in order to reach efficiencies that are of any interest with respect to realistic devices, it is essential at least to operate with functionalized surfaces.

The band gap of TiO_2 can be modified by metal/ametal deposition. Systems containing Fe, Al, Si, and F deposited on the surface of rutile and anatase have been modeled and characterized by electronic structure calculations (DFT) [43]. These studies show that, while the cationic dopants at the Ti lattice sites stabilize anatase slightly more than rutile, anionic doping with F has the opposite effect. Modeling Pt, Ru, and Co ions doped anatase TiO_2(001) surface shows that the band gap of the complexes decrease by 1.8 eV with Co, 1.7 eV with Ru, and 0.4 eV with Pt [44]. By growing Ru clusters on the anatase(101) surface, instead, not only a significant decrease of the local band gap is observed, but also electrons accumulate at the metal/oxide interface, due to the electron flow from Ru to TiO_2 [45].

There are also other studies which focus on designing water splitting systems by mixing TiO_2 with another metal oxide. Graciani et al. [46] modeled water adsorption on Ce_2O_3 doped rutile TiO_2(110) surface. They show that the proposed mixed-metal oxide has a promising ability to dissociate water exposing an exothermic dissociation energy of -0.7 eV with a small activation barrier of 0.04 eV. A relatively larger system is investigated by Pastore and De Angelis [47] who modeled a TiO_2/Ru-dye/IrO_2 complex using DFT. In the designed complex, Ru polypyridyl dye, acting as a linker between the oxides, is attached to both anatase TiO_2(101) and IrO_2 surfaces via phosphonic acid and malonate groups, respectively. The electronic structure analysis shows that both highest occupied molecular orbital (homo) and lowest unoccupied molecular orbital (lumo) are located on the IrO_2 showing a metallic-like character. While occupied molecular orbitals of the dye are located within the IrO_2 valence band (VB), its unoccupied orbitals are distributed over the CB of both IrO_2 and TiO_2.

A promising design for an heterogeneous water reduction devise seems to be obtained by adsorbing a macrocyclic water reduction catalysts on the TiO_2 surface together with a proper photo-sensitizers. Only relatively few studies on the combination of Co-catalysts with TiO_2 surface have been published. One example is the Co-based complex [Co^{III}(dmgH)$_2$(pyridyl-4-hydrophosphonate)Cl] which can be adsorbed by

means of some anchoring groups and it is active as proton reduction catalyst [48]. Yin et al. [49] studied the organic dye eosin Y (EY) and several other Co complexes also adsorbed on the TiO_2 surface through different anchoring groups. They concluded that TiO_2 is able to harvest electrons from the excited EY molecules, thus generating long-lived charge-separated states, which eventually lead to the electron transfer to the Co-catalyst and the reduction process. A similar reductive pathway has also been observed by Lakadamyali et al. [50], who studied the co-adsorption of the CoP catalyst and a ruthenium dye RuP on TiO_2. The photo-excitation of RuP induces an electron injection into the conduction band of TiO_2. The photo-electrons are then transferred to CoP, where the H_2 formation occurs. The photo-excitation of Co(I)-porphyrin on TiO_2 in acetonitrile-pyridine solution has also been studied [51], showing that after the rapid electron injection from Co to TiO_2 and the coordination of pyridine to Co, the undesired charge recombination is significantly slowed down. Monti et al. [52] proposed a model system of Ru-based catalyst/antenna/TiO_2 complex for water splitting and investigated proton coupled electron transfer dynamics of the catalyst in water solution using Ab-Initio Molecular Dynamics (AIMD). Results show that a water molecule binds to Ru center and after 1.9 ps of simulation time proton transfer from attached water molecule to the closest one in the solution is achieved. Several studies are already available on the properties of metal centered porphyrins adsorbed on TiO_2 surfaces [34, 36, 53].

The porphyrin derived tetra-aza macro-cycle, constituted of four pyridine rings, is named pyrphyrin (Pyr) but also known as Ogawa porphyrin like ligand. Pyr has been introduced first by Ogawa et al. [54] in 1984. Later, alkylated pyrphyrin has also been synthesized and its optical properties have been characterized [55]. More recently, metal-centered pyrphyrins have been studied both experimentally and theoretically to determine their UV-visible spectra in solution [56–58]. Co centered pyrphyrin (CoPyr) has been recently synthesized and successfully used as water reduction catalyst in homogeneous environment [14]. Although, there are many studies on Pyr molecules in homogeneous environment there is no research carried out so far on the interactions between Pyr and solid surfaces. Exploring the potential of Pyr adsorbed on TiO_2 surface might provide useful insight for the design of new, promising, and feasible photo-catalysts for water reduction. Therefore, one of the chapter in this thesis, Chapter 5, is dedicated to the investigation of Pyr and CoPyr interactions with TiO_2 surface.

Metal surfaces are also extremely important in designing photo-catalysts towards H_2 production. Two dimensional regular monolayers of molecules at metal surfaces might result in molecular architectures with tailored topological, electronic, optical, magnetic or catalytic properties. In particular, the interactions of porphyrin molecules with metal surfaces and the formation of self-assembled monolayer have been intensively studied [59–61]. Yokoyama et al. [62] observed that porphyrin molecules adsorbed on Au(111) can form supermolecular structures, as trimers and tetramers, depending on the positions of the cyano substituents. Other recent studies [63] focused on the coordination self assembly and metalation of tetra-porphyrin with Cu on Au(111) surface. While some of the Cu atoms link two pyridyl groups of neighboring molecules, others coordinate to the porphyrin's macrocycle and lead to metalation. Mielke et al. [64], instead, showed the formation of coordination bonds between native Au adatoms and tetraphenylporphyrins. Recently, Hulsken et al. [65] performed a mechanistic study of oxidation catalysis by monitoring individual manganese porphyrin catalysts on a Au(111) surface by scanning tunneling microscopy (STM) at the solid-liquid interface. The activity of NiAu/Au (core/shell) nanoparticle catalyst for hydrogen evolution is investigated by Lv et al. [66] and the results show that low coordinated Au sites in NiAu/Au facilitates H_2 formation in acidic media.

Investigation of the interactions between Pyr and Au(111) surface is also important in terms of revealing the potential of a new photo-catalyst. However, it is not straightforward since the (111) surface of gold is known to undergo a complex reconstruction under UHV conditions [67]. Therefore, clarifying the interactions between Pyr and reconstructed Au(111) surface is important not only because of developing new H_2 production systems, but also filling a fundamental gap in the literature by investigating interactions of large macrocyclic molecules with a complex metal surface structure.

As this literature review suggests the increasing number of promising studies leads to build photocatalytically efficient and robust several catalysts, however it is practically impossible to test the photo-catalytic activity of all possible catalysts using only experimental techniques. Instead, theoretical simulations can help screening materials, clarifying interactions at molecule/substrate and molecule/solvent interface, and providing insights into photo-activity prior to extensive experimental efforts. In this regard, this thesis is organized in seven chapters and focuses on investigating photocatalytic H_2 production systems from homogeneous to heterogeneous environments using Density Functional Theory based simulations. After this introduction, chapter

2 reports on some experimental results on model systems for H_2 production addressed in this thesis, i.e, Co-based polpyridine catalysts in solution, Pyr and CoPyr adsorbed on TiO_2 surface, and monolayer of Pyr on Au(111). Chapter 3 is dedicated to the description and limitations of theoretical models employed for the investigation of these systems. Chapters 4, 5, and 6 discuss the results on the Co-based catalyst in water environment, adsorption of Pyr on TiO_2, and adsorption, self assembly formation and metalation of Pyr on Au(111) surface, respectively. The final chapter gives conclusions and outlook.

2 Brief Account: Experimental Studies on the Catalytic Systems Addressed in This Work

The activity of Co-based polypyridyl complexes as WRC towards H_2 production in both aqueous and heterogeneous environments have been widely investigated. In homogeneous phase, the catalyst is solvated together with some photosensitizer and sacrificial electron donors to investigate the catalytic performance of the whole system. The heterogeneous systems are constituted by semiconductor or metallic solid supports where the WRC can be adsorbed. The whole system is merged in a aqueous solution or electrolyte. In this chapter, we will first briefly summarize the experimental results obtained for Co-based poly-pyridyl catalysts in both homogeneous and heterogeneous environments. Afterwards, we will discuss some open questions that we are able to address by complementing the experimental research by proper theoretical modeling.

Co-based Water Reduction Catalysts Solvated in Water

Among the Co-based complexes suggested so far that are active in homogeneous environment we will particularly focus on the ligand environment containing pentapyridyl and tetrapyridyl units. In Chemistry Department of UZH the researchers under the supervision of Prof. Roger Alberto successfully synthesized the Co-deposited penta-pyridyl ligand, CoPPy, comprising five individual pyridines and two hydroxy functions in the backbone [24]. This ligand structure offers a coordinating pocket with an almost perfect octahedral arrangement. By differential pulse polarogram a reduction potential of $Co^{II/I}$ at -1.3 V (vs Ag/AgCl) has been measured. For testing the photocatalytic activity of the CoPPy, several tests have been carried out together with ascorbic acid/sodium ascorbate buffer and $[Re(py)(bpy)(CO)_3]^+$ as a photosen-

sitizer in aqueous solution under 385 nm LED source. The achieved turnover numbers (TONS) are up to 1180 H_2/Co in 45 h.

To enhance the catalytic activity, an alternative catalyst with the same denticity as CoPPy but less symmetric ligand consisting of two 2,2'bipyridine units and one single pyridyl donor, CoaPPy, has been synthesized [24]. While four pyridine units occupy the equatorial positions, the fifth one is placed in the axial position. Compared to the CoPPy, the ligand environment in CoaPPy does not offer a regular coordination pocket, thus leading to a non-ideal pentadentate coordination. This coordination is described as distorted trigonal prismatic geometry, which results in sterical constraints and strongly distorted octahedral structure. The difference in coordination environment around Co is supposed to yield different activity results. Indeed, the reduction potential $Co^{II/I}$ for CoaPPy is -0.87 eV, hence lower than the one for CoPPy and also the TONS of 1380 H_2/Co in 10 h is enhanced. Though expected, the mechanistic details on how the distorted structure affects the reactivity have not been fully explained yet.

Apart from the distortions in structural geometry, the number of pyridyl units coordinating Co center can also be a factor influencing the activity of the catalysts. In this regard, a complex with a tetra-pyridyl ligand that also displays significant distortions from an octahedral geometry has been proposed by the same research group [26]. They synthesized the hydroxy derivative of a tetra-pyridyl type ligand based (TPY-OH = 2-bis(2-pyridyl)(hydroxy)methyl-6-pyridylpyridine) Co catalyst, CoaTPy, and investigated its water reducing activity under photo-catalytic conditions in an aqueous solution [26]. The reduction potential of $Co^{II/I}$ measured using a cyclic voltammogram tuns out to be -1.11 eV (vs Ag/AgCl). The excitation of the PS under 385 nm LED leads to the reductive quenching by ascorbate, which is followed by an electron transfer from PS^- to WRC. The rate profile of the CoaTPy catalyst shows that the promising TONS as high as 9000 can be achieved in 20 h [26].

More mechanistic studies on the same catalyst and PS together with TEOA as sacrificial electron donor in aqueous solution have been carried out by joint experimental and theoretical work of Rodenberg, Alberto, Hamm, and Baldridge et al. [21]. In particular, modeling the catalyst by static calculations in water environment reveals a distorted square-pyramidal coordination geometry. The UV spectra shows two intense bands at 250 nm and 305 nm which are attributed to the π–π^* transitions. The laser flash photolysis experiment shows a peak at 620 nm which is related to the generation of Co^I-WRC specie upon electron injection from the PS^- to the catalyst.

The electronic structure calculations predict two allowed spin states for Co^{I}-WRC which are singlet and slightly more stable triplet spin states. Further calculations on visible spectrum reveal a moderate signal at 763 nm and strong bands at 404 and 270 nm for singlet spin state of Co^{I}-WRC. On the other hand, much weaker signals are obtained at the range between 643–371 nm for the triplet spin state. Furthermore, protonated specie, $Co^{III}H$, shows strong bands at 288 and 235 nm. Mechanistic findings suggest that after first reduction and protonation of the catalyst, an intermediate reduction of $Co^{III}H$ to $Co^{II}H$ occurs. The overall mechanism towards H_2 production is, therefore, supposed to take place with two separate protonation steps and transient accumulation of a cobalt hydride as an intermediate [21].

Taking all the mentioned results into consideration, the three Co-based polypyridyl CoPPy, CoaPPy, and CoaTPy, turn out to be promising active and stable water reducing catalysts under acidic conditions. By tuning the ligand framework, distorting the perfect octahedral geometry, less negative reduction potentials of $Co^{II/I}$ are observed together with higher TONS. Additionally, decreasing the number of pyridyl subunits, from five to four, somehow leads to significantly higher performance towards H_2 production. Theoretical investigations of the effects of number of pyridyl units and coordination pocket around Co center on H_2 production mechanism and rate limiting steps will improve our understanding of the water reduction systems and facilitate the design of more efficient homogeneous catalysts. Our theoretical studies on the CoaPPy and CoaTPy catalysts in water environment are discussed in Chapter 4.

Water Reduction Catalysts Adsorbed on TiO_2 Surface

Regarding the investigation of the WRC immobilized on semiconductor surfaces, we refer to the work done in the group of Prof. Jürg Osterwalder in Physics Institute of UZH, the bonding geometry and the electronic structure of the CoPyr adsorbed on a rutile $TiO_2(110)$ surface have been studied by means of STM, photoelectron spectroscopy (XPS/UPS), and low-energy electron diffraction (LEED). In order to elucidate the role of the Co^{2+} center on the molecular levels and their alignment with the substrate, they also performed a comparative study of the unmetalated Pyr on the same substrate. [68].

The LEED data indicate that the deposition of 0.1 monolayer (1 ML $\approx$ 1 Pyr molecule per 8 TiO_2 surface unit cells) of Pyr on $TiO_2(110)$ yields randomly distributed adsorbates, without apparent preferential sites or clustering. This is con-

firmed by room-temperature STM images, shown in Figure 2.1, where individual Pyr molecules appear blurred in the form of two lobes on the TiO_2(110) surface. These lobes are aligned along two directions, labeled as A (green) and B (blue) in Figure 2.1(c) which are tilted by -18 and -20 degrees with respect to the (001) axis, respectively. The bridging-oxygen rows (white lines in the figure), also observed by Diebold et al. [69], intersect the molecules between the two lobes. The resolution of the STM does not provide more detailed information on the internal molecular structure and binding mode.

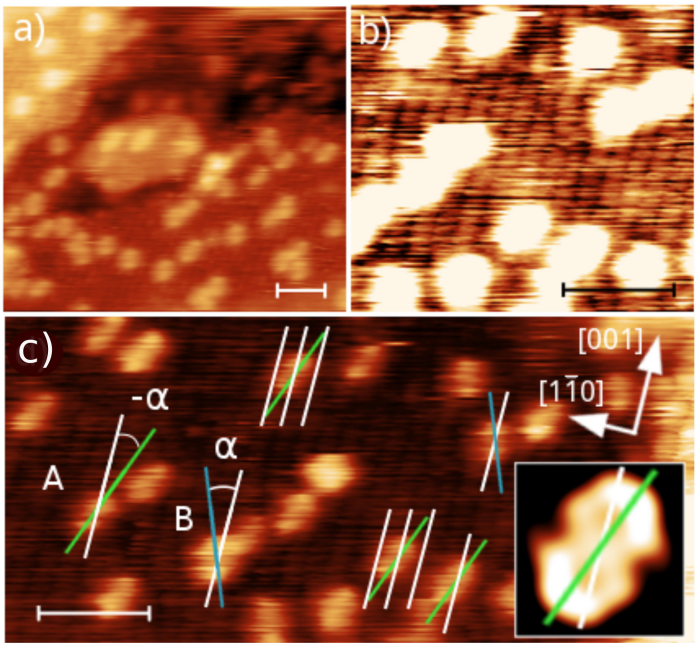

Figure 2.1: Empty state STM images of 0.1 ML Pyr on TiO_2(110). (a) Adsorbed Pyr molecules appear as bright elliptical configurations. (b) Region of (c) with optimized contrast for the dark lines representing the bridging-oxygen rows of the substrate. (c) Submolecular resolution exhibits two lobes per molecule which allow to identify the molecular orientation with respect to the bridging-oxygen rows (highlighted by white lines). Two molecular orientations A and B indicated with green and blue lines, respectively, are observed with the molecular axis rotated by $\alpha \approx \pm 19°$ with respect to (001). (Tunneling conditions: U_s =2.4 V, I_t=151 pA, scale bar≈3 nm.) For more details, see Ref. [68].

Concerning the metalation of the adsorbed Pyr molecules XPS measurements show that Pyr/TiO2 is readily metalated at room temperature. The underlying reason for this spontaneous metalation could not be addressed experimentally. It is known that the kinetics of the metalation reaction could be influenced by the diffusivity of Co on the substrate or a different propensity for Co cluster formation [70]. However,

concerning the obtained STM images it is supposed that the adsorption geometry of the Pyr molecules prior to the metalation most likely plays a role in enhancing the metalation process.

UPS measurements indicate that Co incorporation does not induce a drastic variation of the electronic structure of the adsorbate/substrate system. On the other hand, it has been observed that the presence of Co significantly enhances the structural stability against continuous UV-irradiation. While the photo-induced decomposition of the Pyr molecules is revealed from the evolution of the photoemission spectra, as shown in Figure 2.2, the CoPyr signal remains stable, suggesting the stabilizing effect of metalation, which makes it resilient against UV-induced degradation. The reasons of the increased structural stability followed after Co deposition should be clarified with the support of the theoretical simulations.

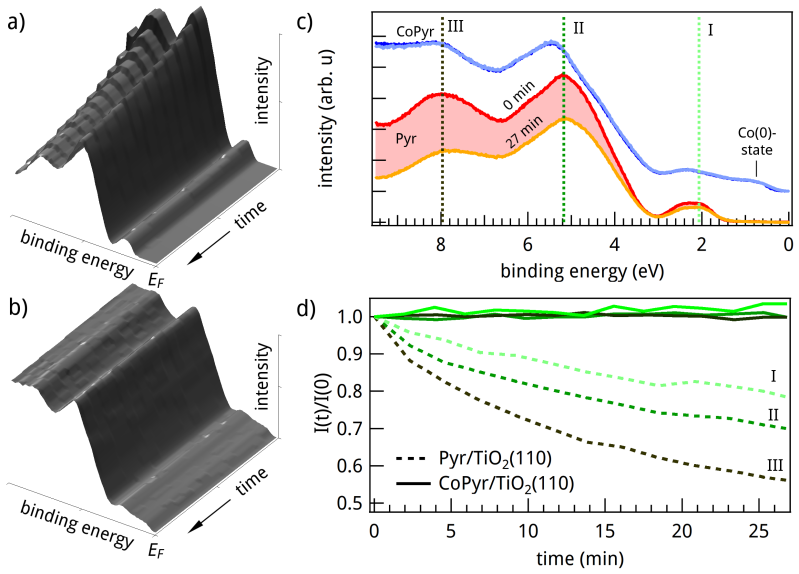

Figure 2.2: Stability of (a) Pyr/TiO_2(110) and (b) CoPyr/TiO_2(110) under exposure to He Iα radiation (21.2 eV), measured by continuously recording UP-spectra during 27 min. (c) Measured valence band spectra for Pyr and the CoPyr with an arbitrary offset added to the latter. (d) Photoelectron yield as function of time at fixed binding energies I, II and III as marked in (c). Pyr (dashed lines) shows almost exponentially decaying states, whereas CoPyr (solid lines) appears to be stable over this time period. For more details, see Ref. [68]

The theoretical approach can provide the most probable adsorption geometries of the Pyr and CoPyr monomers, and of the monolayers. These simulations can shed light on the spontaneous metalation of the Pyr molecules. Electronic level alignment

calculated for the monolayer structures with respect to the $TiO_2(110)$ can be compared with the UPS results. Charge transfer analysis and comparison of neutral and charged species can provide insights on the increased photo-stability of the CoPyr species with respect to Pyr. All these calculations are discussed in Chapter 5.

Co-based Water Reduction Catalysts Immobilized on Au(111) Surface

The same research group in Physics Institute of UZH also studied the adsorption of Pyr on a single crystalline Au(111) surface in ultrahigh vacuum (UHV). They obtained Pyr coverages up to one monolayer by sublimation of the molecules on a Au(111) surface at room temperature. Upon deposition of Co metal followed by subsequent annealing, up to 523 K, 90% of the adsorbed molecules is transformed into CoPyr. Also in this case the adsorbate/metal systems are then characterized by means of LEED, STM, and XPS [71].

The LEED patterns obtained before and after metalation reveal a transformation of the monolayer superstructure. While every Pyr molecule covers an area associated with 17.5 Au atoms, after metalation process the area per each CoPyr molecule corresponds to 18.7 Au atoms, i.e., slightly larger than for the starting Pyr superstructure. A sequence of STM images recorded after Co evaporation on a monolayer Pyr/Au(111) surface is shown in Figure 2.3. A hexagonally-ordered molecular layer is observed on top of the preserved herringbone reconstruction of the Au(111) surface. The majority of the molecules are imaged as spots of relatively uniform and intermediate brightness (labeled as B) representing $\approx 90\%$ of the molecular lattice, are determined as CoPyr complexes, with Co atoms occupying the central, four-fold nitrogen-coordinated site. Dark spots (C) mark point defects within the molecular lattice. Very bright spots (D) and (E) appear to be small remnant Co clusters resulting from the metal deposition and they disappear as annealing proceeds. The darker gray donut shaped spots (A) which show a slight depression in their center are identified as non-metalated Pyr molecules. At intermediate stages, some molecules appear brighter than the most common Pyr image (A), still exhibiting a two lobes structure. These have been labeled with F. Successive annealing steps to 373 K and to 423 K increase the number of brighter molecules, the two lobes features change to a single central protrusion (B). The presence of the F features suggests the existence of intermediate metalated states formed before the annealing. However, the structures of these intermediate states could not be identified by the experiments.

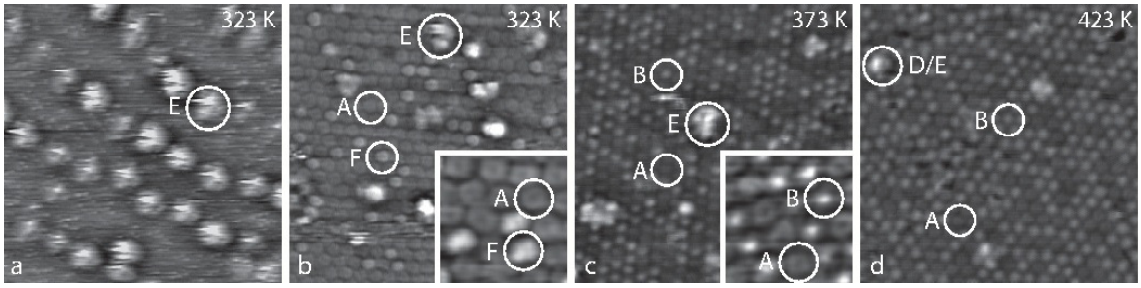

Figure 2.3: STM images covering (a) 50×50 nm^2, (b)-(d) 25×25 nm^2 and (insets) 4×4 nm^2, recorded after Co evaporation on a monolayer Pyr/Au(111) surface at a sample temperature of 323 K (a,b), and after successive annealing steps to 373 K for 1 hour (c), and to 423 K for 14 hours (d). Tunneling parameters: (a) -1.0 V, 1.0 nA; (b) +0.8 V, 0.5 nA; inset -1.0 V, 0.5 nA; (c) -0.8 V, 0.5 nA; inset -0.8 V, 0.5 nA; (d) -0.8 V, 1.0 nA. For more details, see Ref. [71].

To shed more light on the metalation process, XPS measurements have been carried out to characterize the Co oxidation state and the N species involved. Figure 2.4(a) shows the Co $2p_{3/2}$ spectrum of the metalated Pyr monolayer while the evolution of the Co $2p_{3/2}$ spectrum as a function of the annealing temperature is depicted in Figure 2.4(b). In the latter, the peak at binding energy of 777.7 eV is attributed to the metallic Co and it decreases in intensity with the annealing, whereas the peak with higher binding energy, 780.3 eV, is related to the Co atoms ligated to the cores of Pyr molecules. One possible interpretation for this metallic-like component in the Co $2p_{3/2}$ spectrum is in terms of the interaction of the molecular Co center with the substrate. Indeed, a modulation of the binding energy between the molecule and the Au(111) surface could explain the shift in the photoelectron energy. However, which is the origin of such modulation has not been fully understood yet. One hypothesis is that this is related to the different regions characterizing the Au(111) reconstructed surface or due to different possible adsorption geometries. Therefore, the effects of different surface domains on binding strength and shifting in XP spectra are the open questions that should be clarified by theoretical studies.

The N 1s spectra as metalation proceeds are reported in Figure 2.4(c). The spectrum of Pyr/Au(111) (top curve) shows two bands, compassing photoelectrons from three different chemical environments: pyridinic (-NH-) with binding energy of 400.1 eV, iminic (-C=N-) at 398.5 eV and cyano (-C≡N) at 397.9 eV. After Co evaporation and subsequent annealing (bottom curve), the spectrum collapses into a single band. These data also confirm metalation of 90% of the Pyr molecules as deduced

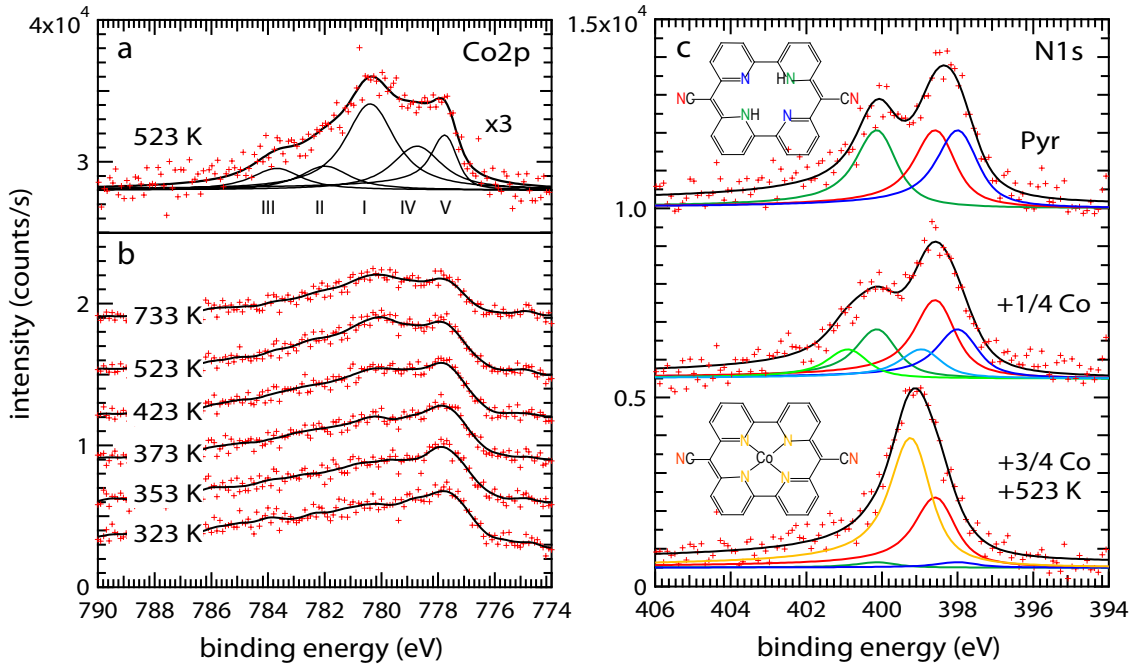

Figure 2.4: XPS data and corresponding fits of Co $2p_{3/2}$ and N 1s spectra before and after Co evaporation on a monolayer Pyr/Au(111) surface and after subsequent annealing. (a) Co $2p_{3/2}$ spectrum measured after a 12 hour annealing at 523 K fitted with three main components at binding energies of E_B = 780.3 eV (I), 778.9 eV (IV) and 777.7 eV (V) and two additional satellites at 781.9 eV (II) and 783.7 eV (III). (b) Evolution of the Co $2p_{3/2}$ spectra as a function of the annealing temperature fitted with the same five components. (c) N 1s spectra before the Co evaporation (top), after partial Co evaporation (a quarter of the total deposition) without annealing (middle) and after the complemented Co evaporation (resulting in a total coverage of 0.043 ML) with subsequent annealing to 523 K (bottom). The top spectrum has been fitted with three peaks representing the three different species of nitrogen atoms in the pyrphyrin molecule: the cyano-N (398.5 eV, red), the pyridinic-N (400.1 eV, green) and the iminic-N (397.9 eV, blue). After Co metalation in the bottom spectrum, the pyridinic-N and iminic-N peaks are both greatly reduced and replaced by a new Co-N peak (399.2 eV, orange). Co evaporation without annealing produces a distinct shift of the middle spectrum to higher binding energies that can be accounted for by adding two additional components at 400.8 eV (light-green) and 398.9 eV (light-blue). See Ref. [71] for more details.

from the STM. On the other hand, already soon after the Co deposition before annealing a distinct shift of the N 1s spectra to higher binding energies (middle spectrum) is observed indicating existence of some intermediate states.

It is remarkable that, although in many related porphyrin monolayer systems the metalation reaction occurs rapidly and spontaneously upon metal deposition at 300 K, [72] the metalation of Pyr on Au(111) needs to be activated. The probable reasons, though not yet assessed by the experimental evidence, are the structural differences of Pyr cores with respect to the porphyrins and/or the presence of some intermediate steps acting as bottleneck during the metalation process.

In summary, the optimized geometry of the Pyr and CoPyr monomers, the formation of Pyr monolayer, and the metalation dynamics of Pyr assembly on Au(111) surface are the open questions raised by the experimentalists that we are going to address by the computational modeling approach. In particular, the effects of the herringbone reconstruction, possible intermediate metalated states are discussed in Chapter 6.

3 Theoretical Approaches

In this chapter, the main underlying principles of Density Functional Theory and Ab-initio Molecular Dynamics simulations that are used throughout this thesis are briefly introduced. In particular, the standard and hybrid DFT formalisms, the augmentation of DFT by adequate corrections for the van der Waals interactions, the theoretical framework of AIMD, the simulation of spectroscopic properties, and several methods for analyzing the calculated electronic structure are introduced and correlated by examples. As a final remark challenges and limitations of DFT-based simulations are discussed.

3.1 Density Functional Theory and Ab Initio Molecular Dynamics

DFT is developed by Hohenberg, Kohn, and Sham [73,74] in 1964 as a minimization problem of ground-state energy as a function of electron density. The approach is to solve any fully interacting problem by mapping it to a non-interacting problem introducing exchange–correlation functionals, see Equation 3.1.

$$E = E_{\mathrm{xc}}[\rho(r)] + T_{\mathrm{s}}[\rho(r)] + J[\rho(r)] + \int v_{\mathrm{ext}}(r)\rho(r)dr \tag{3.1}$$

$E_{\mathrm{xc}}[\rho(r)]$ term is the exchange and correlational energy contribution. While electron correlation addresses how an electron interacts/sees the other electrons in an atom or molecule, the electron exchange related to the Pauli Exclusion principle describes the exchange of electrons between a fermion and a boson. $T_{\mathrm{s}}[\rho(r)]$ is the kinetic energy of the non-interacting system, $J[\rho(r)]$ is the classical Coulomb repulsion energy, and $\int v_{ext}(r)\rho(r)dr$ is the interaction of the external potential acting on the electrons. All of these terms are called functionals which depend on the electron density $\rho(r)$, i.e., the number of electrons per unit volume.

The electron density can be expressed in many ways [75], however Gaussian and plane wave formalism is shown to be significantly efficient for the description of the

orbitals [76]. A localized Gaussian basis set positioned at each atom is used to expand the Kohn-Sham orbitals and an auxiliary plane wave basis set is used to describe the electron density, thus improving the computational performance in the calculation of the Coulomb interactions. The description of the total charge density $\rho(r)$ is given in Equation 3.2.

$$\rho(r) = \sum_{n} f_{\mathrm{n}} |\psi(r)|^2 = \sum_{n} f_{\mathrm{n}} \sum_{\alpha\beta} C_{\alpha n} C_{\beta n} \varphi_{\alpha}(r) \varphi_{\beta}(r) = \sum_{\alpha\beta} P_{\alpha\beta} \varphi_{\alpha}(r) \varphi_{\beta}(r) \qquad (3.2)$$

where the $\psi(r)$ are the molecular orbitals and f_n is the occupation number of the corresponding molecular orbital. The $C_{\alpha \mathrm{n}}$ are the expansion coefficients which are the variables during wave function optimization. While the density matrix $P_{\alpha\beta}$ is determined by the $C_{\alpha n}$ terms, its size depends on the total number of basis set functions. The real space integration of the atomic orbitals, $\varphi_{\alpha}(r)$ and $\varphi_{\beta}(r)$, give the overlap matrix, i.e., $S_{\alpha\beta}$=$\langle\varphi_{\alpha}|\varphi_{\beta}\rangle$. This formalism of the electron density is shown to be a suitable choice for large scale DFT simulations [71, 77].

Although, the achievement in introducing electron density dependence of the total energy instead of the electron wave functions and providing simple, universal, and self-consistent-field description of the ground-state electronic structure, any practical usage of DFT requires an accurate description to the exchange and correlational functional, $\mathrm{E_{xc}}[\rho(\mathrm{r})]$, see Equation 3.3.

$$E_{\mathrm{xc}}[\rho(r)] = (V_{\mathrm{ee}}[\rho(r)] - J[\rho(r)]) + (T[\rho(r)] - T_{\mathrm{s}}[\rho(r)]) \qquad (3.3)$$

where $T[\rho(r)]$ is the kinetic energy of the interacting system and $V_{\mathrm{ee}}[\rho(r)]$ is the non-classical interaction between electrons. Although, the exact analytic expression of the exchange–correlation functional is not known, approximations to these terms have been demonstrated to be able capture most of the physical/chemical properties of many systems from solid state to liquid environment.

Many methods have been proposed to calculate exchange-correlation contribution to the total energy [78]. One of the most commonly used one is the Generalized Gradient Approximation (GGA), where the exchange and correlation energy depends on both electron density and its gradient [79]. This method includes semiempirical functionals which consist of one or more parameters fitted to experimentally observed quantities. Perdew-Burke-Ernzerhof (PBE) [80] and Becke exchange/Lee-Yang-Parr correlation (BLYP) [81] are the most popular semiempirical functionals.

These functionals are successfully applied to many systems, i.e., metals and 2D self-assemblies [82]. However, it is shown that they fail to accurately reproduce some experimentally observed properties of some particular systems, such as oxides, transition metal deposited macrocyclic molecules and aqueous environments. Often the inaccuracies are related to the incorrect description of electronic localization by standard DFT [83]. The reason is attributed to the incomplete cancellation of the Coulomb self interaction in GGA functionals, which leads to the stabilization of electrons' delocalization [84]. For instance, the PBE density functional captures structural properties of both bulk phase and surface of TiO_2, however the band gap of bulk TiO_2 is predicted as 1.74 eV [85], which significantly underestimates the experimental band gap of 3.2 eV [86]. Therefore, for electronic structure analysis and band alignment of oxides one should go beyond GGA [87].

One of the commonly applied method to overcome the failure of GGA is to use hybrid density functionals, which mix the exact Hartree-Fock exchange from [88] and GGA. Applying hybrid functionals removes some of the self–interaction error and favors localized electronic states by reducing the barrier to the localization. [89] Including orbital analogue of exchange formalism in hybrid functionals often improves the accuracy of the simulations, however the computational cost significantly increases by an order of magnitude with respect to the pure GGA formalism. The most popular hybrid functionals are, e.g., HSE06 [90,91] and PBE0 [92]. The band gap of bulk TiO_2 results to be 4.21 eV [93] and 3.35 eV [87] by PBE0 and HSE06, respectively. Since also the hybrid functional formalism introduces some empiricism in the combination of the schemes, it is always recommendable to perform the pre-tuning of the computational settings on some known property. In the specific case, the HSE06 is to be preferred to the PBE0 description. For more details on the effects of employed density functionals on the properties of TiO_2 bulk and slab, see Chapter 5.

In addition to the difference in calculated band gaps, the fingerprints of the selected formalism appear also by comparing the total or projected density of states, TDOS or PDOS, of the system under consideration. The inspection of the density of states provides further information on the redistribution of the molecular orbitals upon adsorption and on the nature of the interactions. Figure 3.1 shows the comparison between the PDOS computed for CoPyr in the gas phase using HSE06 or PBE. The localization of the electronic states introduced using HSE06 has a clear effect on the energy distribution of the orbitals with 2p-N_{CN} and 3d-Co(II) character. In particular, the highest occupied states at the Co(II) metallic center are stabilized by

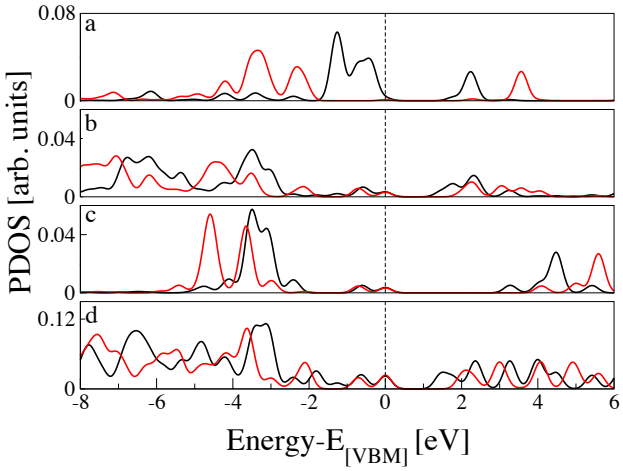

Figure 3.1: PDOS on different species of CoPyr calculated using HSE06 (red solid line) and PBE in the gas phase (black solid line). a) PDOS on Co, 3*d* states. b) PDOS on the central N atoms binding to the pyridine rings (N_p), 2*p* states. c) PDOS on the external N atoms belonging to the cyano groups (N_{CN}), 2*p* states. d) PDOS on all carbon atoms, 2*p* states. Energy states of CoPyr are aligned with respect to its valence band maxium (VBM). For the schematic representation of CoPyr, see Figure 5.5 in Chapter 5.

about 2 eV, while the lowest unoccupied states are pushed to higher energies by more than 1 eV. This corresponds to the decoupling of these states from the states on N_p and C, in particular for what concerns the unoccupied orbitals. With PBE, instead, the unoccupied states projected on C and N_p are hybridized with the delocalized 3d states of Co at about 2.5 eV. This has a pinning effect that most probably prevents the further relaxation of the energy gap, see also Figure 3.2 and Table 3.1.

The PDOS on the different atomic species in CoPyr and Pyr are compared in Figure 3.2. The corresponding energy gaps obtained with both the PBE and the HSE06 density functional are reported in Table 3.1. The band gap correction achieved using HSE06 with respect to PBE is around 0.57 eV for CoPyr and it is roughly 0.71 eV for Pyr. The PDOS analysis suggests that the significant difference in the distribution of energy states calculated using PBE and HSE06 is mainly due to the cyano nitrogens. These results confirm that HSE06 corrects the ground state electron distribution not only for transition metal deposited macrocyclic molecules but also for the metal-free ones.

Also in the description of the electronic structure of liquid water, PBE underestimates band gap by more than 4 eV [94]. The difference becomes less pronounced in

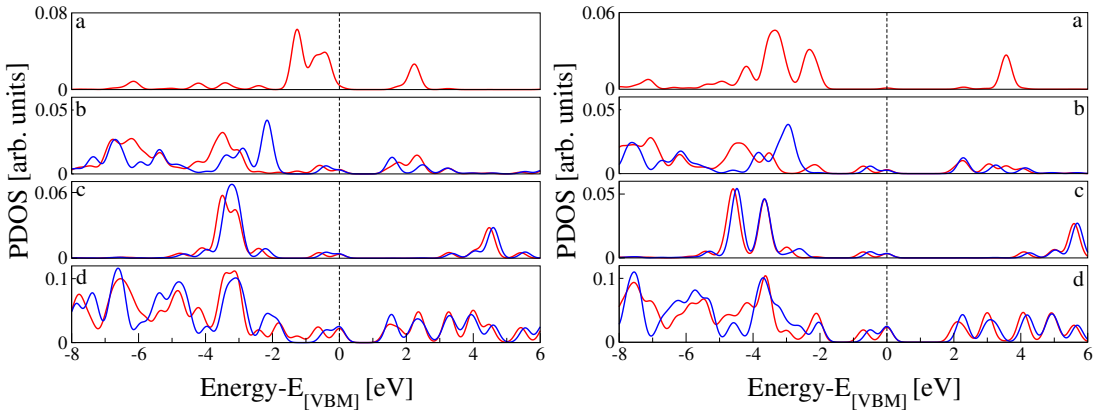

Figure 3.2: PDOS on different species of CoPyr (red solid line) and Pyr (blue solid line) calculated using PBE (left) and HSE06 (right) in the gas phase. a) PDOS on Co, 3*d* states. b) PDOS on the central N atoms binding to the pyridine rings (N_p), 2*p* states. c) PDOS on the external N atoms belonging to the cyano groups (N_{CN}), 2*p* states. d) PDOS on all carbon atoms, 2*p* states. For the schematic representations of CoPyr and Pyr, see Figure 5.5 in Chapter 5.

Table 3.1: Homo-lumo gap (E_{gap}) of Pyr and CoPyr calculated with different density functionals.

Molecule	Functional	E_{gap} [eV]
Pyr	PBE	1.52
Pyr	HSE06	2.23
CoPyr	PBE	1.46
CoPyr	HSE06	2.03

the case of solvated WRC. Indeed, the experimental energy gap of CoaTPy, in aqueous solution has been measured to be 3.87 eV and the one obtained for one CoaTpy molecule solvated in 215 water molecules gives 1.68 eV and 3.75 eV using PBE and PBE0, respectively. Figure 3.3 shows the calculated homo and lumo orbitals of CoaTPy/water system using PBE and PBE0. Although, PBE underestimates the gap by 2.07 eV with respect to PBE0, the localizations are very similar for the two density functionals. While the homo is distributed over the Co(II) center and the pyridine nitrogens, the lumo is mainly located on the bipyridine ring.

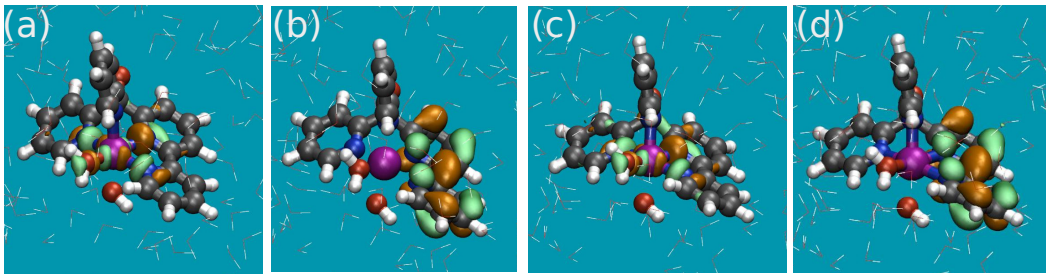

Figure 3.3: Frontier molecular orbitals of CoaTPy/water system using different exchange-correlation density functionals. a) Homo and b) lumo calculated by PBE, c)Homo and d)lumo calculated by PBE0. Color code: gray: C, white: H, red: O, blue: N, and purple: Co. While CoaTPy is depicted as ball and stick representation, water solvent is shown by sticks. Isosurface (green for positive and orange for negative) is set to 0.04 e/Å^3.

The proposed density functionals are also unable to accurately describe the dispersion interactions among non bonded subsystems at an intermediate distance. This is mainly due to deficiencies in the description of the correlation interaction and to a not correct fast decay of the electron density away from the atomic centers. This flaw of DFT might have important consequences in the description of the geometries of systems where these type of interactions play an important role. This is the case, for instance, of molecule/substrate systems. However, effects are also to be noticed in the dynamics of soft condensed matter systems, like water. One example is cis/trans coordination of the ligand with respect to the anchoring group adsorbed on the anatase TiO_2 (110) surface that affects the binding mode of the molecule. [95]. One common approach is to add an empirical dispersion energy correction term, as for example suggested by Grimme et al. [96], on top of the total energy obtained by DFT. The simplest for of this type of correction is a pairwise interaction parametrized for each specific atomic species and defined as;

$$E_{\text{disp}} = -\frac{1}{2}\sum_{A,B} f_{damp}(r_{AB}, r_A^{vdW}, r_B^{vdW}) C_{6,AB} r_{AB}^{-6} \tag{3.4}$$

Here r_{AB} is the distance between particles A and B, and f_{damp} is a factor introduced to prevent divergence in calculated E_{disp} for small r_{AB}. The dispersion coefficients $C_{6,AB}$ are fitted to some reference data sets and might also depend on the coordination numbers of each atom. When depending on the number of neighbors, the appropriate coefficient is assigned to each specific pair AB and is updated at each simulation step.

Overall, such a correction type reproduces the expected $1/r_{AB}^6$ asymptotic behavior and it is the most widely employed formalism that corrects the dispersion interactions.

An alternative method introduces non-local van der Waals (vdW) density functionals, which directly depend on the electronic density and have to be calculated within the self consistent cycle. Within this approach, the correlation term is partitioned into local and non-local contributions. These are treated by means of different functional forms. The general expression for the non-local correlation energy E_c^{nl} is given as [97];

$$E_{\mathrm{c}}^{nl} = \frac{1}{2} \int \int \rho(r_1)\phi(r_1, r_2)\rho(r_2) d^3r_1 d^3r_2 \tag{3.5}$$

where $\phi(r_1,r_2)$ is the integration kernel showing $1/r_{12}^6$ asymptotic behavior. The non locality comes from the two center form of the kernel,

$$\phi(r_1, r_2) = \phi(\rho(r_1), \rho(r_2), |\nabla\rho(r_1)|, |\nabla\rho(r_2)|, |r_1 - r_2|) \tag{3.6}$$

The most popular non-local vdW density functionals are, e.g., Vydrov–Voorhis (rVV10) [98, 99] in revised form and Dion–Rydberg–Schroder–Langreth–Lundqvist (DRSLL) [100]. It has been demonstrated that the short range regime of the vdW interactions are in most of the cases accurately captured by rVV10 [101]. Although, the performance of DRSLL is quite good for gas-phase dimers and solids, the calculated dispersion energy terms are generally larger than the ones obtained by rVV10 [97]. The dispersion corrections are always taken into account for the simulations reported in this thesis. The rVV10 vdW formalism combined with the PBE exchange-correlation functional is used for modeling Co-based catalysts in aqueous environment, placed in Chapter 4, the Grimme-D3 scheme is employed for the CoPyr adsorption on TiO_2 surface, see Chapter 5. The effects of Grimme-D3, rVV10, and DRSLL vdW schemes on Au(111) surface structure are detaily discussed in Chapter 6.

By taking advantage of DFT, one can optimize structures, determine the most stable adsorption geometries, calculate corresponding adsorption and interaction energies, and extract different structural and electronic properties. Electronic structures can be analyzed by calculating PDOS, schematic representation of molecular orbitals, population analysis, charge distribution maps, and charge density difference maps. All these analytical tools are heavily used in the discussion of the results reported in this thesis.

Starting from the computed electronic structure, it is a common practice to try to reproduce the outcome of experiments such as STM images, XPS/UPS spectra,

infrared spectra, etc. The direct comparison to the experimental data not only allows the assessment of the computational settings, but also rational interpretation of the experimental results. As theoretical model for the STM we employ the Tersoff and Hamann approach, proposed in 1985 [102]. The tip is considered as a locally spherical potential well and using first-order perturbation theory the tunneling current becomes proportional to;

$$I \propto \rho_b(z) e^{-2kR\sqrt{\Phi}} \tag{3.7}$$

where z is the height of the tip above the slab, ρ_b is the charge density of states within bias potential from the Fermi energy, Φ is the local work function, R is the tip curvature radius, and $k{=}\sqrt{2m_e}/\hbar$. Theoretical STM images are obtained by keeping $\rho_b(z)e^{-2kR\sqrt{\Phi}}$ term at a constant value for different positions in xy plane over the slab. The examples of the calculated STM images are depicted in Chapter 6.

The exploration of the conformational space at finite temperature is obtained by running AIMD [103] through the generation of trajectories of several picoseconds. Phase-space trajectories are generated via numerical integration of the equations of motion. Within the Born-Oppenheimer (adiabatic) Approximation [104], at each atomic configuration the electronic structure problem is solved in the ground state. This means that the dynamics of electrons is not propagated, because it is assumed that electrons instantaneously adjust to the atomic configuration. Therefore, the electrons are fully decoupled from the nuclear motion at each MD step. Nuclei is subsequently propogated according to the forces obtained from the electronic structure calculation from timestep to timestep.

Along the AIMD trajectory, energies and forces are calculated on-the-fly at each time step. For a reasonably long sampling of the phase space, this obviously requires significantly large computational resources, well beyond those needed for single point calculations or even geometry optimizations. To reduce the computational costs empirical or semi-empiricial models could be employed. However, the poor transferability of the empirical parameters limits the applicability of such models to complex systems with important evolution of the electronic structure.

Effective sampling of the phase space which might include many energetically deep, separated wells is crucial, since otherwise rare events can not be simulated within feasible computational times. Several methods have been proposed to enhance the exploration of the phase space. One of those methods is metadynamics (MTD) [105, 106], which samples the free energy surface (FES) uniformly based on a history-

dependent bias potential. The applied bias potential accelerates the exploration of the phase space thus enabling monitoring rare events. Properly selected collective variables (CVs), which are functions of the microscopic coordinates describing the most relevant structural changes are used to describe and reduce the dimension of the FES. Thanks to this scheme several rare events can be captured and FES can be constructed accurately in affordable computational times.

3.2 Challenges of Quantum Chemical Methods

In order to understand the physical properties of condensed matter and to develop efficient photocatalytically active devices, one has to use adequate theoretical methods. Although, DFT is a powerful tool to analyze and screen many systems, such as homogeneous catalysts immersed in solution, semiconductors or metal surfaces, it also brings some limitations and challenges. One important issue is the computationally feasible system size. For example, when modeling a slab, the selected number of layers included in the model might affect the resulting structural and electronic properties. When dynamics properties are considered, the spatial correlation can also become an important drawback. There are properties that are more slowly converging with the system size, as for instance the surface energy of a slab or the diffusion coefficient in a liquid. Hence, depending on the specific goal of the investigation, different types of model can result more or less appropriate. In case of the surface energy of rutile $TiO_2(110)$, it is known that it depends on both the thickness of the slab and the number of slab layers that are relaxed during the simulation [87]. While increasing number of layers from 5 to 9 reduces surface energy roughly by 0.05 J/m^2, employing relaxed four outermost layers decreases surface energy by more than 1.05 J/m^2 with respect to the fully rigid slab model, see Chapter 5 for details. In this regard, Harris and Quong [107] proposed a method called "25% rule" to determine the adequate slab thickness that should be used in the simulations. The requirement is also similar for liquids where one should use large simulation box with sufficient number of molecules to correctly reproduce the experimental observations, such as liquid density, see Chapter 4 for details. While the system size has to be large enough to increase the calculated accuracy, it also increases computational effort. The reason is that the computation does not scale linearly with the system size, and the exact scaling depends on the specific algorithms employed for the optimization of the self-consistent-field problem. In case of AIMD runs required computational source

becomes even more expensive than DFT calculations. Therefore, one needs to find a compromise between accuracy and the computational cost.

As already stated, the other issue is the uncertain forms of exchange–correlation functionals. An appropriate, carefully chosen exchange-correlational formalism has to be applied for each system under consideration. For instance, BLYP density functional is considered to be a good choice for systems with transition metals, however for organic compounds, instead, B3LYP is preferred. Although, the selected exchange–correlation scheme might limit the accuracy and cause a dilemma in trusting obtained results there are several methods beyond DFT are developed and successfully used to increase the accuracy of the calculations [108, 109].

In spite of several limitations, in both the accuracy of the DFT description and size of the feasible models, this approach seems to be the most appropriate one to study the systems of interest in this work. Today DFT is an important tool to obtain optimized geometries of the complexes, analyze electronic structures, model many spectroscopic techniques, determine intermediate states of the reactions, and so on. Constant improvement in computational algorithms together with rapidly increasing computer power enable us to find for each research problem an approach with optimal balance between computational cost and accuracy. DFT and AIMD are the robust methods used to supervise experimentalists to build promising materials towards photo-catalytic applications.

4 Poly-pyridyl Cobalt-based Catalysts in Water: The Effects of Ligand Type and Coordination Pocket on H_2 Production Mechanism [110]

In this chapter, H_2 production reaction via Co-based poly-pyridyl homogeneous catalysts, CoaPPy and CoaTPy, immersed in water environment is discussed. We investigate the number of pyridyl subunits, the poly-pyridyl and bipyridyl ligand structures, the distortion of the ligands, and also the coordination sphere around the Co center and how these features affect the water reduction mechanism. In order to verify the relative stability of the intermediate states and the role of the solvent, we investigate the different oxidation states, Co^{II}, Co^{I}, Co^{III-H} , and Co^{II-H}. While each reaction step is sampled using AIMD at the GGA level of theory, more detailed electronic structure analysis of selected AIMD snapshots is performed at the PBE0 level of theory.

Following a brief introduction on the proposed catalytic cycle for the H_2 production, we describe the applied methodology and the used models for describing the solution of the catalysts in water. Next, we monitor solvent response and structural changes occurring in the catalysts at each intermediate step of the water reduction cycle. We analyze in detail the electronic structure of the complexes before and after the reduction reaction. Reduction free energies are then calculated assuming a liner solvent response and a connection between the ligand type and H_2 production performance is established. We expect that this study will clarify how the ligand type and the coordination sphere around the metal center influence the mechanism, thus identifying the structural and electronic aspects that must be tuned to optimize the process.

Catalytic Cycle for H_2 Production

Figure 4.1(a) shows possible catalytic steps towards H_2 production as well as corresponding oxidation states of the Co center. Taking experimental evidences into account, in this work we focus on the heterolytic reaction pathway shown by black solid lines and Co oxidation states depicted by red circles. This pathway requires subsequent electron and proton transfer to the Co center, hence the reaction is described as 2-electron and 2-proton transfer reaction. In accordance with the proposed reaction mechanism, we intend to simulate the equilibrium at each oxidation state, add charges and protons to change the oxidation state, monitor structural and electronic properties, compare different spin states, and compute the reduction potential, which will help us understanding the probable reasons of different catalytic performance observed for two catalysts.

Figure 4.1(b) illustrates all intermediate steps under consideration with $^{m}(\text{Catalyst})^{+q}$ formalism where $+q$ refers to the total system charge and m is the multiplicity. The initial catalytic state is $^{4}(\text{Catalyst})^{+2}$ and the first electron injection might result in one among two possible states with different multiplicity, $^{3}(\text{Catalyst})^{+1}$ and $^{1}(\text{Catalyst})^{+1}$. We consider both spin states in our simulations. Followed by a protonation reaction $^{1}(\text{Catalyst-H})^{+2}$ is obtained and second electron injection yields $^{2}(\text{Catalyst-H})^{+1}$. The reaction cycle is completed with second protonation yielding $^{4}(\text{Catalyst-H})^{+2}$-$H_2$ and after this step H_2 release from the catalytic center should be observed. As the same vein as CoaTPy, we consider all these intermediate steps also for CoaPPy in our simulations.

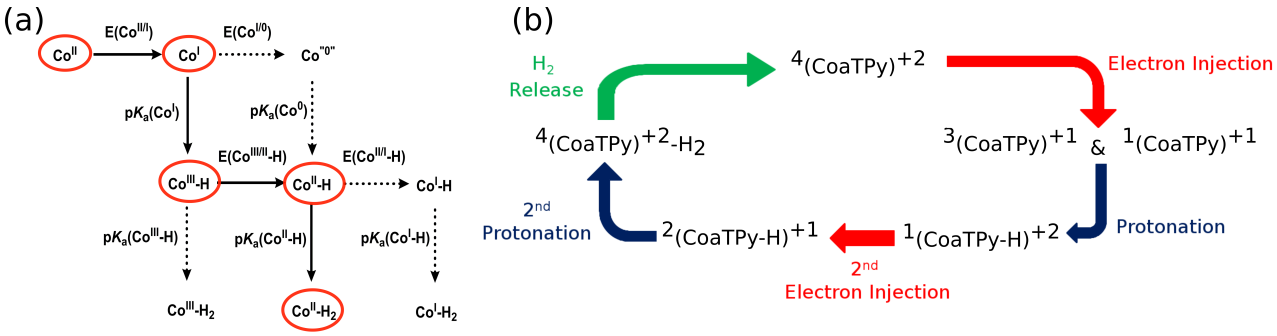

Figure 4.1: (a) Simplified scheme of the relevant reduction and protonation steps for H_2 formation on cobalt poly-pyridine catalysts. We focus on the reaction pathway shown by black solid lines and corresponding Co oxidation states depicted by red circles. (b) All intermediate steps under consideration are shown with $^{m}(\text{Catalyst})^{+q}$ formalism where $+q$ depicts total system charge and m shows multiplicity.

4.1 Computational Methodology

The electronic structure calculations are performed at the Kohn-Sham DFT level, employing the Gaussian and plane wave (GPW) formalism as implemented in the CP2K/QUICKSTEP package [111]. Valence electrons are treated explicitly, while norm-conserving Goedecker–Teter–Hutter (GTH) pseudo potentials [112] are used to describe the interactions between the valence electrons and the atomic cores. The valence shells contain 17, 6, 4, 1, and 5 electrons for Co, O, C, H, and N, respectively. Double-zeta valence plus polarization (DZVP) basis sets, optimized on molecular geometries (Mol-Opt method) [113], are employed for all atomic kinds. A cutoff of 400 Ry is used for the auxiliary plane wave basis set. Periodic boundary conditions and spin polarizations are always applied.

AIMD simulations are carried out for two Co-pyridyl complexes, CoaTPy and CoaPPy, within a fully explicit solvent environment in a cubic box. This approach allows for the hybridization of the localized electronic states of the redox active solutes with the extended band states of the solvent. The systems are equilibrated and their volumes are determined by first running 20 ps of AIMD in the NPT ensemble. AIMD/NPT runs result in a cubic box of 19.1 $Å^3$ for both systems containing 215 water molecules. Then, keeping the volume constant at its equilibrium value, the solvated catalysts are further equilibrated within the NVT ensemble for 10-15 ps. A time step of 0.5 fs is used and temperature is kept constant at around 300 K using the CSVR thermostat [114] with a time constant of 100 fs. The equilibration is followed by the production run, where the solution is sampled for other 15 ps in the NVT ensemble. The charges of the systems are neutralized by a negative homogeneous background charge density, instead of using explicit counterions [115].

All geometry optimizations of the catalysts in vacuum and the AIMD runs for the catalysts/water systems are performed using the general gradient approximation (GGA) by Perdew–Burke–Enzerhof (PBE) [80]. Dispersion interactions are included via the nonlocal electron correlation scheme conceived by Vydrov and Van Voorhis, in the revised form (rVV10) proposed by Sabatini et al. [99]. In the analytic expression of the rVV10 density functional the short-range interactions are governed by the empirical parameter b, which is set to 9.3 in this work. This level of theory has been shown to be sufficiently accurate to describe the structural properties of liquid water [94]. On the other hand, it is known that PBE significantly mispredicts the energy gap and molecular energy levels alignment of water and solute [94]. Moreover, the

delocalization error introduced by the GGA functionals leads to the underestimation of the redox potentials. The misalignment of the molecular states of the solute and the band states of the solvent aggravates the error. The electronic structure calculations performed with hybrid-functionals should substantially correct for these problems. Hence, we are going to perform the analysis of molecular orbital and spin-density distribution applying the PBE0 [92] hybrid density functional together with rVV10 electron correlation. In the case of hybrid density functional, the empirical parameter b in rVV10 is set to 5.3 [116]. All hybrid functional calculations are performed with the help of the auxiliary density matrix method (ADMM) [117–119], which provides a significant speed up. Despite the speed up obtained with ADMM, hybrid functional AIMD are still computationally very demanding and do not produce important structural changes with respect to the PBE scheme. Therefore, our strategy consists in carrying out AIMD runs at the PBE-rVV10 level of theory and refine the electronic structures of a sufficiently large number of selected snapshots distributed over the generated production trajectory using PBE0-rVV10 density functional. We then compute the reduction potential, which consist in adiabatically adding an electron to the solution, using the free energy perturbation (FEP) approach. The scheme consists in the reversible addition of an electron by simply changing the number of electrons and re-optimizing the electronic state of a large number of snapshots extracted along the AIMD sampling [120].

4.2 Structure and Solvation

4.2.1 Co-based Poly-pyridyl Catalysts in Vacuum

Figure 4.2 illustrates the ball and stick sketches of CoaPPy and CoaTPy as well as CoPPy for comparison. CoPPy has pentapyridine ligand framework which provides perfectly symmetric octahedral coordination around Co center. Four pyridine nitrogens, labeled as N_{Lpy1}, N_{Lpy2}, N_{Rpy1}, and N_{Rpy2}, occupy the equatorial plane, while one pyridine nitrogen, N_{Vpy1}, is located in the axial position. Besides, CoPPy has two hydroxy functions in the backbone. Although, CoPPy and CoaPPy have the same denticity, the latter is less symmetric. CoaPPy consists of two bipyridine units, one single pyridyl donor, and one hydroxy function in the backbone. The four pyridine nitrogens at equatorial positions are not coplanar, i.e., the coordination pocket around Co is not an ideal pentadentate. CoaTPy is, instead, characterized

by a different number of pyridyl and bipyridyl subunits with respect to CoPPy and CoaPPy, and, as a consequence, a different coordination environment around the Co center. CoaTPy consists of one bipyridine unit, two pyridyl donors, and one hydroxy function in the backbone. Also in this case the coordination is not ideal pentadentate and yields a strongly distorted structure.

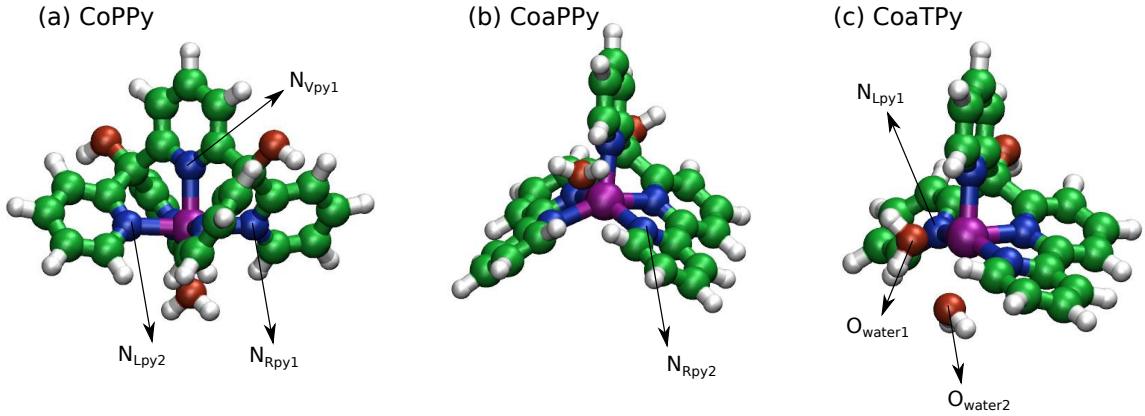

Figure 4.2: Ball and stick representations of a) CoPPy, b) CoaPPy, and c) CoaTPy. The nitrogens in differently positioned pyridyl rings are labeled as N_{Lpy1}, N_{Lpy2}, N_{Rpy1}, N_{Rpy2}, and N_{Vpy1}. The oxygen belonging to the closest water molecule to the Co center is labeled as O_{water1}, while the second closest oxygen in the solvent is displayed with O_{water2}. Color code: green: C, white: H, purple: Co, blue: N, red: O.

The most relevant structural parameters characterizing the optimized geometries of the catalysts are the distances between Co and nitrogens in different pyridyl rings and the distances between Co and oxygens of different water molecules, and are summarized in Table 4.1. The laterally located nitrogens in CoPPy are slightly more distant from the Co center than the vertically positioned nitrogen, N_{Vpy1}. On the other hand, N-Co distances are, in general, shorter in CoaPPy and CoaTPy with respect to the CoPPy. Taking all Co-N distances into consideration, the interactions between Co and Ns can be described as binding which is also agree with the results in the literature [24]. The available experimental data suggest that there is only one water molecule coordinating with the Co center of CoPPy and CoaPPy, and two coordinating to CoaTPy [21,24]. The water molecules coordinating to CoPPy and CoaTPy can be considered as binding because of the relatively short $d_{O_{water1}}$ and $d_{O_{water2}}$ distances. The water molecule coordinating to CoaPPy, instead, can be described as unbound, being the $d_{O_{water1}}$ 3.89 Å.

Table 4.1: Structural parameters for the optimized geometries of CoPPy, CoaPPy, and CoaTPy catalysts in gas phase. $d_{\mathrm{N_{Lpy1}}}$ is the distance between Co and $\mathrm{N_{Lpy1}}$; $d_{\mathrm{N_{Lpy2}}}$ is the distance between Co and $\mathrm{N_{Lpy2}}$; $d_{\mathrm{N_{Vpy1}}}$ is the distance between Co and $\mathrm{N_{Vpy1}}$; $d_{\mathrm{N_{Rpy1}}}$ is the distance between Co and $\mathrm{N_{Rpy1}}$; $d_{\mathrm{N_{Rpy2}}}$ is the distance between Co and $\mathrm{N_{Rpy2}}$; $d_{\mathrm{O_{water1}}}$ is the distance between O in first water molecule ($\mathrm{O_{water1}}$) and Co; and the distance between O in second water molecule ($\mathrm{O_{water2}}$) and Co is displayed with $d_{\mathrm{O_{water2}}}$. All distances are reported in Å.

Catalyst	$d_{\mathrm{N_{Lpy1}}}$	$d_{\mathrm{N_{Lpy2}}}$	$d_{\mathrm{N_{Vpy1}}}$	$d_{\mathrm{N_{Rpy1}}}$	$d_{\mathrm{N_{Rpy2}}}$	$d_{\mathrm{O_{water1}}}$	$d_{\mathrm{O_{water2}}}$
CoPPy	2.12	2.14	2.09	2.14	2.13	2.22	–
CoaPPy	2.08	2.10	2.03	2.07	2.09	3.89	–
CoaTPy	2.09	–	2.07	2.04	2.08	2.16	2.39

In this subsection we compared the geometrical parameters of CoaPPy, CoaTPy, and CoPPy in the gas phase to emphasize the differences between the distorted structures and the perfectly symmetric one. From now on, we will only consider CoaPPy and CoaTPy catalysts solvated in water environment.

4.2.2 Simulation of Bulk Water

Liquid water has been widely studied with molecular dynamics simulations using many quantum-chemical models [121–123]. However, the accurate description of its structural and electronic properties is not trivial. Due to the intensive computational effort required by AIMD runs, generally cheaper GGA density functionals, i.e. PBE, have been used in the literature for modeling bulk water. In order to properly reproduce the structural and dynamic character of the hydrogen bonding network in liquid water, it is advisable to run DFT simulations with vdW corrected functionals. Recently, Ambrosio et al. [94] carried out AIMD/NVT simulations and investigated the effects of regarding/disregarding dispersion interactions on hydrogen bonding network of bulk water using PBE and PBE-rVV10 (empirical parameter, b=9.3) density functionals. Their results are summarized in Figure 4.3. As a general observation, the inclusion of nonlocal vdW interactions improves the overall description of the structural properties of liquid water. The oxygen-oxygen radial distribution function, $g_{\mathrm{OO}}(r)$ in Figure 4.3(a) shows that the height of the first peak is larger for PBE, whereas PBE-rVV10 is closer to the experimental observations of Skinner et

al. [124]. Besides, the second shell feature is also more pronounced in the PBE $g_{OO}(r)$ meaning that PBE gives slightly more structured water with respect to PBE-rVV10. This is also confirmed by the histogram in Figure 4.3(b), which provides a comparison between the number of hydrogen bonds formed by individual molecules in the simulations based on the two different density functionals. It appears clearly that the PBE simulations at the experimental density yield important differences in the hydrogen-bond network, compared to PBE-rVV10. The percentage of molecules with four hydrogen bonds is reduced from 66% to 52% and the average number of hydrogen bonds is reduced from 3.67 to 3.59, when going from PBE to PBE-rVV10. The latter value can be compared to the experimental value of 3.58 [124]. Since the picture obtained using non-local electron correlation is closer to the experiments, we use PBE-rVV10 formalism in our AIMD simulations.

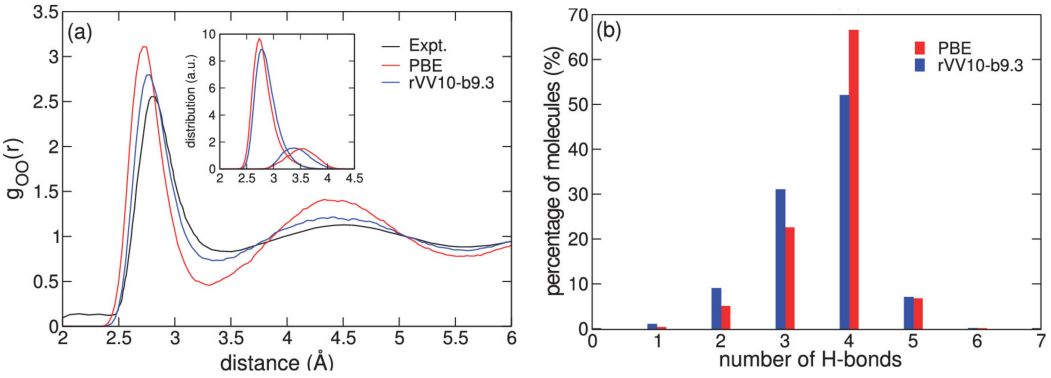

Figure 4.3: (a) Oxygen-oxygen radial distribution function, $g_{OO}(r)$, obtained through PBE and PBE-rVV10 (b=9.3) AIMD simulations at 350 K, and compared to experimental data from x-ray diffraction obtained at ambient temperature [124]. The inset shows the distribution of distances in the first coordination shell, distinguishing between the first four nearest water molecules and the fifth. (b) Distribution of water molecules according to the number of hydrogen bonds formed, as obtained from PBE and PBE-rVV10 (b=9.3) AIMD simulations. Reproduced with permission from J. Chem. Phys. **63** (2015) [94]. Copyright 2015 American Chemical Society.

4.2.3 System Size Dependence

The evaluation of redox potentials might be affected by the limitation in system size, therefore it is an important parameter in AIMD. While the water box should be large enough to avoid artifacts due to a too high concentration of the solute or too

strong spatial correlations in the solvent fluctuations, large simulation cells have an important impact on the computational effort. The minimal requirement is that the periodically repeated box is large enough such that the solute does not interact with its images, not event through long range structural rearrangements of the surrounding solvent. This can be verified by ensuring that after a certain distance from the solute molecule there is a sufficiently thick water shell behaving as bulk liquid water. Structural features that can be easily monitored in this respect is the radial distribution function and the hydrogen bonding network. The radial distribution functions presented in Figure 4.4 are computed from two simulation cells, one containing one CoaTPy catalyst in a box of 495 water molecules (relatively large system) and the other with only 215 water molecules (moderately large system). We observe that the oxygen-oxygen (g_{OO}, Figure 4.4(a)), and oxygen-hydrogen (g_{OH}, Figure 4.4(b)) radial distribution functions, computed from the bulk liquid region of the simulation cell (O at distance larger than 7 Å from catalyst) do not change significantly by changing the size of the system. On the other hand, we see some slight deviations in Co-O ($g_{\mathrm{Co-O}}$, Figure 4.4(c)) and Co-H ($g_{\mathrm{Co-H}}$, Figure 4.4(d)) radial distributions. Although the behavior obtained by two boxes is similar, the larger water box has more peaks and O and H atoms around Co atom seem more structured. However, these differences can be attributed to the shorter sampling achieved with the larger simulation cell, which could run only for 6 ps, while the sampling performed with the smaller cell is three times longer, for 18 ps. We will further extend the sampling of the larger box to improve the statistics and better evaluate the size effects. Since anyway the radial distribution functions computed for two boxes can be considered substantially equivalent, we conclude that the 215 water molecules box is sufficiently large for modeling the solvation of the catalysts addressed in this work. Therefore, we will use smaller water box containing of 215 water molecules in subsequent simulations.

4.2.4 Post-processing: Auto-correlation Function

The molecular dynamics procedure allows to generate trajectories that sample a specific statistical ensemble characterized by some given thermodynamic properties, i.e., N, V, and T. The ergodic hypothesis ensure that the sampling visits all accessible microscopic states according to the ensemble specific probability distribution and that observable macroscopic and dynamic properties can be extracted from the sampling by applying statistical mechanics. In particular, ensemble averages can be

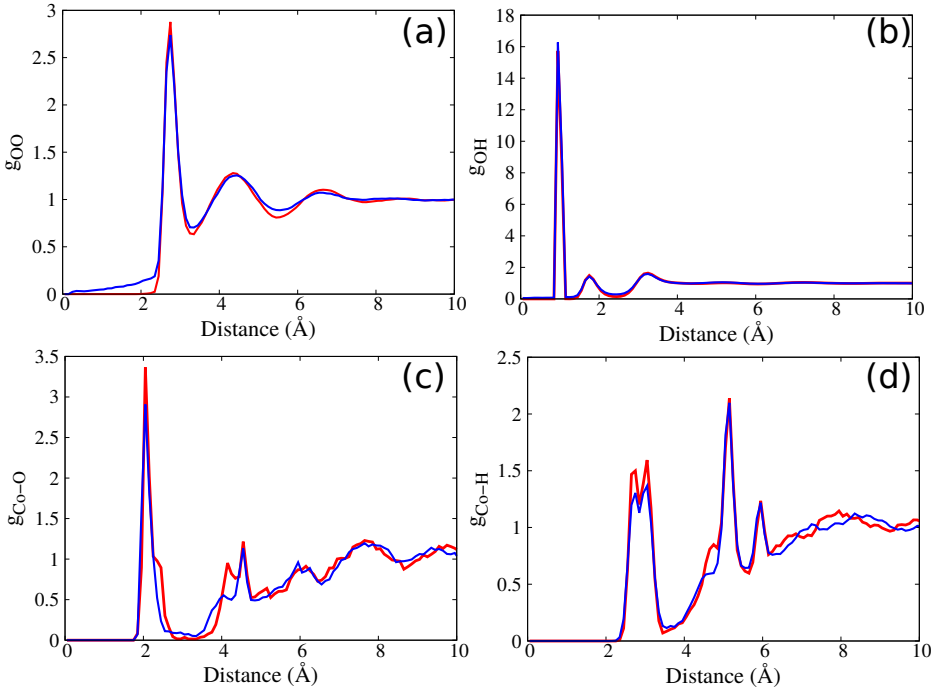

Figure 4.4: (a) Oxygen-oxygen g_{OO}, (b) oxygen-hydrogen g_{OH}, (c) cobalt-oxygen $g_{\mathrm{Co-O}}$, and (d) cobalt-hydrogen $g_{\mathrm{Co-H}}$ radial distribution functions. Red and blue solid lines are for water boxes containing 495 and 215 water molecules, respectively.

obtained as time averages over sufficiently long trajectories. This said, one recurrent issue is to determine how long the sampling should run to obtain distributions that are statistically meaningful and converged. This depends strongly on the properties of interest, since different physical quantities may have rather different fluctuations and convergence behavior. When exploring an equilibrium thermodynamic state, it is then important to monitor the properties of interest along the trajectory, considering averages and fluctuations. Since MD is a deterministic scheme and subsequent configurations along the trajectory are strongly correlated. In order to be sure that the sampling of a property is statistically relevant, the correlation between separate evaluations has to decay to zero. In other words, by evaluating the auto-correlation function of the property, it is possible to estimate the length of the correlation time interval, i.e., the time space that separates two statistically independent evaluation of the quantity.

The auto-correlation function, C_k reveals any pattern that may exist between the observation of a quantity y at two different moments along the trajectory separated

by a time interval $t{=}k{\times}\Delta t$ and it is computed from;

$$C_k = \frac{\sum_{i=1}^{n-k}(y_{k+i} - \overline{y})(y_i - \overline{y})}{\sum_{i=1}^{n}(y_i - \overline{y})^2} \tag{4.1}$$

where k is lag, y is the instantaneous value of the variable, and $\overline{y}$ is its time average. As long as time is small compared to the correlation time, the oscillation property y_i appears to be particular to the initial condition y_1, and y_{k+i} remains correlated with y_i. However, for times longer than the correlation time, the trajectory loses memory of its initial condition and y_{k+i} and y_i become uncorrelated [125].

In the present study we want to investigate the electronic properties by monitoring the fluctuations of some electronic parameters and relating them to the structural features of the solvated catalysts. Hence, we need to extract from the trajectories a statistically relevant set of configurations to be used for this analysis. The optimal distribution of the extracted snapshots can be determined by evaluating the correlation decay for some structural parameter that is closely related to the properties that we want to estimate. Indeed, the length of a correlation time depends on the nature of the system and the property under consideration. We choose the dihedral angle formed by N_{Lpy1}–N_{Vpy1}–Co–N_{Rpy1} as the structural parameter to monitor, because this has a direct relation to the electronic state of the Co center. To illustrate the approach to evaluate the decay of correlations, we take the case of solvated ^{4}(CoaTPy)^2 as an example. Figure 4.5 shows the calculated auto-correlation function versus the lag, within the range from 0 to 80. Auto-correlation function is defined as minimal if it is less than $|0.1|$. For this particular case, over a trajectory of 15 ps, we decide that choosing lag as 13 is sufficient for correlations to decay, which corresponds to a correlation time interval of 65 fs. This provides about 250 independent structures that can be used for the statistical sampling of the explored phase space. Starting from these selected snapshots, additional electronic calculations are performed, employing an higher level of theory.

4.2.5 Post-processing: Comparison of Density Functionals

The series of not-correlated snapshots discussed in the previous section is then used to refine the electronic structure properties, study the structure/electronic distribution inter-dependencies, and evaluate the redox free energies. In order to illustrate how we

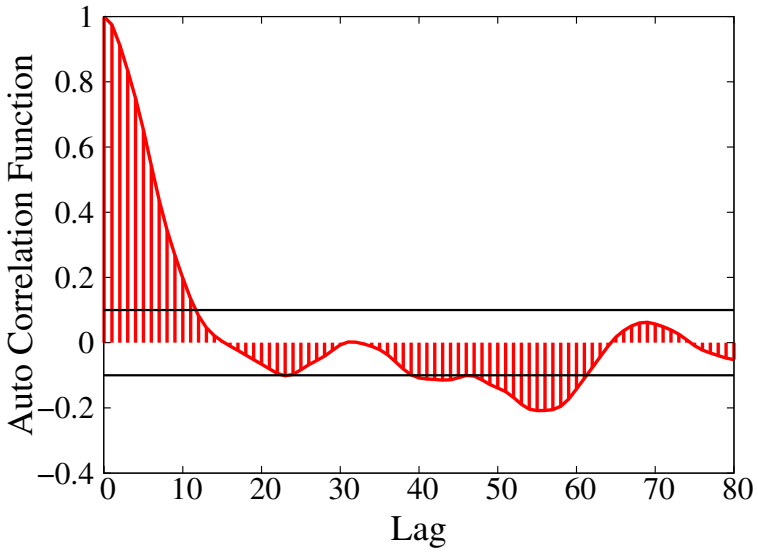

Figure 4.5: Auto-correlation function calculated for CoaTPy/water with +2 system charge and quartet multiplicity. Lag interval is chosen between 0 and 80 and auto-correlation function is calculated for each lag.

asses the methodologies to carry out these further analysis and to give the details of the used procedures, we use again CoaTPy/water as a model system. The choice of the density functional level of theory is based on the reproducibility of the homo-lumo band gap and on representation of the selected molecular orbitals. The experimental UV spectrum obtained by Rodenberg et al. [21] for CoaTPy in aqueous solution shows an intense band appearing at 305 nm, 4.06 eV, and originating from π-π^* transitions. The calculated band gap for this system using PBE-rVV10 formalism is 1.63 eV, which is significantly lower. Amrosio et al. [94] showed that hybrid density functionals, PBE0-rVV10 scheme with 0.40 exact exchange fraction, predicts the energy gap of bulk water accurately, as 8.75 eV. However, the same settings yield significantly larger band gap for the CoaTPy/water system, 5.74 eV. Therefore, we decided to tune the exact exchange scaling parameter, obtaining a good agreement with the experiments using the PBE0-rVV10 formalism with 0.25 exact exchange, 3.75 eV.

We also compare the distributions of homo and lumo of CoaTPy/water obtained with the three methods PBE-rVV10, PBE0-rVV10 with 0.40 exact exchange, and PBE0-rVV10 with 0.25 exact exchange. Some visualizations of the resulting orbitals are reported in Figure 4.6. At the PBE-rVV10 level of theory the homo is mainly distributed on Co, the pyridine nitrogens, and on the closest water molecule to the Co. The lumo, instead, is distributed on the bipyridine ring. On the other hand, both

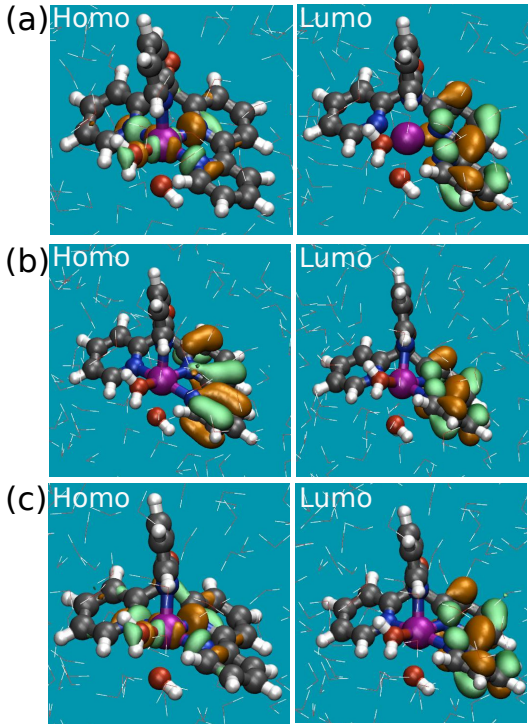

Figure 4.6: Homo and lumo molecular orbitals of optimized $^{4}(\text{CoaTPy})^{+2}$/water obtained using different density functionals, (a) PBE-rVV10, (b) PBE0-rVV10 with 0.40 exact exchange, and (c) PBE0-rVV10 with 0.25 exact exchange. Color code: gray: C, white: H, purple: Co, blue: N, red: O. While the catalyst is illustrated with ball and stick representation, solvent molecules are shown with lines. Isosurface (green for positive and orange for negative) is set to ± 0.04 e/Å^3.

homo and lumo are distributed over the bipyridine ring using PBE0-rVV10 with 0.40 exact exchange. Although, calculated band gaps using PBE-rVV10 and PBE0-rVV10 formalism with 0.25 exact exchange are significantly different, we do not observe significant changes in localization of molecular orbitals obtained from these density functionals. The orbitals obtained using PBE0-rVV10 with 0.25 exact exchange are instead very similar to the PBE-rVV10 results, in spite of the significant difference in the energy gap.

Further assessment of the density functional models in determining the relative stability of triplet and singlet states. Using time–dependent DFT (TDDFT) calculations, Rodenberg et al. [21] determined the band gaps of $^{3}(\text{CoaTPy})^{+1}$/water and $^{1}(\text{CoaTPy})^{+1}$/water as 3.54 eV and 3.09 eV, respectively. Our calculations using PBE0-rVV10 with 0.25 exact exchange formalism are in good agreement with these

previous results, yielding band gaps of 3.55 eV and 2.82 eV for triplet and singlet spin states, respectively.

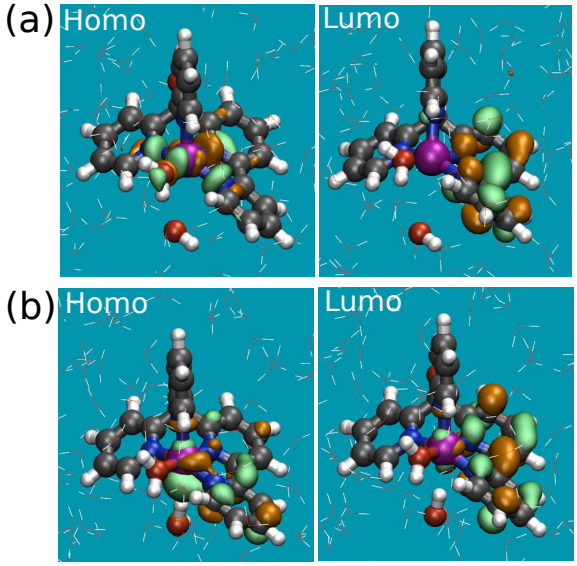

Figure 4.7: Homo and lumo molecular orbitals of optimized $(CoaTPy)^{+1}$/water for two spin states, (a) triplet and (b) singlet. Color code: gray: C, white: H, purple: Co, blue: N, red: O. While the catalyst is illustrated with ball and stick representation, solvent molecules are shown with lines. Isosurface (green for positive and orange for negative) is set to ± 0.04 e/Å^3.

Figure 4.7 shows the homo and lumo representations obtained for $(CoaTPy)^{+1}$/water in both spin states. In triplet spin state, similar to what observed for the $^4(CoaTPy)^{+2}$/water system the homo is localized on Co, pyridine nitrogens, and the closest water molecule to the Co. The lumo is on the bipyridine ring. In singlet spin state, homo is more delocalized on Co, N_{Vpy1}, and bipyridine ring and the lumo is distributed over both bipyridine ring and Co center.

As a summary, we compared the effects of GGA and two PBE0 schemes with different exact exchange fractions on a few electronic characters of the $^4(CoaTPy)^{+2}$/water system. The general outcome is that the PBE0-rVV10 scheme with 0.25 exact exchange better reproduces the experimental observations. We further tested this density functional on $(CoaTPy)^{+1}$/water system for both triplet and singlet states. The corresponding results capture the previously calculated TDDFT results relatively good. Therefore, we will use PBE0-rVV10 with 0.25 exact exchange for calculating electronic structure properties of the selected AIMD snapshots and redox free energies.

4.2.6 Computation of Redox Potential

In this subsection we summarize the procedure to calculate the redox potential for an electron injection step of the catalytic cycle. To illustrate the methodology, the first step in the CoaTPy cycle is taken as an example. The reduction reaction under consideration is as follows

$$^{4}(\text{CoaTPy})^{+2} + e^{-} \rightarrow \ ^{1}(\text{CoaTPy})^{+1}$$

This is a half reaction, where the number of electrons varies between n, for the reduced state R, and n-1, for the oxidized state O. The AIMD simulation can be employed to sample both states, i.e, the reduced state R or the oxidized state O. As explained above, from each trajectory a statistically meaningful selection of snapshots can be extracted for the post-processing.

In order to determine the redox potential for the electron injection reaction, we need to compute the free energy difference between the two states. However, the two individual trajectories do not simply provide these information, since they are independent sampling of the phase space that cannot be directly compared. Several methods have been developed to extrapolate estimates of free energy differences among thermodynamic states from molecular dynamics simulations. For the specific case of interest here, the preferred choices are the Free energy perturbation scheme or equivalently the thermodynamic integration [126, 127]. In practice, these consist in running trajectories at different intermediate states, between the two end states R and O, and sampling on the resulting ensemble of configurations the potential energy derivative with respect to the fluctuation in the reaction coordinate, that in this case is the number of electrons. The underlying idea is that the potential energy of the system is related to the free energy difference, ΔA, via [126]

$$\Delta A = A_1 - A_0 = \int_0^1 \frac{\partial A(\eta)}{\partial \eta} d\eta = \int_0^1 \left\langle \frac{\partial E(\eta, r)}{\partial \eta} \right\rangle_{\eta} d\eta \tag{4.2}$$

where η is a coupling parameter and E is the potential energy of the system. The integral of the average derivative of the potential energy function with respect to the coupling parameter (or reaction coordinate) provides an estimate of the free energy difference between the two end points. In the present case, we assume that we can linearize this integral and sample only one of the two states, R or O. Over the generated trajectory, the derivative of the energy for a change in the number of electrons

$\Delta n = 1$ is the vertical energy gap as shown below.

$$\frac{\partial E(\eta, r)}{\partial \eta} = E_1(r) - E_0(r) = \Delta E(r) \tag{4.3}$$

$E_1(r)$ and $E_0(r)$ are the total potential energies of two end states R and O, respectively, at the same instantaneous configuration r. The integral then reduces to one single term, which is the average of ΔE sampled over the trajectory. This approximation also assume a linear response of the solvent to the electron transfer, and it is part of the Marcus theory [128]. $\langle \Delta E \rangle_R$ denotes the ensemble average of the vertical energy gap obtained by sampling the potential energy surface of the reduced state R, while $\langle \Delta E \rangle_O$ corresponds to the average of the vertical gap sampled over the configurations generated with the Hamiltonian for the oxidized state, O. In order to improve the estimate of the free energy difference, both sampling have to be taken into account and the following average is computed.

$$\Delta_{red} A = \frac{\langle \Delta E \rangle_R + \langle \Delta E \rangle_O}{2} \tag{4.4}$$

Equation 4.4 implies that under linear response the free energy difference is equal to the canonical average of the ionization energy and electron affinity. This assumption enables us to obtain redox free energy from only two equilibrium molecular dynamics runs. In addition to this, the solvent response can be described by a quantity called reorganization free energy, λ, which can be estimated as the difference of the mean energy gaps

$$\lambda = \frac{\langle \Delta E \rangle_R - \langle \Delta E \rangle_O}{2} \tag{4.5}$$

Before using Equations 4.4 and 4.5 one should check if the assumption of the linear response of the solvent applies for the systems under consideration. A necessary condition for a linear solvent response is that the probability distributions of the energy gaps in the two end states have a Gaussian shape characterized by the same width, i.e. the samplings of the vertical energy gaps in the two end states R and O have the same variance [129]. This implies that in the linear regime the free energy curves are parabola with equal curvatures, the variances of the distributions are equal, $\sigma^2_{\mathrm{R}} = \sigma^2_{\mathrm{O}}$, and as a consequence the reorganization free energies of R and O states are also equal, $\lambda_R = \lambda_O = \lambda$, as shown below

$$\lambda = \lambda_R = \frac{\sigma_R^2}{2k_B T} = \lambda_O = \frac{\sigma_O^2}{2k_B T} \tag{4.6}$$

In summary, we first compare the variances of the distributions for both R and O states to check if the solvent response is linear. Then, we use Equation 4.4 and

Equation 4.6 to calculate the reduction free energy and solvent reorganization energy, respectively.

4.3 Results and Discussion

Before starting AIMD runs of intermediate states towards H_2 production, we first equilibrate initial state of both systems, aqueous ^{4}(CoaPPy)$^{+2}$ and ^{4}(CoaTPy)$^{+2}$. As suggested by the geometry optimizations carried out in vacuum, AIMD production run confirms that there are two water molecules of ^{4}(CoaTPy)$^{+2}$, at average distances of 2.07 and 2.33 Å. The average distances between the pyridine nitrogens and Co range between 2.06 and 2.13 Å, being $d_{\mathrm{N_{Rpy1}}}$ the shortest one. The average angle between $\mathrm{N_{Lpy1}}$, C atom connecting two pyridine rings, and $\mathrm{N_{Rpy1}}$ is 113º. This angle can give some hint on the accessibility of the Co center during the following steps of the reaction cycle.

In the case of ^{4}(CoaPPy)$^{+2}$/water, the interaction with the solvent effects induces substantial changes in the structure of the catalyst with respect to the optimized geometry in vacuum. One water molecule is very loosely coordinating to the Co center at an average $d_{\mathrm{O_{water1}}}$ around 4.87 Å. On the other hand, a second water molecule approaches the Co center even though the interaction is apparently quite weak, since it shows a rather diffusive behavior, while the distance from Co fluctuates between ≈2.3 and ≈5 Å within a few picoseconds. The distances separating the pyridine N and Co are slightly shorter than what observed for ^{4}(CoaTPy)$^{+2}$, ranging between 2.04 and 2.08 Å. Additionally, the angle between the pyridine rings is also slightly narrower, being 109º. This implies that the two bipyridine units are more bended in ^{4}(CoaPPy)$^{+2}$ with respect to ^{4}(CoaTPy)$^{+2}$, which might hinder the accessibility of the Co center by water molecules.

In the next section we discuss the solvent response as well as the structural changes of the catalysts at each intermediate step of the reaction cycle, i.e. the subsequent electron injection and protonation steps.

4.3.1 Solvent Response

The first electron injection to both ^{4}(CoaTPy)$^{+2}$ and ^{4}(CoaPPy)$^{+2}$ systems may lead to two different spin states, triplet and singlet. Moreover, the electron injection should favor the interaction between the Co center and the protons from the solution,

therefore we expect changes in the structure of the solvation shell around the Co center.

Considering triplet spin state of CoaTPy, ^{3}(CoaTPy)$^{+1}$, O_{water1} preserves its position fluctuating around 2.23 Å as shown in Figure 4.8(a). The distance between the nearest solvent H and the Co center, $d_{H_{water2}}$, is relatively long fluctuating around 3.42 Å. The behavior is similar in ^{3}(CoaPPy)$^{+1}$, see Figure 4.8(d), where the average $d_{O_{water1}}$ and $d_{H_{water2}}$ are at 5.22 and 4.10 Å respectively. On the other hand, in the singlet spin state, first solvation shell undergoes a significant rearrangement. In the case of ^{1}(CoaTPy)$^{+1}$, although the closest water molecule remains substantially at the same distance, we observe an abrupt change in coordination of the second closest water molecule after 5 ps of simulation time, see Figure 4.8(b). The water molecule rotates and H_{water2} coordinates with the Co center, as illustrated in Figure 4.8(c), yielding a shorter $d_{H_{water2}}$ of 2.5 Å. In the case of ^{1}(CoaPPy)$^{+1}$, we also observe a similar solvent rearrangement, where the second water approaches the Co center and the distance $d_{H_{water2}}$ changes from 4.5 Å to 2.63 Å. These rearrangements characterizing the singlet spin state suggest that the hydrogen bonding network around the solute has been modified and connects the molecular center to the bulk solvent. This might explain the experimental observation that H_2 production reaction is actually occurring in the singlet spin state [21]. Hence the next step that we study is the protonation of the singlet spin state.

The insertion of a proton close to the Co center creates a cobalt-hydride and the total charge changes from +1 to +2. For ^{1}(CoaTPy-H)$^{+2}$, the distance between Co and proton, $d_{Co\text{-}H^+}$, oscillates around 1.48 Å. While the water molecule that was previously coordinated to Co via the hydrogen is now displaced and interacts directing with the proton, at a distance $d_{H_{water2}\text{-}H^+}$ oscillating around 1.75 A, see Figure 4.9(a) and (b). In the case of ^{1}(CoaPPy-H)$^{+2}$, the $d_{Co\text{-}H^+}$ is also around 1.46 Å, but the second closest water molecule seems not to stably interact with the proton, being the average $d_{H_{water2}\text{-}H^+}$ distance larger than 3.2 Å, see Figure 4.9(c) and (d). These results suggest that the Co center is more accessible in CoaTPy with respect to CoaPPy, which might explain the enhanced performance observed for CoaTPy towards H_2 production.

Following the second electron injection to the Co-hydride, both systems are expected to become more prone to grab a proton from the solvent and generate H_2. The spin state becomes doublet and total charge of the systems changes from +2 to +1. For ^{2}(CoaTPy-H)$^{+1}$, the interactions between H_{water2} and H^+ become stronger

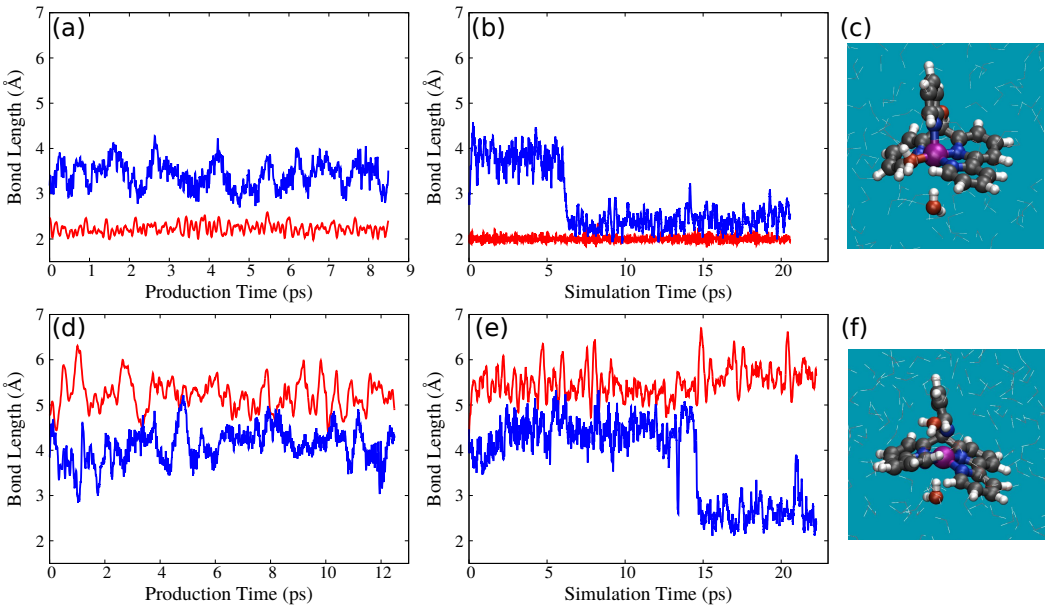

Figure 4.8: Fluctuating $d_{\mathrm{O_{water1}}}$ (red) and $d_{\mathrm{H_{water2}}}$ (blue) distances along AIMD trajectory for (a) ^{3}(CoaTPy)$^{+1}$, (b) ^{1}(CoaTPy)$^{+1}$, (d) ^{3}(CoaPPy)$^{+1}$, and (e) ^{1}(CoaPPy)$^{+1}$. (c) and (f) illustrate selected AIMD snapshots for ^{1}(CoaTPy)$^{+1}$ and ^{1}(CoaPPy)$^{+1}$, respectively. Color code: gray: C, white: H, purple: Co, blue: N, red: O. While the catalysts are illustrated with ball and stick representation, solvent molecules are shown with lines.

with respect to ^{1}(CoaTPy-H)$^{+2}$. While $d_{\mathrm{H_{water2}\text{-}H^{+}}}$ becomes shorter, 1.48 Å, $d_{\mathrm{Co\text{-}H^{+}}}$ becomes slightly larger, 1.50 Å, see Figure 4.10(a) and (b). The behavior is similar for ^{2}(CoaPPy-H)$^{+1}$, see Figure 4.10(c) and (d), where shorter $d_{\mathrm{H_{water2}\text{-}H^{+}}}$ and slightly larger $d_{\mathrm{Co\text{-}H^{+}}}$ are obtained as 2.42 and 1.47 Å, respectively. The $d_{\mathrm{H_{water2}\text{-}H^{+}}}$ is significantly shorter in CoaTPy with respect to CoaPPy, which once more hints to a more favorable environment for the reduction reaction.

As soon as we add second proton to the Co-hydride, the H_2 production cycle is closed. Both systems spontaneously return back to their initial state having quartet spin state and +2 total charge. Figure 4.11(a) and (b) illustrate AIMD snapshots taken from the equilibration of the solvated ^{4}(CoaTPy)$^{+2}$-H_2 and ^{4}(CoaPPy)$^{+2}$-H_2 systems, respectively. The additional proton is supposed to be transferred from the surrounding water environment through proton hopping. When this happens, H_2 is formed it moves away from the Co center. This happens a little bit faster for CoaTPy, in 770 fs vs. 3.5 ps of simulation time for CoaPPy. This result presumably thanks to the presence of the H-coordinating water molecule at CoaTPy. The formation

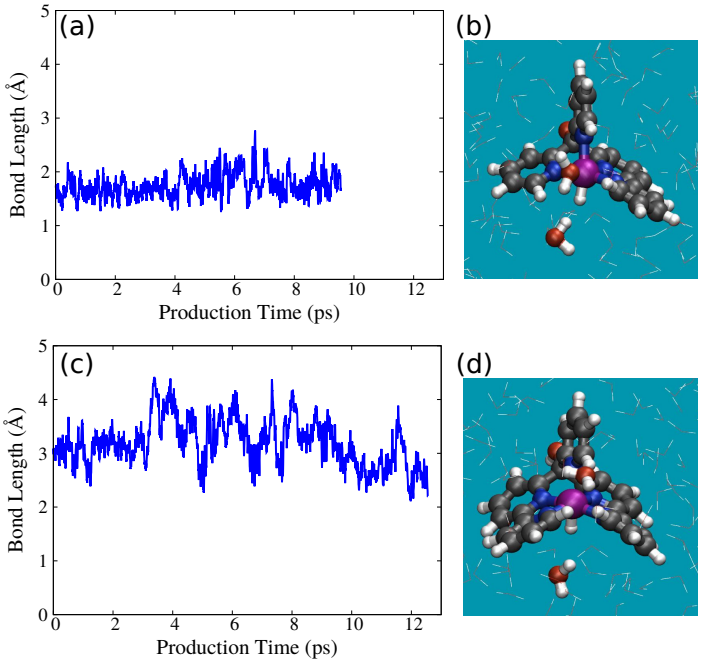

Figure 4.9: Fluctuating $d_{\mathrm{H_{water2}\text{-}H^{+}}}$ distances along AIMD trajectory for (a) ^{1}(CoaTPy-H)$^{+2}$ and (c) ^{1}(CoaPPy-H)$^{+2}$. (b) and (d) illustrate selected AIMD snapshots for ^{1}(CoaTPy-H)$^{+2}$ and ^{1}(CoaPPy-H)$^{+2}$, respectively. For the color code, see previous figures.

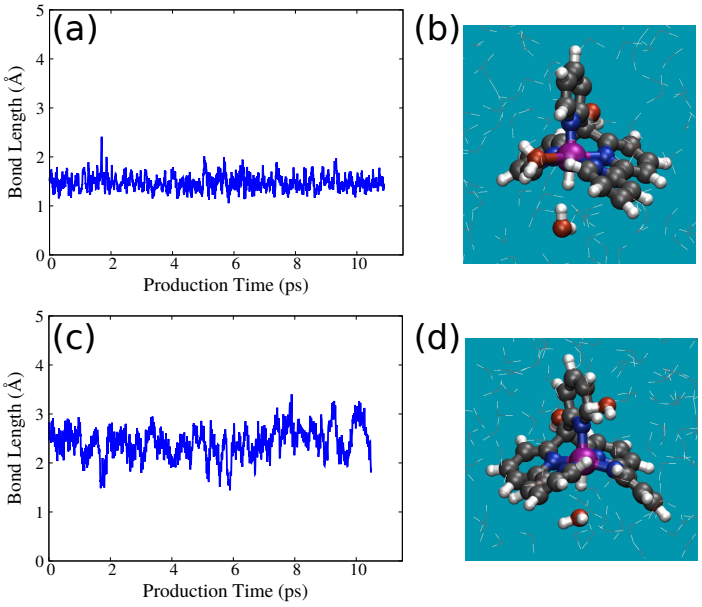

Figure 4.10: Oscillating $d_{\mathrm{H_{water2}\text{-}H^{+}}}$ distances along AIMD trajectory for (a) ^{2}(CoaTPy-H)$^{+1}$ and (c) ^{2}(CoaPPy-H)$^{+1}$. (b) and (d) illustrate selected AIMD snapshots for ^{2}(CoaTPy-H)$^{+1}$ and ^{2}(CoaPPy-H)$^{+1}$, respectively. For the color code, see previous figures.

of H_2 and the consequent change in the oxidation state of Co, also determine the rearrangement of the water environment towards the initial conditions.

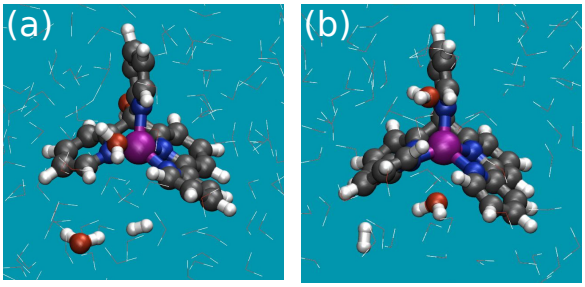

Figure 4.11: Selected AIMD snapshots of H_2 formation in (a) ^{4}(CoaTPy)$^{+2}$-H_2 after 14 ps and (b) ^{4}(CoaPPy)$^{+2}$-H_2 after 5 ps of simulation time. For the color code, see previous figures.

In this subsection, we discussed the characteristics of the solvation shell rearrangements observed at each intermediate step of the reduction cycle. The next section focuses on the observed catalysts conformational changes, to shed some light on the effects of the ligand type on H_2 production performance.

4.3.2 Structural Changes in Catalysts

We observe some changes in catalysts' structures associated with the subsequent electron injection, , the protonation, and the solvent response. The resulting average distances and angle between the pyridine rings obtained through AIMD trajectories are characterized by $d_{N_{Lpy1}}$, $d_{N_{Lpy2}}$, $d_{N_{Vpy1}}$, $d_{N_{Rpy1}}$, $d_{N_{Rpy2}}$, and A_{CCC} as reported in Table 4.2. The average values are calculated over the production runs of ≈15 ps. Similar to the observations in the vacuum phase, in initial state pyridine Ns-Co distances in CoaPPy are slightly shorter than in CoaTPy. The ligand environment in CoaPPy is more bended, i.e. A_{CCC} measured in CoaPPy is slightly narrower than in CoaTPy. After the first electron injection, all pyridine Ns move towards to the Co center, forming a more compact molecular pocket. This is observed for both triplet and singlet states. Even though the effect is more pronounced in the singlet state. While we observe ≈0.17 Å change in $d_{N_{Vpy1}}$ for ^{1}(CoaTPy)$^{+1}$, interestingly no significant change of this parameter is recorded in the case of ^{1}(CoaPPy)$^{+1}$. The motion of the pyridine Ns towards the catalytic center enhances the deformation in ^{1}(CoaTPy)$^{+1}$, whereas the opposite effect is observed in ^{1}(CoaPPy)$^{+1}$, where the angle between the pyridine units increases with respect to the initial state of the catalyst.

Table 4.2: Structural parameters characterizing the initial states as well as five distinct intermediate states of both CoaTPy and CoaPPy immersed in water. All distances are given in Å, whereas the angle between pyridine units, A_{CCC}, is given in degree.

Reaction Steps	Formula	$d_{\mathrm{N_{Lpy1}}}$	$d_{\mathrm{N_{Lpy2}}}$	$d_{\mathrm{N_{Vpy1}}}$	$d_{\mathrm{N_{Rpy1}}}$	$d_{\mathrm{N_{Rpy2}}}$	A_{CCC}
CoaTPy							
Initial state	^{4}(CoaTPy)$^{+2}$	2.13	–	2.13	2.06	2.13	113.10
1$^{\mathrm{st}}$ reduction	^{3}(CoaTPy)$^{+1}$	2.02	–	2.02	1.92	2.03	112.66
1$^{\mathrm{st}}$ reduction	^{1}(CoaTPy)$^{+1}$	2.07	–	1.96	1.85	1.87	109.11
1$^{\mathrm{st}}$ protonation	^{1}(CoaTPy-H)$^{+2}$	1.95	–	2.03	1.87	1.93	109.83
2$^{\mathrm{nd}}$ reduction	^{2}(CoaTPy-H)$^{+1}$	1.96	–	1.99	1.95	2.03	110.06
2$^{\mathrm{nd}}$ protonation	^{4}(CoaTPy)$^{+2}$-H_2	2.06	–	2.07	2.09	2.08	109.32
CoaPPy							
Initial state	^{4}(CoaPPy)$^{+2}$	2.04	2.08	2.05	2.07	2.08	109.40
1$^{\mathrm{st}}$ reduction	^{3}(CoaPPy)$^{+1}$	1.97	2.04	2.03	1.96	2.06	108.67
1$^{\mathrm{st}}$ reduction	^{1}(CoaPPy)$^{+1}$	1.88	1.91	2.05	1.88	1.91	111.04
1$^{\mathrm{st}}$ protonation	^{1}(CoaPPy-H)$^{+2}$	1.88	1.95	2.05	1.89	1.96	109.80
2$^{\mathrm{nd}}$ reduction	^{2}(CoaPPy-H)$^{+1}$	1.88	1.95	2.10	1.88	1.97	109.56
2$^{\mathrm{nd}}$ protonation	^{4}(CoaPPy)$^{+2}$-H_2	2.05	2.08	2.04	2.06	2.11	108.53

The first protonation leads to the relaxation of the pyridine nitrogens, resulting in the general elongation of the N-Co distances, We observe a minor increase in A_{CCC} for CoaTPy, contrarily it decreases in the case of CoaPPy. The second electron injection does not result in any significant structural changes regarding the distances between Co and the pyridine Ns as well as A_{CCC}. The H_2 production cycle is closed with the second protonation and the catalyst is restored in its initial state.

4.3.3 Electronic Structure Analysis

The structural rearrangements are expected to be associated to some response also in the electronic structure. Therefore it is interesting to monitor the evolution of some selected electronic structure parameter at the different states along the reaction cycle. Here we consider only the initial state and one of the intermediate states of the cycle, i.e., the system after the first reduction process in the singlet spin state. Figure 4.12(a) shows the fluctuations of the ^{4}(CoaTPy)$^{+2}$ band gap around the average value of 3.9 eV. The integrated spin density has an average value of 2.75 and it is mainly localized on the Co center with some contributions also on pyridine Ns, see Figure 4.12(b) and (c). The fluctuations of the gap are combined with a redistribution of the molecular

orbitals. In particular we notice that the homo is affected even by slight structural conformational changes. To illustrate this behavior we analyze the homo and lumo distributions of three snapshots, corresponding to a minimum, an average, and a maximum value of the energy gap. These are taken at 4.86 ps, 7.86 ps, and 8 ps, respectively. At 4.86 ps the homo is distributed over Co and Ns except for N_{Vpy1}. At 7.86 ps the homo is mainly on the pyrine ring at axial direction with contributions also localized on the Co, N_{Rpy1}, and N_{Rpy2} atoms. Moreover a small contribution is detected also on the O_{water2} for the snapshot obtained at 8 ps where the band gap is larger than its average value. Except for the slight differences observed in homo representations, the lumo, instead, seems not to be substantially affected by the fluctuations in this equilibrium state, and its distribution remains constantly principally localized.

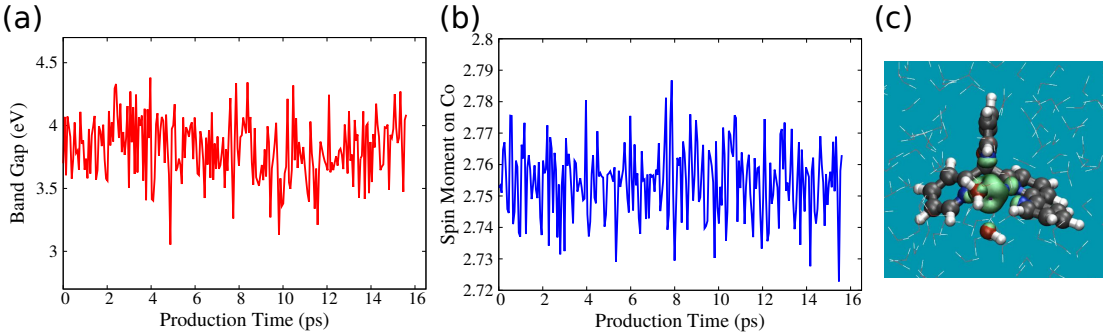

Figure 4.12: Electronic structure analysis carried out for $^{4}(CoaTPy)^{+2}$. Fluctuations in calculated band gap and spin moment on Co are depicted in (a) and (b), respectively. (c) Spin density of $^{4}(CoaTPy)^{+2}$. Isosurface is taken at 0.002 e/Å^3.

After the first electron injection, the band gap of the CoaTPy catalyst decreases in average by ≈0.5 eV. The average integrated spin density, which is still localized on the Co center, is around 0.92, see Figure 4.14. Here, we assume that electron injection process, from PS to the catalyst, is very fast and atomic rearrangement and solvent response are relatively slow, hence at the instant of electron injection the atoms in $^{4}(CoaTPy)^{+2}$ preserve their coordinates. In order to illustrate the relation between the structural and the electronic fluctuations, we selected three snapshots, at 0.6 ps, 8 ps, and 13.8 ps, corresponding to a maximum (4.2 ev), average (3.4 eV), and minimum (2.7 eV) value of the energy gap. The selected molecular orbitals of $^{1}(CoaTPy)^{+1}$ are illustrated in Figure 4.15. Homo distributions are very similar for three snapshots, where it is mainly located on Co, the pyridine Ns, and the second closest water molecule to the Co. On the other hand, the lumo state, shown only for the snapshot at 0.6 ps, is distributed over solvent molecules which implies that the

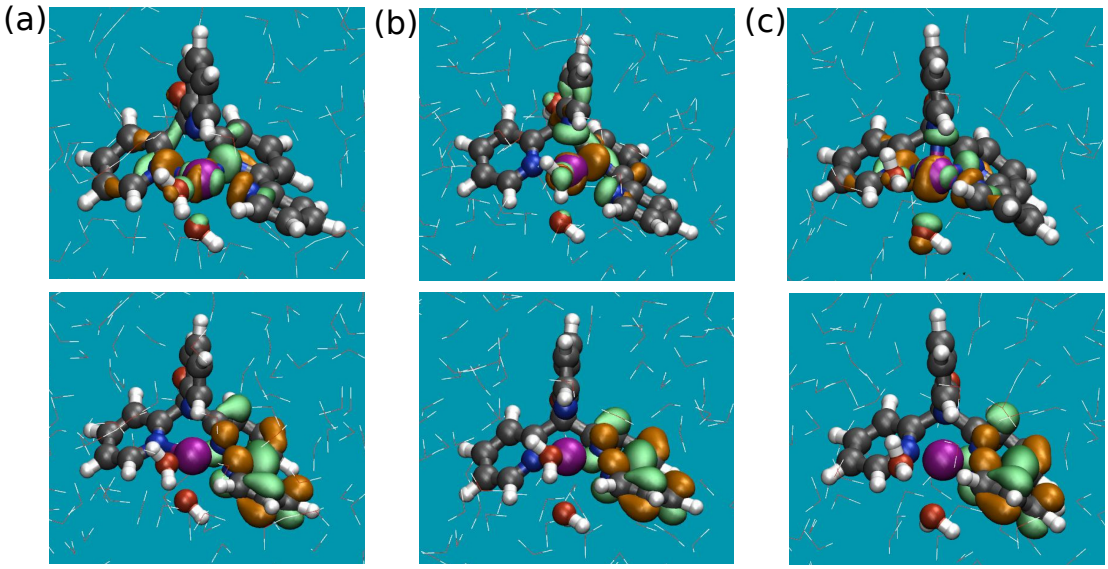

Figure 4.13: Homo and lumo representations for $^{4}(CoaTPy)^{+2}$ obtained at (a) 4.86 ps, (b) 7.86 ps, and (c) 8 ps. While all the top figures show homo, bottom ones illustrate lumo representations. Isosurface (green for positive and orange for negative) is set to ± 0.04 e/Å^3.

next reaction step should be protonation, as the experimentalists suggest rather than subsequent second electron injection.

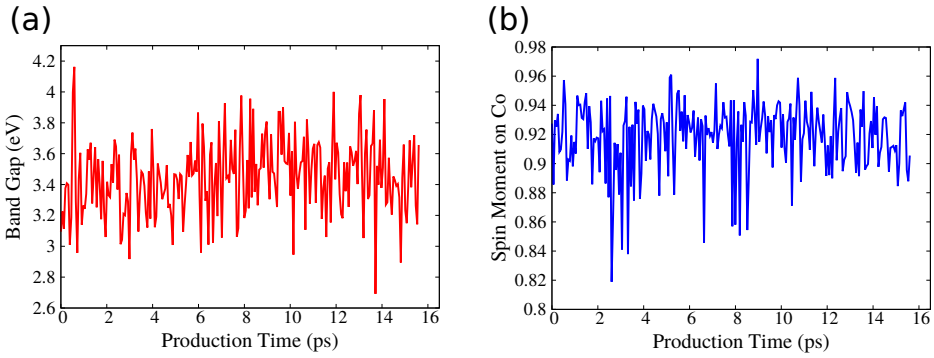

Figure 4.14: Electronic structure analysis carried out for $^{1}(CoaTPy)^{+1}$ at the same coordinates as $^{4}(CoaTPy)^{+2}$. Fluctuations in calculated band gap and spin moment on Co are depicted in (a) and (b), respectively.

The band gap of $^{4}(CoaPPy)^{+2}$, in its equilibrium state, fluctuates around 3.7 eV being ≈0.2 eV lower than what calculated for $^{4}(CoaTPy)^{+2}$, see Figure 4.16(a). As Figure 4.16(b) shows the spin density localizes mainly on the Co with an average value of 2.73. At 4.8 ps we observe a slight decrease in the spin state of Co, however as Figure 4.16(c) shows it still mainly localizes on the Co center.

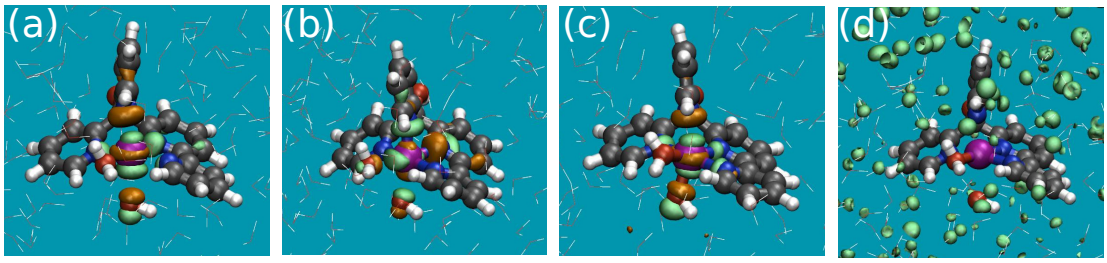

Figure 4.15: Homo representations for $^{1}(CoaTPy)^{+1}$ obtained at (a) 0.6 ps, (b) 8 ps, and (c) 13.8 ps. (d) Lumo obtained at 0.6 ps. Isosurface (green for positive and orange for negative) is set to ± 0.04 e/Å^3.

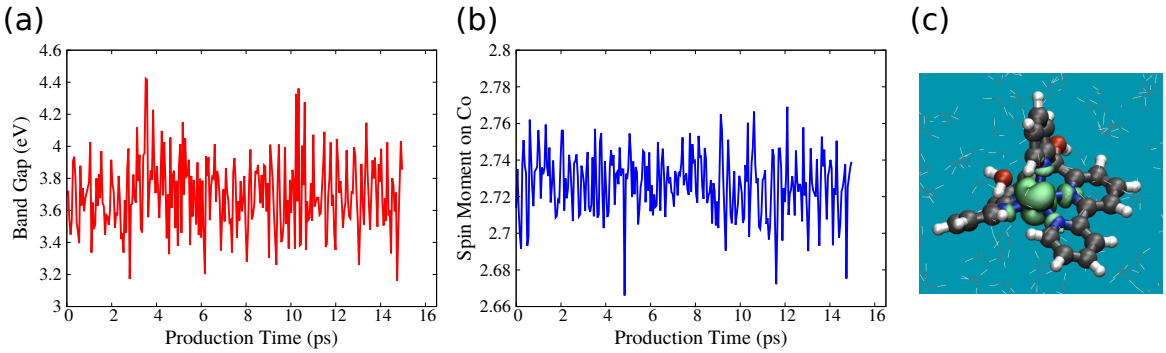

Figure 4.16: Electronic structure analysis carried out for $^{4}(CoaPPy)^{+2}$. Fluctuations in calculated band gap and spin moment on Co are depicted in (a) and (b), respectively. (c) Spin density of $^{4}(CoaPPy)^{+2}$ at 4.8 ps. Isosurface is taken at 0.002 e/Å^3.

Selected molecular orbitals of $^{4}(CoaPPy)^{+2}$ are illustrated in Figure 4.17. We observe very similar distribution of homo states, obtained at 8.6 and 14.7 ps, with respect to the $^{4}(CoaTPy)^{+2}$ system. The lumo is generally localized on only one bipyridine ring at 8.6 ps, while it is distributed over both bipyridines at 14.7 ps. Lumo distribution on both bipyridine units results in a smaller energy gap, 3.14 eV, instead of 3.66 eV energy gap observed at 8.6 ps, see Figure 4.16(a).

To explore the sudden changes in the electronic structure after the first electron injection, we employ the same procedure as before, and simply recalculate the electronic structure with one additional electron, for the same structure sampled at the equilibrium state. The average energy gap decrease by 2.1 eV, see Figure 4.18. This amount of decrease is more pronounced than $^{4}(CoaTPy)^{+2}$ case where we only observe 0.2 eV of reduction in the band gap. Besides, at 12.9 ps we observe an abrupt drop in the calculated homo-lumo gap which becomes to 0.46 eV. In order to shed light on this sudden change, we analyze and compare the homo and lumo distributions at 12.9

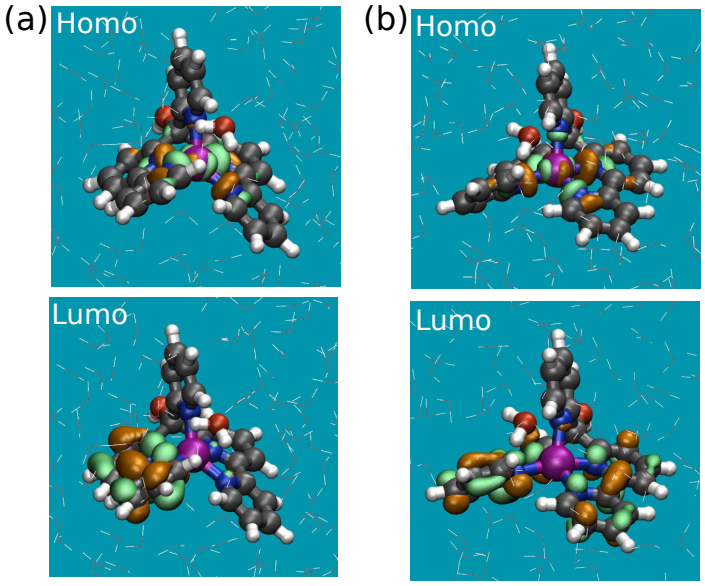

Figure 4.17: Homo and lumo representations for ^{4}(CoaPPy)$^{+2}$ obtained at (a) 8.6 ps and (b) 14.7 ps. While all the top figures show homo, bottom ones illustrate lumo representations. Isosurface (green for positive and orange for negative) is set to ± 0.04 e/Å^3.

ps and at 14.9 ps, see Figure 4.18(b) and (c). While the homo is located on Co and pyridine Ns at 12.9 ps, it mainly localizes on the Co center at 14.9 ps. The lumo, on the other hand, delocalizes over all bipyridine units as well as Co center at 12.9 ps. The behavior obtained at 14.9 ps is, instead, similar to the previous cases, where the localization of lumo over only one bipyridine ring is observed.

4.3.4 Reduction Free Energies

The reduction free energy of CoaTPy after the first electron injection is computed by the accumulative time averages of the vertical energy gaps, $\overline{\Delta E}$, in the reduced, ^{1}(CoaTPy)$^{+1}$, and the oxidized states, ^{4}(CoaTPy)$^{+2}$, as described above. Running averages of the $\overline{\Delta E}$, plotted in Figure 4.19(a), converge at the values of -0.75 and -3.14 eV, for the reduced and oxidized limit, respectively. Using Equation 4.4, the reduction free energy of CoaTPy, $\Delta_{red}A$, is is estimated to be -1.95 eV. We also check if our assumption, i.e. linear solvent response, holds for this particular case. The distributions of the vertical energy gaps of the reduction reaction are plotted in Figure 4.19(b), together with a Gaussian fit. The standard deviations of the two Gaussian distributions are obtained as 0.27 and 0.24 eV for the reduced and oxidized limit, respectively. Besides, the reorganization free energies for the reduced, λ_R, and

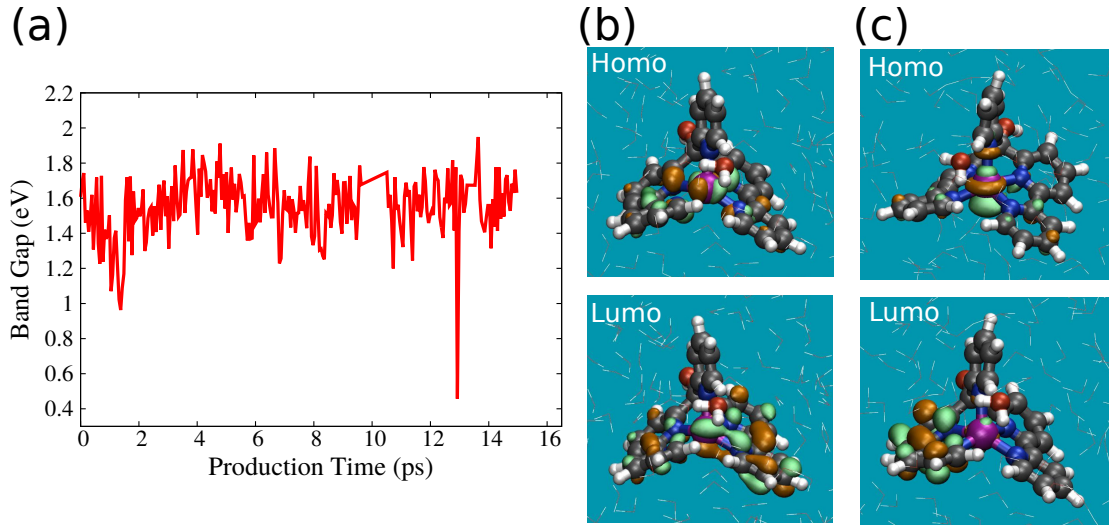

Figure 4.18: Electronic structure analysis carried out for $^{1}(\text{CoaPPy})^{+1}$. (a) Fluctuations in calculated band gap. Homo and lumo representations for $^{1}(\text{CoaPPy})^{+1}$ obtained at (b) 12.9 and (c) 14.9 ps. Isosurface (green for positive and orange for negative) is set to ± 0.04 e/Å^3.

oxidized states, λ_O, are calculated as 1.30 and 1.02 eV, respectively. A minor variation in the standard deviations of the two Gaussian distributions, 0.03 eV, yields only slightly different reorganization free energies. We, therefore, can confidently confirm that linear regime holds for this reaction and the calculated reduction free energy is reliable.

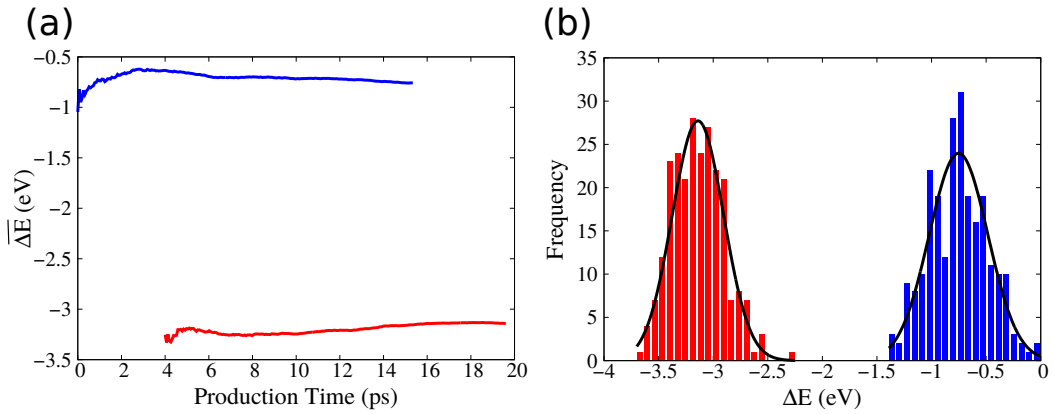

Figure 4.19: (a) Accumulative time averages of the vertical energy gaps of the reduction reaction, $^{4}(\text{CoaTPy})^{+2} + e^{-} \rightarrow {}^{1}(\text{CoaTPy})^{+1}$. While reduced limit is shown with blue, oxidized limit is depicted with red solid line. (b) Distributions of the vertical energy gaps of the reduction reaction with Gaussian distributions fitted to the data (black solid line).

4.4 Conclusion

We have studied H_2 production mechanism of differently ligated Co-based polypyridyl catalysts, CoaTPy and CoaPPy, in explicit water environment. The effects of the number of pyridyl units, strongly distorted structures, and coordination environment around Co center on the reaction mechanism have been investigated by monitoring solvent response and structural changes occurring at each step of the catalytic cycle. To this purpose we employ AIMD simulations by extending the production trajectories over tens of picoseconds in order to properly sample the structural rearrangements. The free energy changes associated with the reduction steps are evaluated within the framework of Marcus theory, using a well established procedure based on the perturbation free energy formalism.

Our results indicate that the Co center is more accessible by protons present in the solvent molecules in CoaTPy with respect to the CoaPPy. This behavior is attributed to the reduced steric hindrance effects created by the four pyridine rings in comparison to the five in the CoaPPy structure. The examples can be readily seen after the first electron injection, where water proton more rapidly and stably coordinates to the Co center in CoaTPy comparing to the CoaPPy. Moreover, we observe that after the second step in the catalytic cycle, the CoaTPy/water system attracts protons present in the solvent stronger than CoaPPy/water. At the final catalytic step, the formed H_2 moves rapidly away from the Co center. Also this rearrangement appears to be faster for the CoaTPy because of the more flexible ligand environment. All these results suggest that the more open catalytic pocket of CoaTPy favours the interaction with the solvent and the attraction of protons as well as the formation and release of H_2 molecule. We then suggest that this might explain the higher photo-catalytic performance observed in CoaTPy with respect to the CoaPPy.

Reduction free energy representing the first step in the catalytic cycle is computed only for CoaTPy assuming linear solvent response. The reduction free energy is determined as -1.95 eV for CoaTPy. We observe slight differences in solvent reorganization energies calculated at reduced (1.30 eV) and oxidized limits (1.02 eV), therefore the present assumption, linear solvent response, is satisfied.

Concerning the reliability of our results, the explicit solvent model employed in our AIMD simulations already provides accurate information on the dynamic properties of the systems under consideration with respect to the widely applied static models such as solvent continuum model. In order to increase the accuracy in the reduction free

energy calculations, hybrid density functional scheme within DFT is applied rather than widely used GGA formalism. Besides, we have followed the protocols suggested in previous works [120] which reduces the error in the computational estimate to less than 0.2 eV.

We plan to extend this study by calculating reduction free energy also for CoaPPy for comparison. Besides, we intend to carry out reduction free energy calculations for the third step in the catalytic cycle, the second electron injection, which will provide additional information on the effects of ligand environment on H_2 production performance. An irreversible ligand switch in CoaTPy following the first electron injection have been observed by our experimental collaborators, which might substantially change the proposed H_2 production mechanism. Therefore, each catalytic cycle should be reconsidered and simulated for the catalyst that undergoes a ligand switch. Last but not least, we plan to model proton diffusion to the Co center using metadynamics which will help us understanding the effects of coordination sphere around Co on H_2 production performance.

5 Insight into H_2 Production Systems Using Oxides: Pyrphyrin and Co-Pyrphyrin Adsorbed on TiO_2(110) [68, 87, 130]

In this chapter, the structural and electronic properties of the complexes, Pyr and CoPyr monomers as well as their monolayer structures adsorbed on rutile(110) surface by means of DFT are discussed. It is generally accepted that anatase phase of TiO_2 exhibits higher photocatalytic activity than rutile TiO_2 [131], which resulted theoretical investigation of water–TiO_2 interactions mostly with the anatase phase [132]. However, in this study only the rutile phase is considered, which is easier to obtain as high quality single crystal [133] and, for this reason, it is employed in the experimental studies of the catalytic activity of supported-CoPyr/Pyr. We first briefly describe the applied methodology and the used models for the molecules, the surface and the complexes. Next, we discuss the possible adsorption configurations of CoPyr/rutile(110) and Pyr/rutile(110), and we analyze in detail the electronic structure of the most stable configurations. Monolayer structures are then created according to the experimental observations and energy level alignment of the complexes are compared with the experiments.

5.1 Computational Methodology

Electronic structure calculations are performed at the Kohn-Sham DFT level, employing the Gaussian and plane wave (GPW) formalism as implemented in the CP2K QUICKSTEP package [111]. Double-zeta valence plus polarization (DZVP) basis sets, optimized on molecular geometries (Mol-Opt method) [113], are employed for all atomic kinds. A cutoff of 600 Ry is used for the auxiliary plane wave basis set. The interaction between the valence electrons and the atomic cores is described through norm-conserving Goedecker–Teter–Hutter (GTH) pseudo potentials [112]. The va-

lence shells contain 12, 6, 17, 4, 1, and 5 electrons for Ti, O, Co, C, H, and N, respectively. Periodic boundary conditions are always applied.

As exchange–correlation functional, the general gradient approximation (GGA) by Perdew–Burke–Enzerhof (PBE) [80] is used. The dispersion interactions are corrected according to the Grimme–D3 scheme [96] for the optimization of the geometries. This level of theory has been proved to be sufficiently accurate to describe the structural properties of the materials involved in this study. Namely, the lattice parameters of bulk rutile turn out to be in agreement with the experimental values within an error of 1% [93]. However, PBE is known to underestimate the energy gap of TiO_2 as for other oxides [134, 135]. The most commonly adopted solution to this deficiency is the use of suitable hybrid functionals that can reproduce the experimental value [136, 137]. For the specific case of TiO_2, we find, in agreement with previous works, that the best accuracy in the energy gap is achieved by applying the Heyd–Scuseria–Ernzerhof (HSE06) hybrid functional [90,91,93]. All hybrid functional calculations are performed with the help of the auxiliary density matrix method (ADMM) [117–119], which provides a significant speed up and makes it possible to compute the electronic structure of several hundreds of atoms of condensed matter systems. The required ADMM basis sets have been optimized to reproduce the results of full hybrid functional calculations with very high accuracy. Despite the speed up obtained with ADMM, hybrid functional geometry optimization are still computationally very demanding and do not produce important changes with respect to the PBE optimization. Therefore, our strategy consists in carrying out the refinement of the electronic structure of PBE-optimized geometry using the HSE06 hybrid functional.

5.2 Structural Models

5.2.1 Rutile: Bulk and (110) Surface

The rutile lattice belongs to the $P4_2/mnm$ (No. 136) tetragonal space group [138, 139]. In the bulk, each Ti atom is coordinated by six O atoms, while the O atoms are three-fold coordinated by Ti. In order to assess our PBE computational set up, the lattice parameters are optimized for a 3×3×3 supercell (162 atoms). This supercell is sufficiently large to converge the bulk structural properties, which turn out to be in very good agreement with previously published data, from both experimental and DFT studies (see Table 5.1). The corresponding band gap energies, E_{gap}, computed

for the PBE and the HSE06 functionals are reported in Table 5.2 and also compared to previous studies. All GGA and LDA result underestimate the E_{gap} by more than 1.2 eV, while PBE0 overestimates it by about the same amount. Only the value obtained with HSE06 approximates the experiment with reasonable accuracy. The slight discrepancies between results obtained with the same functional can be ascribed to different basis sets and pseudopotentials.

Table 5.1: Lattice parameters (a and c) and bulk modulus (B) of bulk TiO_2. The values reported for this work are obtained for the 3×3×3 supercell and the PBE functional.

Method	a [Å]	c [Å]	B [GPa]	ref.
GGA/PBE/GPW	4.606	2.966	219	this work
GGA/PW92/PAW	4.649	2.972	225	[140]
GGA/PBEsol/PW	4.604	2.947	-	[41]
LDA/PAW	4.554	2.927	256	[141]
Experiment	4.587	2.954	210	[86]
Experiment	4.594	2.959	-	[138]

Table 5.2: Band gap energy (E_{gap}) of bulk TiO_2. The values reported for this work are obtained for the 3×3×3 supercell.

Method	E_{gap} [eV]	ref.
GGA/PBE	1.73	this work
GGA/PBE	1.74	[85]
GGA/PW92	1.80	[141]
LDA	1.81	[141]
HSE06	3.35	this work
HSE06	3.11	[93]
PBE0	4.21	[93]
Experiment	3.0	[86]

Figure 5.1 shows projected density of states (PDOS) for O and Ti atoms in bulk rutile. The highest occupied states have O-2p character, whereas the lowest unoccupied states are Ti-3d, in agreement with previously published calculations [142, 143]. The hybridization between O-2p and Ti-3d states results in covalent bonding [144].

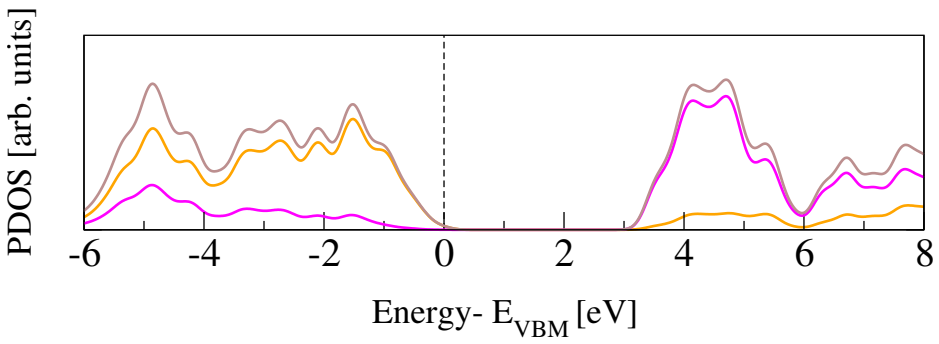

Figure 5.1: Density of states of bulk rutile: total DOS plotted with brown line, O PDOS in orange, Ti PDOS in magenta. The distributions are normalized by the number of atoms and the aligned at zero with the valence band maximum (VBM) energy.

The (110) surface is the most stable surface of rutile, and also the most frequently studied and used one for applications [145]. To model such a surface, a symmetric slab consisting of a few atomic layers is cut out from the bulk cleaving along the (110) plane. Above the surface, a sufficiently large amount of vacuum space (20 Å) is added to avoid interactions with the periodic images in the perpendicular direction. The surface unit cell contains two Ti atoms, which lay on the same plane, and four O atoms, two on the same plane as Ti, one above (sticking out O) and one below. One surface Ti atom is still six-fold coordinated, as in the bulk, while the second is five-fold coordinated. Among the O atoms, three are still three-fold coordinated, while the sticking out one is two-fold coordinated. This latter dangling O atom is a particularly active species, which can lead to the formation of vacancies at the surface, or be saturated. Figure 5.2 displays the top and side view of a 3×7 slab, containing five atomic layers. We label the surface three-fold and two-fold coordinated O atoms with O_{3c} and O_{2c}, while the bulk oxygens are labeled $O_{3c-bulk}$. We also distinguish between the bulk Ti atoms, labeled $Ti_{6c-bulk}$, and the under-coordinated Ti atoms at the surface, Ti_{5c}. In order to determine the optimal number of layers for the slab model, we tested the convergence of the surface energy. The surface energy is calculated as

$$E_{\text{surface}} = \frac{E_{\text{slab}} - N \cdot E_{\text{bulk}}}{2 \cdot A} \tag{5.1}$$

where E_{slab} is the total energy of the optimized slab model, E_{bulk} is the energy per TiO_2 unit in the bulk, N is the number of units contained in the slab, and A is the area of the exposed surface.

For calculations of the surface energy slabs from 3 to 9 layers have been considered. In Figure 5.3, the computed surface energies obtained with slab models of increasing

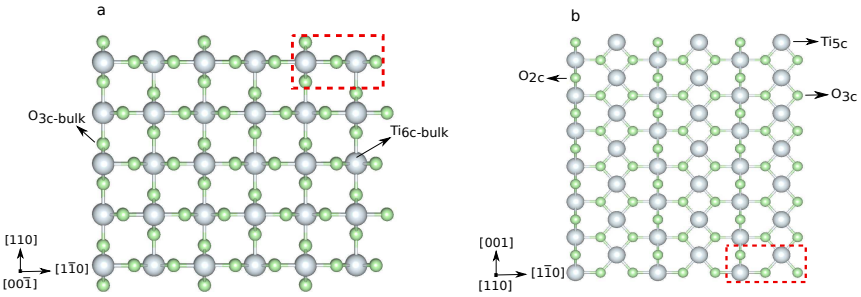

Figure 5.2: Ball and stick representation of the rutile (110) 3×7×5 slab, where 5 is the number of layers: a) side view and b) top view. For clarity, only topmost atomic layer is shown in (b). Surface atoms are labeled as O_{2c}, O_{3c}, and Ti_{5c}, bulk atoms as $O_{3c-bulk}$ and $Ti_{6c-bulk}$. The dashed red box indicates the surface unit cell. Color code: light gray: Ti, light green: O.

number of O-Ti-O layers are plotted. We compare the values obtained by keeping all the coordinates fixed in the bulk positions (black symbols in the figure) to those obtained by relaxing the outermost layers of the slab (green for 1 layer and red for two layers), and keeping fixed at bulk coordinates the innermost ones. For the rigid slab model, the surface energy is largely independent from thickness and amounts to 1.75 J/m^2. By relaxing the outermost or the two outermost layers on both sides of the slab, the surface energies are significantly reduced to around 1.21 and 0.69 J/m^2, respectively. We also computed the electronic properties for slabs of different size, with particular attention at the electronic states distribution at the surface, where it is most important for the interactions with the adsorbates. We compare 3×3 slabs of 5, 6, 7, and 8 layers, always fully relaxing the two outermost O–Ti–O layers on both sides and keeping fixed the innermost ones.

The HSE06 band gaps obtained from the optimized geometries are 3.18 eV for 5 layers, 3.29 eV for 6 layers, 3.13 eV for 7 layers, and 3.07 eV for 8 layers. The PDOS obtained from the first two relaxed layers for each of the tested models are reported in Figure 5.4. The band gap calculated by HSE06 for the rutile slab of five layers, 3.18 eV, in agreement with the experiment [146]. The reduction of the energy gap at the surface is due to the presence of energy states in the gap, which are generated by electrostatic shifting of Ti_{5c} states towards O_{2c} and $O_{3c-bulk}$ band, also discussed in Ref. [147]. We observe that with the 5-layers model, and by keeping the atoms of the middle layer of the slab fixed in the bulk positions, the two exposed surfaces are decoupled and their electronic structure does not depend significantly on the thickness.

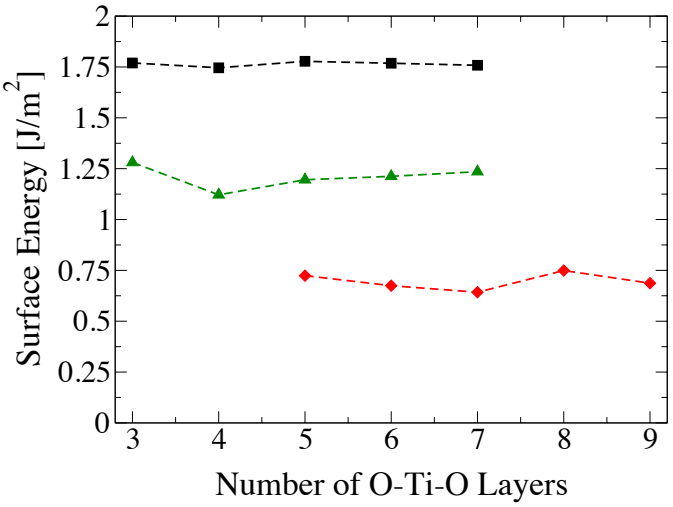

Figure 5.3: Surface energy of rutile (110) plotted vs the number of O-Ti-O layers of the slab model.Values obtained for rigid slab are in black (bulk coordinates), values obtained relaxing the outermost layer on both sides are in green, and relaxing two O-Ti-O layers on both sides are in red.

Therefore, among the different sizes of slabs five layers is a good compromise between accuracy and efficiency.

For the simulation of the adsorption, we used a 5-layers slab where only the two O–Ti–O layers on the adsorption site have been relaxed, while the rest of the slab has been kept fixed in the bulk position. This set up does not affect the electronic structure at the surface and the adsorption, as demonstrated from the discussion above. Hence, we conclude that a 5 layer slab is sufficient to model the rutile (110) surface. The surface energy of the 3×3×5 slab is 0.72 J/m^2, in quite good agreement with the values found in the literature [145].

5.2.2 Pyrphyrin and Co-Pyrphyrin

Ball and stick sketches of Pyr and CoPyr are shown in Figure 5.5. Pyr is characterized by CN groups binding to the pyridine rings via sp^2 hybridized bridging carbons. We label the nitrogen atoms of the cyano groups N_{CN} to distinguish them from the pyridine nitrogens at the center of the molecule (N_p). Two N_p are protonated in Pyr at anti positions, while the protons are replaced by the Co(II) cation in CoPyr. Structure optimization of the second isomer of metal-free pyrphyrin where the protons are

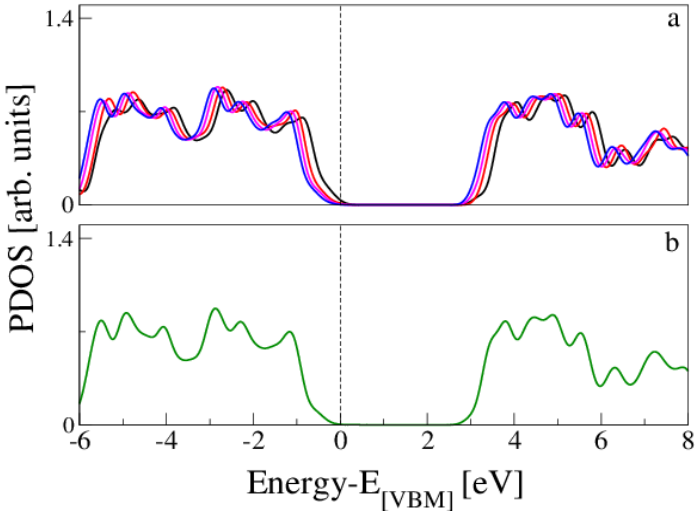

Figure 5.4: PDOS on top two O-Ti-O layers of rutile slabs. a) PDOS of symmetrically relaxed slabs. Black solid line represents PDOS of 5 layer, red 6 layer, magenta 7 layer, and blue 8 layer. Alignment is done with respect to valence band maximum of each slab. b) PDOS of 5 layer slab where only the top two O-Ti-O layers have been relaxed, the one that is used in our calculations. PDOS is aligned with respect to first occupied peak of symmetrically relaxed 8 layer slab.

attached to the adjacent pyridine nitrogens of the same side the molecule is by 0.23 eV less stable. Therefore, in this work protons in Pyr will be considered at anti positions. In the gas phase, both molecules are planar with a vanishing dipole, as discussed in Ref. [58]. In the center of the molecule, the four N_p are symmetrically coordinating Co

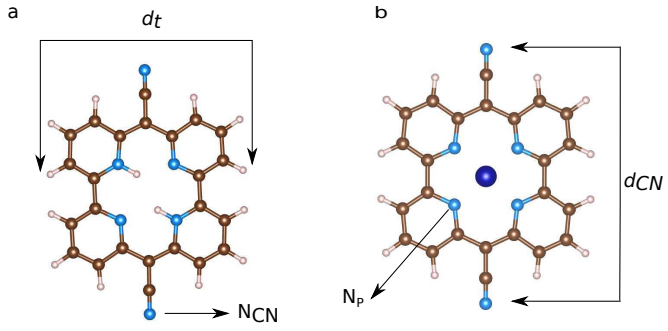

Figure 5.5: Ball and stick representations of a) Pyr and b) CoPyr. The molecular size is described by means of the two diameters, d_{CN} and d_t. Nitrogens in cyano groups and pyridine rings are labeled as N_{CN} and N_p, respectively. Color code: brown: C, light pink: H, dark blue: Co, blue: N.

in CoPyr, while the protonated nitrogens in Pyr are displaced outwards. Along the axis of the cyano groups, d_{CN}, the molecule is slightly shorter for CoPyr with respect

to Pyr, due to the interaction between Co(II) and the electronegative nitrogens. Some structural parameters are reported in Table 5.3.

Table 5.3: Selected distances calculated for the optimized geometries of Pyr and CoPyr in the gas phase.

Molecule	Distances	Length [Å]
Pyr	d_{CN}	11.96
	N_p–N_p (prot.)	3.98
	N_p–N_p (not prot.)	3.80
	d_t	9.45
CoPyr	d_{CN}	11.78
	N_p–N_p	3.77
	d_t	9.57

A theoretical work by Han et al. [148] who calculated the ground state electronic structures and some excitation properties of Zn centered porphyrins, namely YD2 and YD2-o-C8, with different density functionals, shows that HSE06 provides the best description of these properties. Therefore, HSE06 density functional is also considered in this work for the electronic structure calculations of Pyr and CoPyr in gas phase. Calculations with CoPyr are always performed with spin polarization. The lowest energy spin state turns out to be a doublet and the spin density is localized exclusively at the Co center. As it can be seen from Figure 5.6, the homo of CoPyr in the gas phase has major contributions from the cyano groups, the pyridine carbons, and the N_p, but it is also present at Co(II) centers. The lumo, instead, is uniformly distributed over the pyridine CH groups, the central C atoms, and the N_p, but it does not have significant contributions from the cyano groups and the Co(II). Figure 5.7, instead, shows the homo and the lowest unoccupied molecular orbital lumo of the Pyr in the gas phase. The molecular orbitals are distributed over all pyridine rings.

5.2.3 Adsorption of Molecules on Rutile(110)

In order to find possible adsorption sites of the molecules on rutile, it is necessary to explore the potential energy surface of the CoPyr@rutile and Pyr@rutile complexes. We started eleven independent optimizations, changing the initial coordinates of the gas-phase optimized CoPyr on rutile. The molecule has always been positioned par-

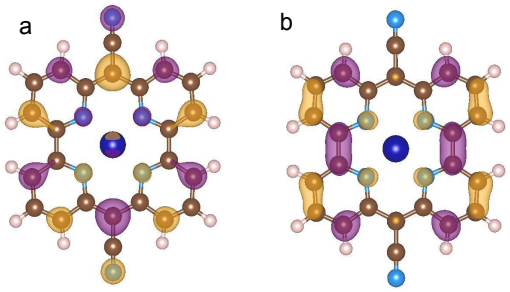

Figure 5.6: Homo (a) and lumo (b) of CoPyr in the gas phase. The displayed isosurfaces are obtained at the value of ± 0.236 e/Å^3.

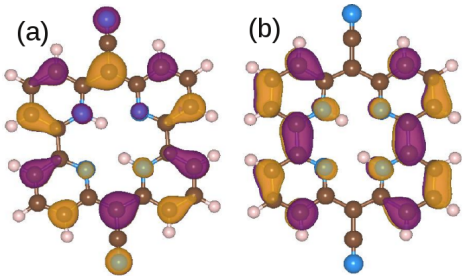

Figure 5.7: Selected molecular orbitals of optimized Pyr in the gas phase, (a) homo and (b) lumo. Color code: brown: C, blue: N, and light pink: H. Isosurface (orange for positive and purple for negative) is set to ± 0.03 e/Å^3.

allel to the surface at a distance a few Å apart from the topmost atoms moving it rigidly by changing the position of Co(II) and the two N_{CN} with respect to the surface O_{2c} and Ti_{5c} atoms and rotating the molecular axis parallel to the surface, as shown in Figure 5.8.

The optimization is carried out by relaxing the molecular geometry and the two top-most layers of the rutile slab. The other three slab layers are kept fixed at bulk coordinates. According to the results, CoPyr finds many local minima on potential energy surface that trap the molecule, even if the adsorption energy is low. In the case of model-f, even starting from a slightly different configuration, the structure is minimized to model-a (see Figure 5.8). Hence, starting the geometry optimization with a small perturbation results in the same favorable configuration. This stable configuration is only obtained when two N_{CN} atoms are close to Ti_{5c}. Instead, when only one N_{CN} interacts with surface Ti_{5c}, as in the case of model-e and model-i, the adsorption energy is weaker. In model-k, Co(II) shows attractive interaction with O_{2c}, however the interaction is repulsive for N_{CN}, which are pushed away from the surface. The initial geometries of models g and j are slightly different from each other but are

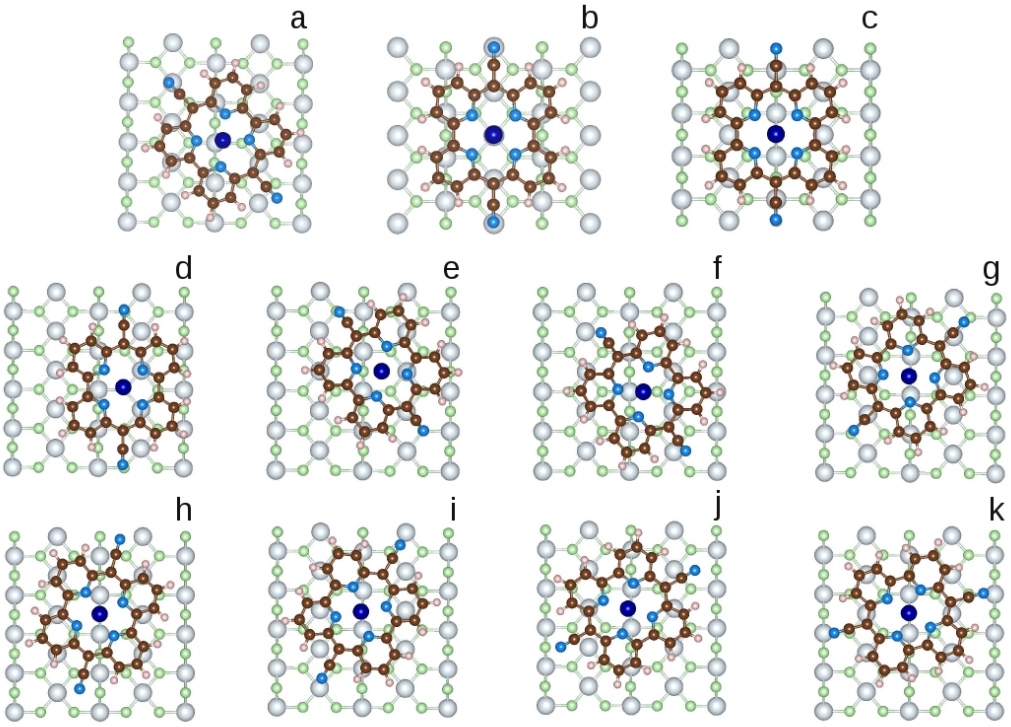

Figure 5.8: Initial configurations of CoPyr@rutile complex. Color code: brown: C, light blue: N, light pink: H, dark blue: Co, light green: O, grey: Ti.

minimized to the same final model-j, which is similar to model-g, where N_{CN} adsorbed between O_{3c} and Ti_{5c} atoms, and Co(II) adsorbed on top of O_{2c}. In model-h, we may expect rotation of N_{CN} towards Ti_{5c}, however the hydrogen atoms coordinated with O_{2c} prevent it.

Geometry optimization results suggest that from these eleven starting positions, only four distinct configurations show relatively high stability. These four structures are displayed in Figure 5.9 with their names model-a, b, c, and d. The adsorption energy (E_{ads}) is calculated as

$$E_{\text{ads}} = [E_{\text{complex}} - (E_{\text{slab}} + n_{mol}E_{\text{monomer}})]/n_{mol} \tag{5.2}$$

where E_{complex} is the total energy of the complex, E_{slab} is the energy of the slab where only two layers are fully optimized, and E_{monomer} is the energy of the molecule optimized in vacuum. For the monomer calculations n_{mol} is 1, whereas it is equal to 2 for the monolayer case. Negative values of E_{ads} correspond to exothermic adsorption. For each optimized structure, the amount in dispersion energy is extracted, so that

its contribution to the adsorption energy is calculated as

$$E_{\text{ads}}^{\text{disp}} = [E_{\text{complex}}^{\text{disp}} - \left(E_{\text{slab}}^{\text{disp}} + n_{mol} E_{\text{monomer}}^{\text{disp}}\right)]/n_{mol} \tag{5.3}$$

The dispersion contribution is always attractive. The distortion energy of the molecules (E_{dist}) is, instead, the increase in molecular energy due to the geometrical changes induced by the interaction with the surface,

$$E_{\text{dist}} = E_{\text{monomerd}} - E_{\text{monomer}} \tag{5.4}$$

E_{monomerd} is the energy of the molecule calculated in vacuum, but with the same coordinates obtained from the complex optimization. For the monolayer adsorption on TiO_2(110) surface the stability of the complexes, both Pyr/TiO_2 and CoPyr/TiO_2, are evaluated in terms of three parameters, the molecules/oxide interactions ($E_{\text{int}}^{\text{monolayer}}$), the distortion energy of the monolayer ($E_{\text{dist}}^{\text{monolayer}}$), and the intermolecular interactions ($E_{\text{mol}}^{\text{inter}}$) which are calculated as

$$E_{\text{int}}^{\text{monolayer}} = [E_{\text{complex}} - (E_{\text{monolayerd}} + E_{\text{slabd}})]/n_{\text{mol}} \tag{5.5}$$

and

$$E_{\text{dist}}^{\text{monolayer}} = [E_{\text{monolayerd}} - E_{\text{monolayer}}]/n_{\text{mol}} \tag{5.6}$$

and

$$E_{\text{mol}}^{\text{inter}} = [E_{\text{monolayer}} - n_{\text{mol}} E_{\text{monomer}}]/n_{\text{mol}} \tag{5.7}$$

respectively. E_{slabd} is the energy of the bare slab at the coordinates of the complex, $E_{\text{monolayer}}$ is the energy of the monolayer computed as free standing, and $E_{\text{monolayerd}}$ is the energy calculated in vacuum with the same coordinates of the monolayer in the complex.

5.3 Results and Discussion

5.3.1 CoPyr and Pyr Monomers on Rutile(110)

In this section, the geometry optimization results and electronic structure analysis will be discussed detaily for CoPyr monomer on rutile, while we will only briefly mention about the corresponding results of Pyr@rutile. The resulting four adsorption configurations of CoPyr@rutile are characterized by different energies and structural parameters. In Table 5.4, the above defined E_{ads}, $E_{\text{ads}}^{\text{disp}}$, E_{dist} values are reported

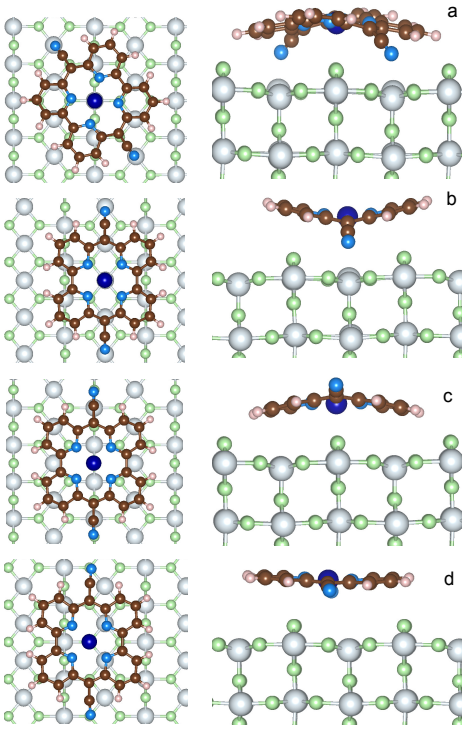

Figure 5.9: Four different optimized structures of the CoPyr@rutile complex, as obtained from different initial positions of the molecule. The top view (left) and one side view (right) of each of the four models are shown. Color code: see previous figures.

together with the average height of the molecule on the Ti_{5c} layer (h_{av}), the difference in height between the lowest and the highest atoms in the molecule (Δh), which is a measure of the deviation from planarity, the distance between the two N_{CN} atoms (d_{CN}), and the minimum distance between an atom of the molecule and an atom of the surface (d_{min}).

Table 5.4: Energies and structural parameters characterizing the four distinct adsorption sites for CoPyr@rutile reported in Figure 5.9.

Model	E_{ads} [eV]	E_{ads}^{disp} [eV]	E_{dist} [eV]	h_{av} [Å]	Δh [Å]	d_{CN} [Å]	d_{min} [Å]	pair
a	-4.18	-2.62	0.57	3.67	2.16	10.86	2.13	N_{CN}–Ti_{5c}
b	-3.56	-2.34	0.40	3.89	2.34	11.14	2.22	N_{CN}–Ti_{5c}
c	-3.35	-2.89	0.24	3.52	1.66	11.51	2.25	Co(II)–O_{2c}
d	-2.49	-2.42	0.09	3.94	0.95	11.65	2.77	H–O_{2c}

As a general observation, the interaction to the surface is relatively weak and the major contribution is due to the dispersion term, which varies from 60% to almost

100% of the adsorption energy. The strongest adsorption is obtained for model-a, where the molecule is bent along the d_{CN} axes such that both the N_{CN} atoms can sit exactly on top of Ti_{5c} centers, while Co(II) coordinates two O_{2c}. The interaction is further favored by the upwards displacement of the involved Ti atoms by 0.26 Å, thus reducing the N–Ti distance to only 2.13 Å. CoPyr is bent along both axis, even if the curvature is more pronounced along d_{CN}, reducing the d_{CN} distance by about 1 Å with respect to the gas phase structure. The geometrical changes correspond to a distortion energy of 0.57 eV. Subtracting from the total adsorption energy the distortion energy, we obtain an interaction energy of -4.75 eV, of which -2.62 eV are attributed to dispersion. The remaining -2.13 eV are mainly due to the chemical bonding between N_{CN} and Ti (≈-1 eV per N_{CN}), which, as it will be discussed in the following, is responsible for the rehybridization of the molecular homo with the surface states.

In model-b, both N_{CN} and Co(II) are sitting on top of Ti_{5c} centers, and the d_{CN} axis is oriented along the [001] lattice direction, i.e. rotated by about 30 degrees with respect to model-a. Also in this case, the closest contact between molecule and surface is the N–Ti interaction, and the involved Ti atoms are displaced upwards by 0.15 Å. However, in this position, some O_{2c} atoms happen to be in proximity of the pyridine rings, which consequently bend outwards. Overall, the distance between molecule and surface (h_{av} = 3.89 Å) is larger than in model-a, and, even though the molecular distortion energy is smaller, the adsorption interaction is weaker. This can be explained in terms of the repulsive electrostatic interaction between Co(II) and Ti and the reduced dispersion contribution due to the larger average distance.

Like in model-a, in model-c Co coordinates the two closest dangling O. The N_{CN} are on top of the surface oxygen giving rise to a repulsive interaction, which causes the upwards bending along the d_{CN} axis. Since only the cyano groups are displaced, the molecule is less distorted than in the two previous configurations, as also indicated by its d_{CN} length and the computed distortion energy. In average, CoPyr is closer to the surface and, as a consequence, the dispersion energy term is larger. By subtracting the distortion energy and the dispersion energy from the total adsorption energy, the remaining interaction energy amounts to 0.70 eV.

Finally, in model-d, the most active molecular centers, Co(II) and N_{CN}, are too far from the under-coordinated atoms at the surface. The molecular structure is only slightly modified upon adsorption, since the only attractive interaction is attributed to the dispersion forces. This is a classical example of physisorption, as also confirmed

by the almost equal values of E_{ads} and $E_{\text{ads}}^{\text{disp}}$. Rather weak physisorption has been already reported for the case of a single pyridine ring adsorbed on TiO_2 [149].

The standing adsorption of CoPyr on rutile(110) surface has also been examined. CoPyr is positioned perpendicular to the (110) surface, with one N_{CN} on top of one Ti_{5c}, since between these two species the binding is expected to be strongest. After the optimization of the structure, the distance between N_{CN} and Ti_{5c} is 2.09 Å. The resulting adsorption energy E_{ads} is -1.61 eV, i.e. 2.5 eV lower than for the molecule adsorbed flat. The obvious reasons for the weaker binding are that only one direct N-Ti_{5c} interaction is available and the significantly smaller contribution of dispersion (-0.65 eV), given the standing geometry.

Pratik et al. [150] modeled several different porphyrin-derived molecules adsorbed both horizontally and vertically on anatase nanoparticles. Their calculations show that while horizontal orientation of porphyrin on anatase has E_{ads} of -2.6 eV, porphyrin–4–NO_2 has -9.30 eV, and porphyrin–4–NH_2 has -4.33 eV, vertical attachment of 1–NMe_2–porphyrin–1–COOH results in E_{ads} of -2.80 eV.

In summary, the most effective interactions for the adsorption of CoPyr on rutile are those between N_{CN} and the Ti_{5c} surface atoms, followed by the Co(II)–O_{2c} coordination. These are maximized in model-a, which turns out to be the most stable adsorption site. Therefore, the following analysis of the electronic properties of the CoPyr@rutile is based on this model.

In the case of Pyr/TiO_2(110), the resulting optimized complex is depicted in Figure 5.10. E_{ads} is calculated as -4.22 eV, indicating relatively strong interactions between Pyr and TiO_2. Apart from chemical interactions, van–der–Waals interactions contribute significantly by $E_{\text{ads}}^{\text{disp}}$ =-2.57 eV. The distance between cyano-N and five-coordinated surface Ti atom becomes 2.14 Å. As in the case of CoPyr/TiO_2(110), the convex shape of the molecule on the oxide surface due to this bonding of cyano-N with the surface Ti atoms results in a cyano-N–cyano-N distance of 10.98 Å compared to 11.96 Å in the gas phase.

Apart from this structure, an alternative configuration is possible where the two protons attached to the pyridinic nitrogens are closer to the two-coordinated surface oxygens [151]. The optimized structure of this alternative configuration is shown in Figure 5.11. The adsorption energies of the two configurations are almost the same, the difference is only around 0.09 eV. We do not observe bending of the protons attached to the pyridinic nitrogen atoms towards the surface oxygen atoms. The

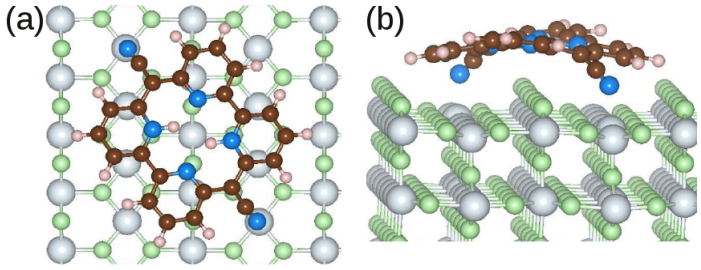

Figure 5.10: Top view (a) and side view (b) of the optimized structure of Pyr on $TiO_2(110)$. For clarity only the surface layer and two rutile layers are shown in a and b, respectively. Color code: blue: N, brown:C, pink: H, green: O, and gray: Ti.

proton-pyridinic nitrogen bond lengths are almost the same in the two configurations, around 1.04 Å.

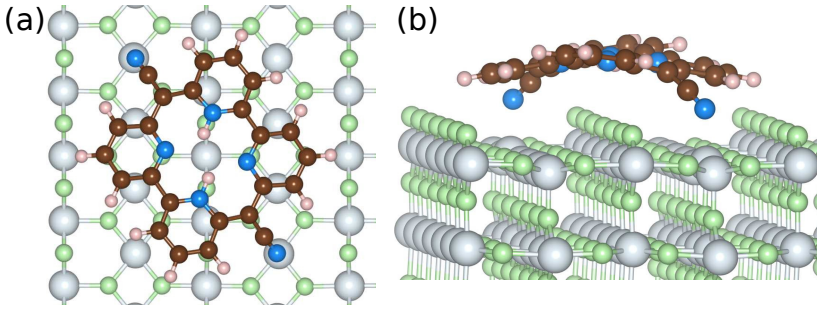

Figure 5.11: Alternative configuration of $Pyr/TiO_2(110)$ where the protons attached to the pyridinic nitrogen are positioned on top of the two-coordinated surface oxygen atoms. Top view and side view are shown in (a) and (b), respectively. Color code: see previous figures.

Concerning metalation of the adsorbed Pyr molecules XPS measurements show that Pyr/TiO_2 is readily metalated at room temperature. The observed fast metalation might be attributed to the stronger molecule–substrate interaction and the particular adsorption geometry of Pyr on $TiO_2(110)$. For example, the bent convex shape of Pyr/TiO_2 may facilitate the Co uptake.

The redistribution of the electronic charge induced by the adsorption is shown in the electron density difference maps. The electron density difference is calculated by subtracting from the total density of the complex $\rho_{\text{complex}}(\mathbf{r})$ the individual electron densities of CoPyr and the slab, at the same coordinates as in the complex

$$\Delta\rho(\mathbf{r}) = \rho_{\text{complex}}(\mathbf{r}) - (\rho_{\text{slab}}(\mathbf{r}) + \rho_{\text{mol}}(\mathbf{r})). \tag{5.8}$$

The two isosurfaces of $\Delta\rho(\mathbf{r})$ for CoPyr@rutile(110) depicted in Figure 5.12 correspond to +0.317 e/Å^3, i.e., charge accumulation (top left panel), and -0.317 e/Å^3 (top right

panel), i.e., charge depletion. We notice that the electrons on the pyridine rings are partially pushed away from the surface, to reduce the overlap with dangling orbitals of the O_{2c} atoms. On the other hand, electron accumulation is observed between N_{CN} and the closest under-coordinated Ti_{5c} atoms, which confirms the presence of a chemical interaction between these species. The rearrangement leads to the polarization of the molecule along the perpendicular axis z. In panel c of Figure 5.12 the 2D-integrated density difference calculated as

$$\Delta\rho_{xy}(z) = \int dx \int dy \Delta\rho(\mathbf{r}) \tag{5.9}$$

is plotted along z. We observe that a finite dipole moment arises along the z axis, which, estimated as $\mu_z = \int \rho_{xy}(z) \cdot z dz$, amounts to 0.5 D.

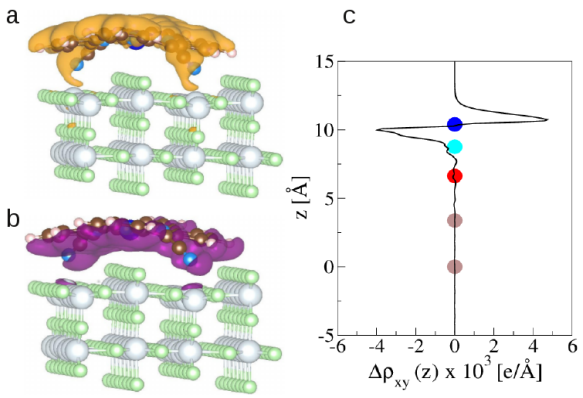

Figure 5.12: Electron density difference $\Delta\rho(\mathbf{r})$: isosurfaces taken at 0.317 e/Å^3 (a) and -0.317 e/Å^3 (b). c) 2D integrated density difference $\Delta\rho_{xy}(z)$ plotted along the slab's perpendicular axis. Red sphere indicates the height of the under-coordinated Ti_{5c} atoms, the cyan is N_{CN}, the dark blue Co(II), and the brown spheres are located at the height of two deeper layers.

Figure 5.13 shows the two isosurfaces of $\Delta\rho(\mathbf{r})$ corresponding to $+0.002$ e/Å^3, i.e., charge accumulation (left panel), and -0.002 e/Å^3 , i.e., charge depletion (right panel) for Pyr@rutile(110). In particular, electron accumulation is observed between cyano-N and the closest under-coordinated Ti atoms. This picture also confirms the presence of chemical interactions between cyano-N and five-coordinated Ti species for Pyr@rutile(110) complex.

A Bader charge analysis [152] is carried out for the optimized configurations of Pyr/TiO_2 and $CoPyr/TiO_2$ to shed light on the charge transfer between the molecules and the substrate. Our results show that there is a charge flow from the molecules to the TiO_2 surface which is very similar for Pyr (0.481e) and CoPyr (0.488e).

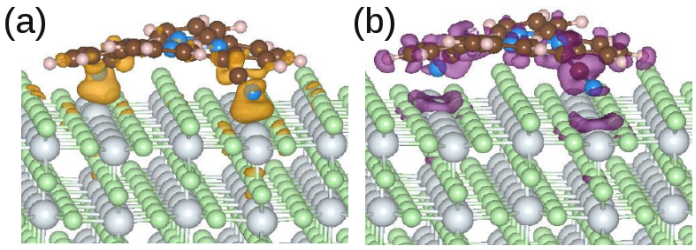

Figure 5.13: Electron density difference $\Delta\rho(\mathbf{r})$: Isosurfaces correspond to 0.002 e/Å^3 (a) and -0.002 e/Å^3 (b).

The total and projected densities of states, TDOS and PDOS, provide further information on the redistribution of the molecular orbitals upon adsorption and on the nature of the interaction. Spin polarization has been used for all calculations; however, not negligible spin density difference is observed only on Co(II), as shown in Figure 5.14. Therefore, we plot the distinct alpha and beta spin DOS solely for Co(II).

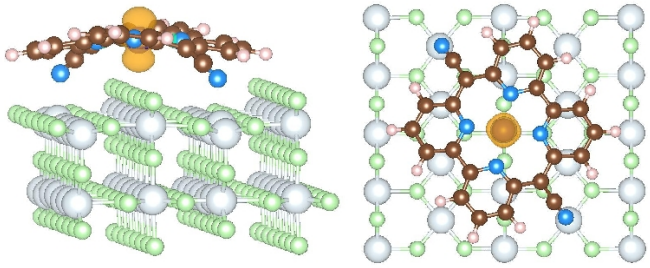

Figure 5.14: Spin density of CoPyr@rutile from side view (left panel) and top view (right panel). Isosurface is taken at 0.317 e/Å^3 and spin density is located on Co(II).

We compare the density of states calculated for the CoPyr@rutile complex with those calculated for the optimized molecule in the gas phase and for the pristine rutile surface. All PDOS plots related to the complex are aligned with respect to the corresponding VBM and normalized by the number of atoms considered in the projection. In order to facilitate the comparison, the PDOS of the clean rutile (110) slab are rigidly shifted to aligning the bulk states, i.e., the projections on the atoms of the inner layers (third and fourth) to the same states of the CoPyr@rutile. These states are not affected by the adsorption and therefore are easily recognizable.

In Figure 5.15, the TDOS of CoPyr@rutile (top panel) is compared to the contribution obtained from its projection on the CoPyr molecule only (bottom panel). The different normalization factor makes the low intensity features of the molecular

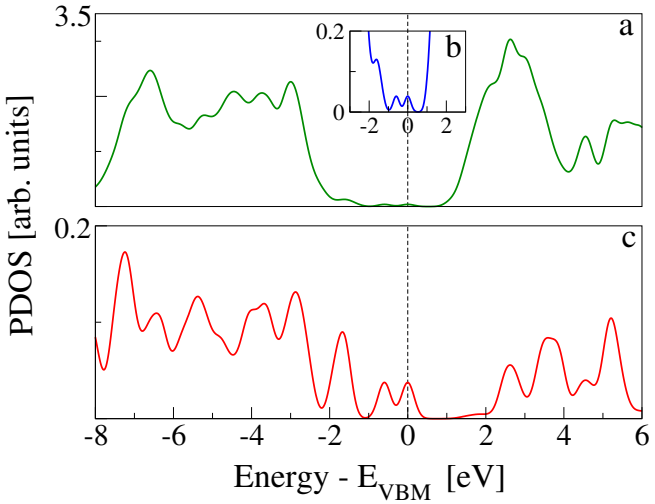

Figure 5.15: a) TDOS of CoPyr@rutile(110). The inset (b) shows a zoom-in of the energy gap region, which allows to distinguish the molecular states within the rutile energy gap. c) DOS projected on all the atoms of CoPyr. Since the number of atoms is much smaller, the normalization factor is different, which allows to better appreciate the fine structure of the molecular states.

states appear with more evidence in the bottom panel. The homo of the complex is clearly a molecular state of CoPyr. The lumo, on the other hand, is mainly located on the rutile slab. The calculated energy gap turns out to be 1.06 eV, which is 1.22 eV smaller than the gap of rutile (110). The lowest unoccupied states with major contributions on CoPyr are about 2.5 eV above the VBM.

The effects of CoPyr adsorption on the DOS of the slab are evaluated by projecting only on the slab's atoms and comparing to the PDOS computed for the pristine slab. In Figure 5.16, we distinguish between contributions from surface titanium atoms (b), and surface oxygen atoms (c). The signature of the surface Ti_{5c} atoms is the growth in intensity of the left shoulder of the lowest band of unoccupied states, as compared to PDOS of bulk Ti atoms (see Figure 5.1). The center of this band is at about 1.5 eV. Of the 21 Ti_{5c} atoms at the surface in our model slab, only two strongly interact with the molecule via the N_{CN} linkers and are responsible for the small difference between the red (CoPyr@rutile) and the blue (clean) curves in panel b. The band of the highest occupied states in rutile is mainly constituted of O-2p orbitals. The differences between bulk (see Figure 5.1) and surface are more evident in this case since the surface oxygen PDOS presents one relatively narrow band at about -3 eV

and lower intensity features at lower energies. This pronounced feature is formed by the highest occupied surface states. The effects of CoPyr adsorption in the O_{2c} PDOS are ascribed to the two surface oxygens interacting with Co(II).

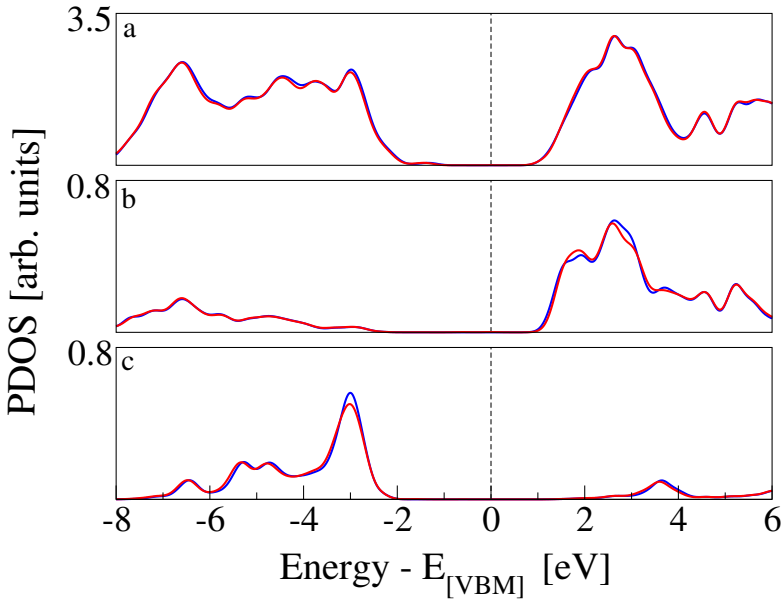

Figure 5.16: PDOS related to surface Ti and O atoms of CoPyr@rutile(110) (red) and of the clean rutile (110) (blue) are compared. While energy states of CoPyr@rutile are aligned with respect to its VBM, alignment in pristine rutile is carried out with respect to highest occupied band of surface O atoms of CoPyr@rutile. a) TDOS. b) PDOS on surface under-coordinated Ti centers. c) PDOS on under-coordinated O centers at the surface.

The electronic structure rearrangements occurring upon adsorption have their major effects on the CoPyr molecular orbitals. The PDOS on CoPyr adsorbed and in the gas phase are compared in Figure 5.17. All the plots are aligned with the homo at zero eV. The PDOS of CoPyr@rutile (red curves) shows a general broadening of the bands. The occupied states on Co(a), N_p (b), and C (d) present the same main features as in the gas phase. The lowest unoccupied states are shifted to higher energies by about 0.5 eV. The projected energy gap becomes 0.48 eV larger than the homo-lumo gap in the gas phase, if one considers the lowest unoccupied state with major contributions on the adsorbed molecule, which actually is at 2.5 eV above the homo. The sharp bands characterizing the PDOS on the N_{CN} in the gas phase are most strongly affected by the interaction with the surface. The two localized molecular states at -3.7 eV and -5.5 eV are replaced by a broad distribution due to

the re-hybridization with the Ti states. Moreover, the interaction has a clear effect on the charge distribution corresponding to the homo of CoPyr. As shown in Figure 5.18, the orbital extends in the region between molecule and surface, thus strengthening the chemical bonding. This electronic rearrangement explains the bending along d_{CN} and the upwards displacement of the Ti atoms.

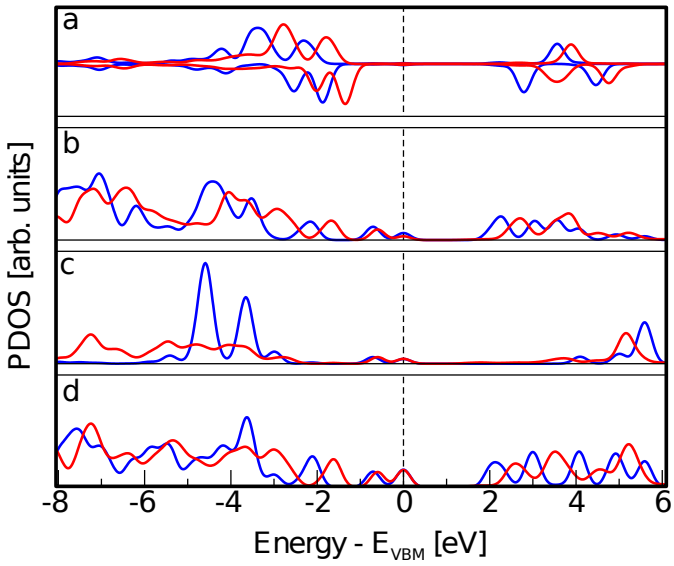

Figure 5.17: PDOS on different species of CoPyr adsorbed on rutile (red solid line) and optimized in the gas phase (blue solid line). a) PDOS on Co. Positive values are for the alpha spin channel and negative values for the beta spin channel. b) PDOS on the central N atoms binding to the pyridine rings, N_p. c) PDOS on the external N atoms belonging to the cyano groups, N_{CN}. d) PDOS on all carbon atoms.

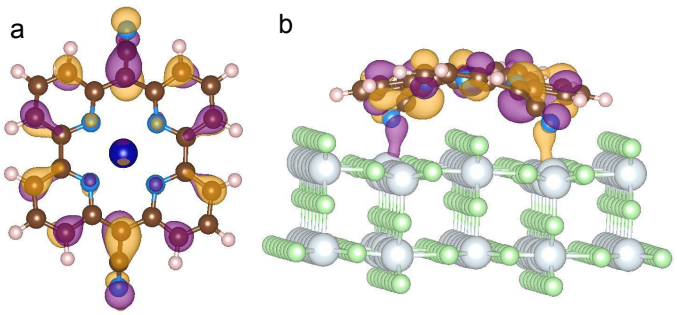

Figure 5.18: Representation of the homo of CoPyr adsorbed on rutile (110). Top (a) and side (b) view. The displayed isosurfaces are obtained at ± 0.236 e/Å^3.

Finally, we separate the contributions to the DOS ascribed to the two Ti_{5c} and the two O_{2c} atoms more directly involved in the interaction. The resulting PDOS are

plotted in Figure 5.19 and compared with the PDOS obtained from all the Ti_{5c} and O_{2c} present at the slab surface. While no significant difference is observed among the occupied states, a clear effect of the interaction is present for the lowest unoccupied states localized at Ti_{5c}. In particular, we observe the increase in intensity of the first peak and the consequent depletion at higher energies. This result implies the presence of available empty states on the Ti atoms that are also involved in the extension of the molecular homo state. On the other hand, the occupied states localized on the surface O atoms are more than 2 eV lower in energy than the CoPyr homo and are not significantly perturbed by the adsorbate.

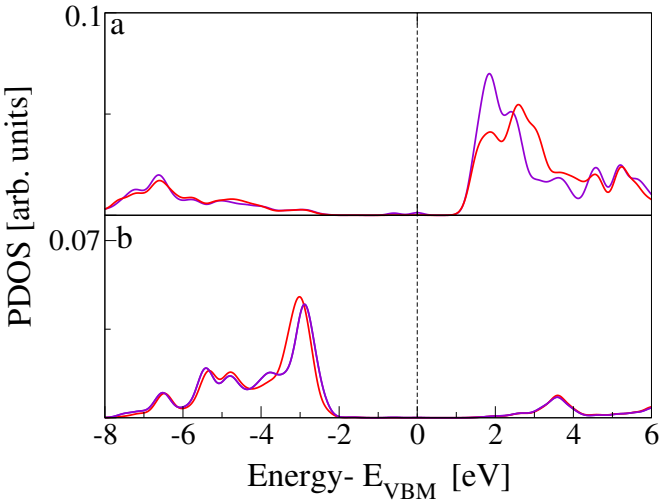

Figure 5.19: a) PDOS on Ti_{5c} atoms. The red line is the same PDOS shown in panel b of Figure 5.16, related to the complex. The purple line is related to the only two surface Ti atoms interacting directly with N_{CN}. b) PDOS on O_{2c} atoms. Red line is the same PDOS presented in panel c of Figure 5.16. The purple line is obtained by the projection on the two oxygen atoms coordinating the Co(II) in CoPyr@rutile(110).

In the case of Pyr/TiO_2(110) complex, similar to the CoPyr/TiO_2(110) case homo and homo-1 is located on the Pyr molecule, whereas lumo is distributed over Ti atoms of TiO_2(110) surface. The molecular band gap is calculated as 2.62 eV, whereas band gap of the slab is computed as 3.48 eV which is not affected by the molecular adsorption. The overall band gap of the system, energy difference of the lumo state of the slab and homo state of the molecule, is determined as 1.61 eV. Figure 5.20 shows the homo of the Pyr/TiO_2(110) complex. As a general observation, similar to

the CoPyr/TiO_2(110) case the homo, molecular state of Pyr, extends in the region between molecule and the surface.

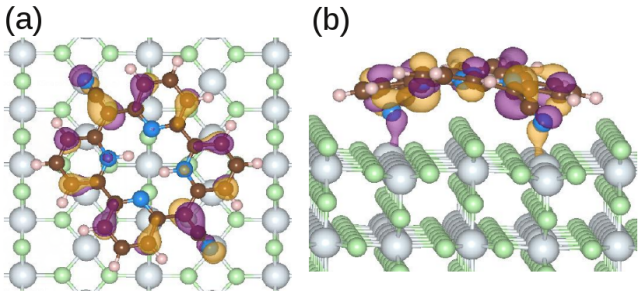

Figure 5.20: Representation of the homo of Pyr adsorbed on TiO_2(110). Top (a) and side (b) view. The displayed isosurfaces (orange for positive and purple for negative) are obtained at ± 0.036 e/Å^3.

5.3.2 CoPyr and Pyr Monolayers on Rutile(110)

The monolayer calculations of both CoPyr@rutile and Pyr@rutile complexes are carried out using a 2×8×5 TiO_2 slab. In both cases, the two topmost layers of the slab are relaxed, whereas the rest is kept fixed in the bulk positions. LEED patterns of Pyr/TiO_2(110) show a single phase over a wide coverage range and suggest the formation of ordered domains with a distorted $c(2 \times 8)$ superstructure in the sub-monolayer regime. The superstructure persists even after metalation with Co which suggests a strong anchoring of the Pyr molecules in this particular adsorption geometry. As a general observation, the experimental findings are corroborated by monolayer calculations of Pyr and CoPyr on TiO_2(110) and reveal that the adsorption structures of monomers and monolayers of both molecules are very similar and thus relatively independent on coverage and metalation.

Figure 5.21 shows the optimized $c(2 \times 8)$ superstructure of a CoPyr monolayer on the TiO_2 (110) surface. Again, the CoPyr molecules preserve their bended shape also in the monolayer case. E_{ads} and $E_{\text{ads}}^{\text{disp}}$ contribution are computed as -3.73 and -2.83 eV, respectively. Concerning the results of isolated monomer [87], monolayer calculations give slightly lower and larger E_{ads} and E_{disp}, respectively. The distance between the two cyano-N atoms of the CoPyr molecule is 10.87 Å which is very similar to the monomer adsorption case. The distance between cyano-N and the undercoordinated Ti becomes 2.2 Å which is slightly larger than for CoPyr monomer adsorption (2.13 Å). The molecules/oxide interactions, $E_{\text{int}}^{\text{monolayer}}$, is computed as -5.35 eV for this

configuration. The shortest distance between two cyano-N atoms of two adjacent CoPyr molecules becomes 3.2 Å. The computed $E_{\text{dist}}^{\text{monolayer}}$ and $E_{\text{mol}}^{\text{inter}}$ are 1.15 and -0.48 eV, respectively.

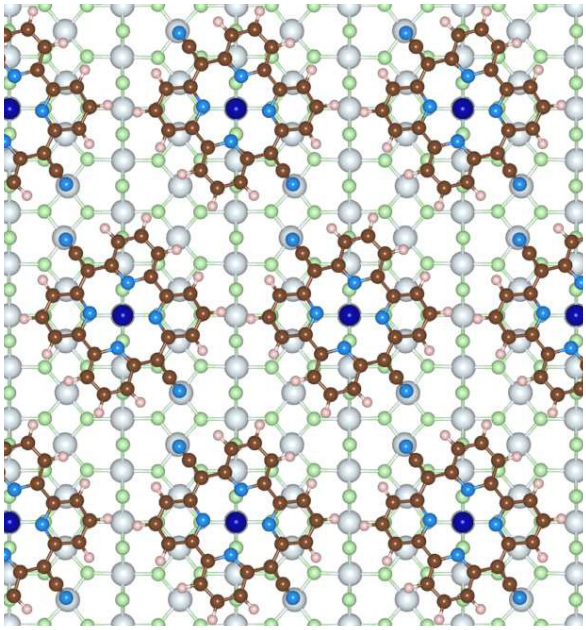

Figure 5.21: Optimized $c(2 \times 8)$ CoPyr monolayer configuration on TiO_2 (110). For clarity only the surface layer of TiO_2(110) is depicted. Color code: see the previous figures.

Figure 5.22 shows the optimized $c(2 \times 8)$ superstructure of a Pyr monolayer on the TiO_2(110) surface. Geometry optimization results show that the molecules preserve their convex shape towards the surface as suggested by the monomer calculations. E_{ads} is calculated as -3.76 eV which is slightly lower than the monomer case. Instead, $E_{\text{ads}}^{\text{disp}}$ is calculated as -2.73 eV being slightly larger than the isolated monomer. While the molecules/oxide interaction, $E_{\text{int}}^{\text{monolayer}}$, is computed as -5.26 eV, the term for the intermolecular interactions, $E_{\text{mol}}^{\text{inter}}$, is calculated as -0.51 eV. As in the monomer case, cyano nitrogens of each Pyr molecule is well positioned on the surface Ti atoms with a measured distance of ≈2.2 Å. The smallest distance between two cyano nitrogens of two Pyr molecules becomes 3.1 Å. This configuration results in distortion energy of the monolayer, $E_{\text{dist}}^{\text{monolayer}}$, to be 1.13 eV.

Relatively large values of the interaction energies are obtained for both CoPyr@rutile and Pyr@rutile complexes which are attributed to the substantial distortion of the monolayer structures on the TiO_2 (110) surface. Although there is repulsive interaction between the cyano nitrogen atoms of adjacent molecules, they still adsorb on the surface in a row direction similar to the monomer case. The smallest distance

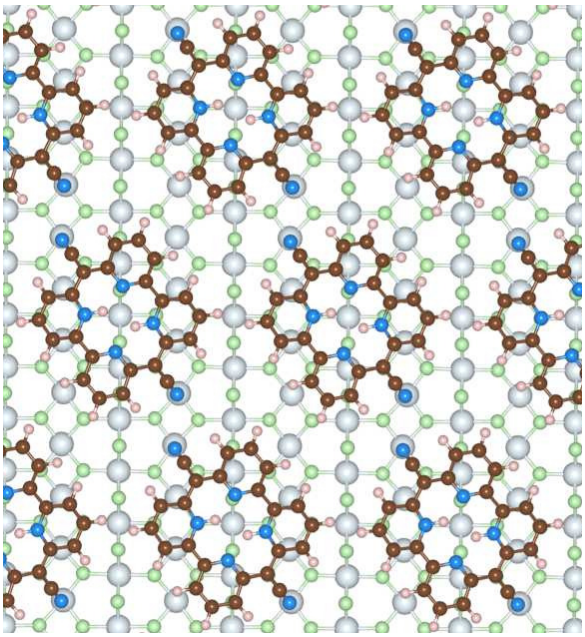

Figure 5.22: Optimized $c(2 \times 8)$ Pyr monolayer configuration on TiO_2 (110). For clarity only the surface layer of TiO_2(110) is depicted. Color code: see the previous figures.

between two cyano nitrogen atoms of two Pyr (CoPyr) molecules becomes $\approx$ 3 Å with this adsorption configuration. In contrast, by relaxing the molecules in the gas phase, without the substrate, flat structures are obtained with $\approx$ 7 Å separated cyano nitrogen atoms. Compared to the formation of disordered Co-Phthalocyanine structures on TiO_2(110) [153], our results suggest that the attractive molecule–substrate and intermolecular interactions together with the van der Waals interaction support the formation of ordered assemblies and sustain the stability of the monolayers on the oxide surface.

Experimental UP-spectra and calculated TDOS for optimized monolayer geometries of both CoPyr@rutile and Pyr@rutile complexes are shown in Figure 5.23. As a general observation, Cobalt incorporation does not induce a drastic variation of the measured UP-spectra, (Figure 5.23c). The apparent shift of the valence band edge (blue dotted line) is about 140 meV smaller after Co-metalation CoPyr/TiO_2 homo and homo-1 binding energies become 1.94 ± 0.10 eV and 2.66 ± 0.10 eV, respectively. The molecular states remain dispersionless, and the work function does not change significantly with respect to Pyr@rutile, ($\Phi_{\mathrm{CoPyr}} = 3.8 \pm 0.1$ eV). DFT results give the conduction band minimum of Pyr@rutile directly at Fermi Energy (E_F) due to the apparent shift of the measured valence band edge, while conduction band minimum of CoPyr@rutile seems to be reasonable. Overall, DFT predicts the relative distances

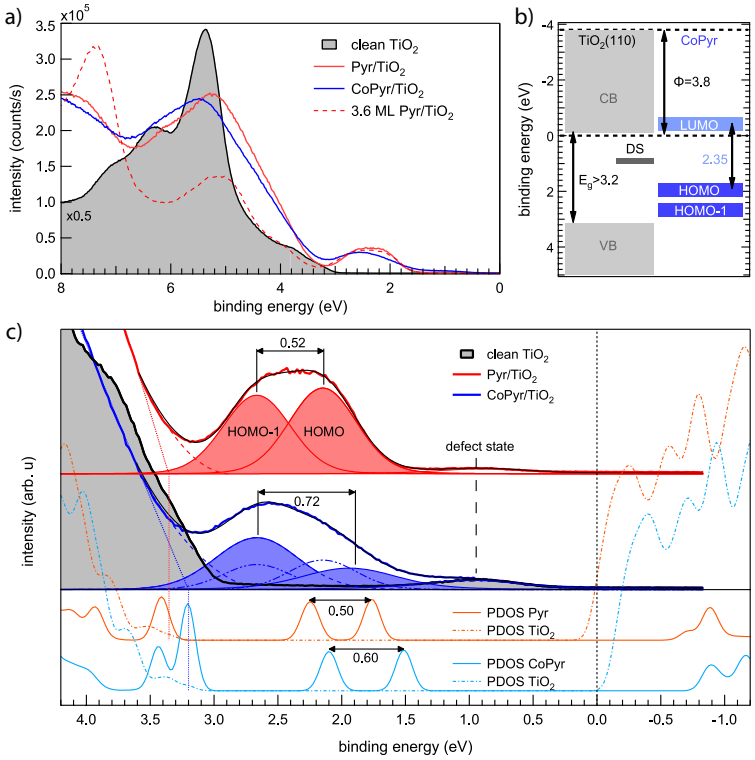

Figure 5.23: (a) Normal emission UP-spectra of clean TiO_2(110) (black), with 1 ML Pyr (red) and CoPyr (blue, 60% metalated). Molecular states appear within the bandgap of the substrate. (b) Energy scheme summarizing the key results of the CoPyr/TiO_2 system. The lumo position is deduced from the measured position of the homo and the homo-lumo gap of 2.65 eV obtained from our DFT calculations. (c) Bandgap region with arbitrary offsets added to the Pyr/TiO_2 spectrum. A deconvolution by Voigt functions locates the homo and homo−1 of Pyr/TiO_2 at 2.14 eV and 2.66 eV and of CoPyr/TiO_2 at 1.94 eV and 2.66 eV, respectively. The lower part of (c) shows the discrete levels calculated by DFT for Pyr/TiO_2 and CoPyr/TiO_2, aligned to the valence band onset of the corresponding spectrum. Note that darker red/blue lines correspond to substrate levels, while orange/cyan lines are located at the molecule. See Ref. [68] for more details.

between the homo and homo−1 of Pyr and CoPyr quite well, but slight misalignment of the molecular states with respect to the substrate bands is observed. As summarized in Figure 5.23(b), the calculated homo-lumo gap of CoPyr becomes 2.35 eV. The present band alignment is favorable for the absorption of visible light by the CoPyr molecules and subsequent injection of these excited electrons from the CoPyr lumo to the conduction band of TiO_2(110) [87]. The same holds also for Pyr where the calculated homo-lumo gap is 2.45 eV.

Experimentally it is shown that Co insertion significantly increases stability of the complex against continuous UV-irridation. As mentioned above, our DFT calculations for Pyr and CoPyr adsorbed on TiO_2(110) found that the molecular level scheme does not change dramatically upon metalation (Figure 5.23(c), lower part). Therefore, the increased stability of CoPyr should be related to a dynamic effect. The fast degradation of the adsorbed Pyr molecules due to UV-irradiation could in principle have two different origins: direct photoexcitation of the molecule yields electronically excited states with potential energy surfaces that lead to dissociation. On the other hand, hot electrons resulting from photoexcitation of the TiO_2 substrate could fill unoccupied molecular states with strongly antibonding character, leading to the same result. The incorporation of the Co atom introduces additional electronic degrees of freedom on the molecule and increases thus the number of de-excitation channels for electronically highly excited molecular states. Along with these lines, the possible explanation for the fast degradation of the adsorbed Pyr molecules due to UV-irradiation could be that the readiness of the Co^{2+} ion for changing its charge state offers efficient channels for hot electrons from the substrate to dwell on the molecule without triggering decomposition. In fact, this is the same variability of the oxidation-state which renders CoPyr an efficient water reduction catalyst in solution [14].

Calculations of the charge redistribution of neutral and negatively charged CoPyr molecules support the mentioned potential buffer property of the Co ion. The comparison of electronic redistribution of neutral and negatively ($-1e$) charged Pyr and CoPyr molecules in vacuo reveals that the homo-lumo gap of Pyr^- (0.26 eV) is significantly narrower than that of neutral Pyr (2.23 eV). The homo of Pyr^- becomes 1.41 eV less stable than the homo of Pyr. Additionally, the difference of homo and homo-1 states becomes more significant in Pyr^-. While homo and homo-1 show an energy difference of 1.81 eV in Pyr^-, it is only 0.5 eV in Pyr. For $CoPyr^-$, instead, we do not observe significant changes of the homo-lumo gap or in the difference of homo and homo-1. Our calculations show that the singlet state of $CoPyr^-$ is more stable than the triplet state by 0.46 eV. Therefore, further calculations were carried out using a singlet spin state. The homo-lumo gaps are calculated as 1.57 eV and 2.02 eV for $CoPyr^-$ and neutral CoPyr, respectively. Contrary to the Pyr^- case, the homo of $CoPyr^-$ becomes 1 eV more stable than its neutral counterpart. While the homo and homo-1 difference is 0.21 eV in $CoPyr^-$, it is 0.72 eV in CoPyr. A Bader charge analysis [152] shows that charges localize on the Co center for CoPyr in vacuo

and similarly for CoPyr/TiO_2 (around $+1.02e$). In comparison, the Co center has $+0.71e$ of charge for the $CoPyr^-$ molecule at vacuum.

5.4 Conclusions

We have investigated the adsorption of CoPyr and Pyr on the stoichiometric rutile (110) surface. The optimized adsorption geometry obtained from DFT calculations where molecules straddle the bridging oxygen rows in a convex fashion are consistent with the experimental STM images of the adsorbed molecules. We observe electronic structure rearrangements occurring upon adsorption, mainly due to the interaction of the cyano groups of CoPyr and Pyr with the five-coordinated Ti atoms of rutile(110). The projected densities of states on the different involved species reveal that the molecular orbitals on the N_{CN} atoms undergo a rehybridization, the homo is located at the molecule, and the lowest unoccupied states of CoPyr (Pyr) are shifted to higher energies. Effects of the electronic redistribution are also recognized from the Ti_{5c} PDOS and the polarization of the electronic density across the molecular plane. Monomer adsorption calculations show that the first band of unoccupied states is mainly on rutile and extends from 1.1 to 2.0 eV, with a maximum at 1.5 eV for CoPyr and 1.61 eV for Pyr. The lowest unoccupied states localized on CoPyr (Pyr) are instead beyond 2.5 eV (2.6 eV), i.e., at higher energy with respect to the lumo of the gas phase molecule. At monolayer coverage, in agreement with the experiments, our DFT-calculation show that molecular states lie within the substrate bandgap for both, Pyr and CoPyr, with only minor energy shifts upon metalation.

Concerning photo-stability of the complexes, continuous UV-irradiation applied by the experimentalists induces rapid decomposition of the Pyr molecules, while Co-incorporation is found to stabilize the molecules against photo- induced degradation. This is attributed to the additional de-excitation channels for electronically highly excited molecular states resulting from the variability of the Co oxidation state.

Overall, the adsorption produces a significant reduction of the energy gap with respect to both pristine rutile TiO_2 and the isolated molecules, which should facilitate absorption of light in the visible range. On the other hand, but for a rigid shift with respect to the homo, we do not observe strong modifications of the electronic structure at the Co(II) center. From these results we expect that the catalytic properties of

CoPyr are preserved upon adsorption. Besides, strongly enhanced stability of CoPyr is of particular importance for its potential use in dye sensitization of TiO_2.

6 Pyrphyrin and Co-Pyrphyrin on Au(111): The Effects of Herringbone Reconstruction and Dynamics of Metalation [71, 154]

The (111) surface of gold is known to undergo a complex reconstruction under UHV conditions, [67] which is clearly visible from STM. The reconstructed surface presents areas with different stacking of the topmost two layers. In the STM image, these areas appear as regular stripes of three types along the (110) axis [155]. They correspond to the fcc, hcp, and intermediate stacking (transition region), thus changing the surface symmetry from C_{3v} (fcc (111) surface) to C_1 [156]. The modulated local atomic coordination is expected to have an influence on the adsorption and aggregation of atoms and molecules. In particular, in the transition region the surface energy is higher and the substrate is more reactive, [157, 158] which, indeed, might favor the catalysis of reactions and the aggregation of clusters [159–161]. A recent experimental study [162] on the adsorption on reconstructed Au(111) of Co-octaethylporphyrin and Co-tetraphenylporphyrin shows a splitting of the Co $2p_{3/2}$ peak in the XP spectra, which has been attributed to the stronger interaction on the more reactive transition region of the reconstruction pattern.

This chapter focuses on the effects on the adsorption due to the gold reconstruction and the registry, as well as the discussion on possible structures and on the stability of the monolayer. Besides, we simulate the metalation process, revealing the intermediate steps and the conformational changes undertaken by the adsorbates along the reaction path. In the following, we briefly describe the applied methodology and the structural models. The most probable adsorption configurations for the monomers of Pyr and CoPyr are compared by addressing the electronic structure features, and by stressing the influence of the reconstruction and of the local registry. Finally, running AIMD we discuss the reaction mechanism that leads to the metalation of the self-assembled Pyr molecules upon co-adsorption of atomic Co. We also demonstrate the presence of an intermediate state along the metalation process and the rearrangement

of the monolayer after the reaction is completed, in agreement with the experimental observations [71].

6.1 Computational Methodology

The electronic structure calculations reported in this chapter are performed at the Kohn-Sham DFT level, employing the Gaussian and plane wave (GPW) formalism, as implemented in the CP2K/QUICKSTEP package [163]. Only the valence electrons are treated explicitly, with valence shells containing 11, 17, 4, 1, and 5 electrons for Au, Co, C, H, and N, respectively. The interaction between the valence electrons and the atomic cores is described through norm-conserving Goedecker–Teter–Hutter (GTH) pseudo potentials [112]. The molecular orbitals are expanded in Gaussian type orbitals using double-zeta plus polarization (DZVP) basis sets, which have been optimized on molecular geometries (Mol-Opt method) [113]. The auxiliary PW basis used to represent the valence electron density in reciprocal space has an energy cut-off of 500 Ry.

As exchange correlation functional the spin polarized general gradient approximation by Perdew–Burke–Enzerhof (PBE) [80] augmented with a correction for the van der Waals (vdW) interactions is used. We are going to show that this level of theory is sufficiently accurate to reproduce the reconstruction of the Au(111) surface, in good agreement with previous works [164]. PBE is also known to be adequate for capturing the interactions in porphyrin/Au systems, i.e., the hybridization of the porphyrin states with the Au d-band [165].

We use as a reference Au-bulk lattice parameter of 4.17 Å. The Au surface is always described via a slab model, with the exposed plane perpendicular to the Cartezian axis. Periodic boundary conditions are always applied. To prevent any interaction between periodically replicated slabs, 20 Å of vacuum space are added along the surface normal.

The study on the adsorption site and registry of the Pyr and CoPyr monomers is carried out using a 22×6 Au(111) slab with 4 layers, where the three topmost layers are relaxed, whereas the fourth is kept fixed at the bulk coordinates. This slab model contains 534 Au atoms. For the structural optimization and the ab-initio molecular dynamics (AIMD) simulations of the CoPyr-monolayer, instead, the un-reconstructed

Au(111) surface model is used, which allows a much smaller simulation cell. The ideal 9×9 Au(111) slab is used, including four layers, of which the bottom one is fixed.

The AIMD simulations are carried out on the Born-Oppenheimer surface, using for the nuclei's equation of motion an integration time step of 0.8 femtoseconds. The temperature is controlled by coupling the system with an external thermostat. In order to simulate the metalation of the adsorbed Pyr, the MD is accelerated by applying the metadynamics methodology (MTD) [105]. MTD accelerates the exploration of the accessible phase space, thus allowing the simulation of rare events that otherwise would require unfeasibly long simulation times. It is based on the definition of a few collective variables (CVs), which are conveniently selected to describe the most relevant structural changes. For the metalation process, one CV describes the changes in coordination state of the Co atom, which is going to be inserted in the Pyr's pocket. The pyridine N atoms are initially coordinated to H and after metalation to Co. Hence, also the N-H average coordination number has been selected as CV.

6.1.1 Au(111): The Herringbone Reconstruction

In order to reproduce the characteristics of the reconstructed Au(111) surface, as known from experiment, we tested three different approaches to correct the PBE functional with the proper amount of dispersion contributions. These are the vdW density functionals by Vydrov–Voorhis (rVV10) [98, 99] in revised form, and Dion–Rydberg–Schroder–Langreth–Lundqvist (DRSLL), [100] as well as the simpler empirical Grimme-D3 correction [96].

When applied to the 22 × 6 Au(111) slab model, all the three approximations give a corrugated surface, partitioned in fcc, hcp and transition stripes, where the top-layer atoms in the transition region are displaced outwards by about 0.05∼0.1 Å with respect to the atoms in the fcc and hcp areas. The change in height with respect to the position of the topmost Au atoms of an ideal Au(111), $\delta h = h - h_{\text{ideal}}$, is plotted in Figure 6.1(a). δh varies along the $[1\bar{1}0]$ direction, while moving over fcc, transition, hcp, transition, and again fcc in the plot. The rVV10 and DRSLL vdW functionals give similar morphologies of the topmost layer, but the overall upwards displacement is larger with DRSLL, which is consistent with a generally less binding functional. Otherwise, the proportions between the three different areas are about the same and in agreement with experiment, where fcc, first transition, hcp, and second transition appear with a 34:22:22:22 partitioning [166]. The Grimme-D3 approach

overestimates the width of the transition area, resulting in a 22:30:18:30 distribution. The plot in Figure 6.1(b) shows the lateral displacement $\delta_{[11\bar{2}]}$ along the $[11\bar{2}]$ axis, with respect to the original fcc site. $\delta_{[11\bar{2}]}$ is zero in the fcc region and maximal (~ 0.85 Å) when the atoms occupy hcp sites. Also in this case, we observe that the Grimme-D3 method is more forgiving with respect to displacements from high-symmetry sites, i.e., more atoms sit at intermediate positions and the actual hcp stacking is never properly reached. The DRSLL and rVV10 give similar profiles, also in agreement with previous studies [155].

The more accurate description of the reconstruction pattern by rVV10 is also confirmed by the simulated STM image obtained using the Tersoff–Hamann approximation [102] and shown in Figure 6.1(c). In spite of the analogous peak-to-peak electronic corrugation of about 0.3 Å, the Grimme-D3 model presents far too broad transition domains [167]. All the calculations presented in the following are then carried out using the rVV10-PBE density functional model. The top view of the rVV10-PBE optimized super cell of the reconstructed Au(111) slab is reported in Figure 6.1(d). While in the ideal (111) atomic layer the nearest Au-Au distance is 2.88 Å, the interatomic distances of the reconstructed layer are modulated between this value in the fcc and the shorter 2.80 Å distance in the hcp domains. Such a compression of the reconstructed Au surface along $[1\bar{1}0]$ direction results in a surface strain which is associated with the partial redistribution of the sp electrons [168]. Figure 6.2 shows s and p electrons total density of states (TDOS) on fcc, transition, and hcp domains of the reconstructed surface, as well as on ideal Au surface. As a general observation, states on all domains show discrepancy, depletion and slight shifting, with respect to the states on ideal surface. Different from fcc and transition regions, hcp domain show depletion and splitting of the states in occupied band near Fermi region at around -3 eV.

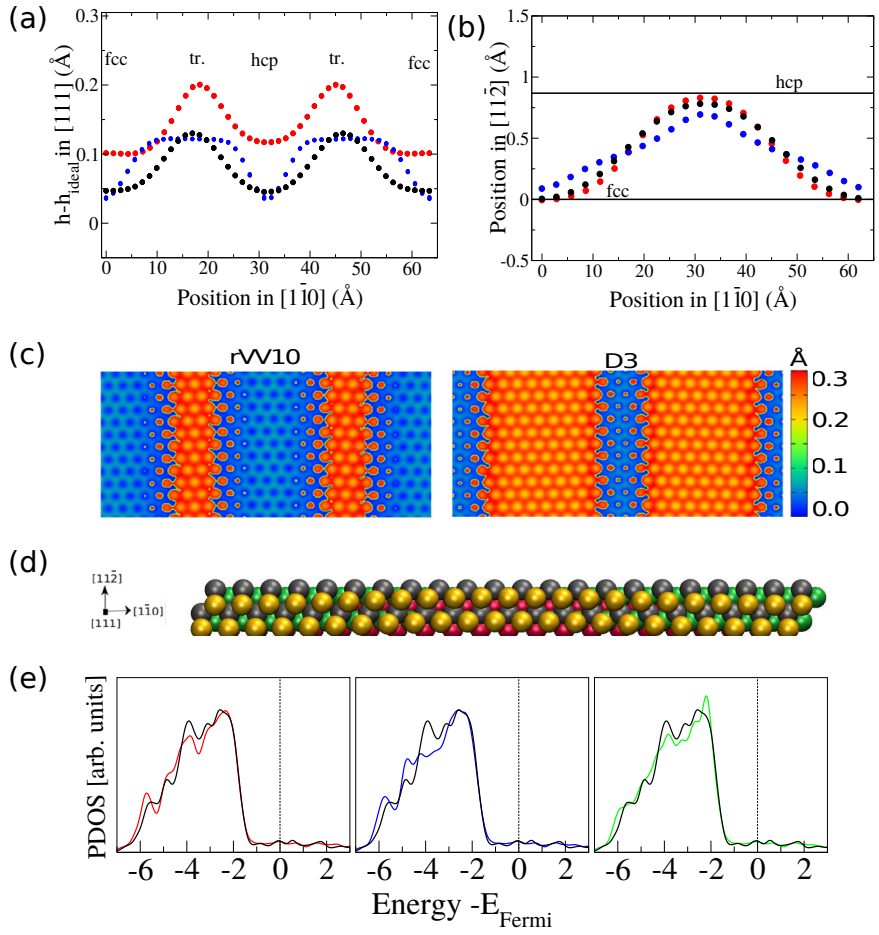

Figure 6.1: Reconstructed Au(111) surface optimized with the three van der Waals schemes. a) Vertical corrugation of the topmost layer with respect to the ideal surface, across the supercell along the [1$\bar{1}$0] axis. b) Lateral displacement of the topmost atoms $\delta_{[11\bar{2}]}$ with respect to their ideal fcc site. Moving over the three domains the displacement changes from ∼0 Å (fcc), ∼0.6 Å (tr.), to ∼0.85 Å (hcp). The results obtained with rVV10 are plotted in black, with DRSLL in red, and with Grimme-D3 in blue. c) Simulated STM image obtained for the rVV10-PBE model (left) and the PBE-D3 model (right). The iso-current surface is taken at an electron density of 6.7 10^{-5} e/Å^3 by applying a bias potential of 0.9 eV. d) Top view of the reconstructed Au(111) supercell optimized with the PBE-rVV10 functional. The top layer atoms are the gold-colored spheres, the second layer is gray, the third green, and the fourth layer, only visible in the transition and hcp areas, is represented by the red spheres. e) Normalized PDOS on the 5d orbitals of the topmost Au atoms belonging to the fcc (left), transition (middle), and hcp (right) domains. Black solid lines indicate PDOS on ideal Au surface.

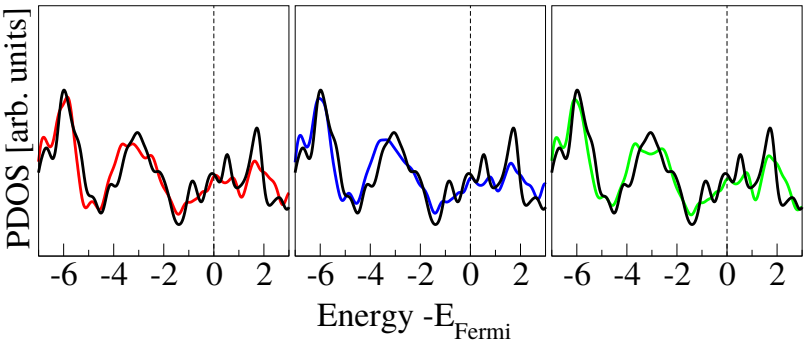

Figure 6.2: Normalized TDOS of the s and p electrons on the topmost Au atoms belonging to the fcc (left), transition (middle), and hcp (right) domains. Black solid lines indicate s and p electrons TDOS on the ideal Au surface. Only the states close to Fermi region are depicted.

The resulting rearrangement of the electronic distribution is also revealed by the projected density of states (PDOS), Figure 6.1(e). The Au-5d states projected on the fcc and hcp regions are very close to the reference PDOS of the ideal surface. In the transition region, instead, the symmetry is reduced, which affects the broadening of the d-band, with the depletion of states around -4 eV causing a shift to higher energy of the band's center.

The reconstruction corresponds to an energy gain that we estimate in terms of the energy difference per unit cell between reconstructed and ideal surfaces, as

$$\Delta E = E_{\text{rec}} - E_{\text{ideal}} - 6E_{\text{bulk}}. \tag{6.1}$$

In the above expression E_{rec} is the energy of the reconstructed 23 $\times$ 6 slab, E_{ideal} is the energy of the ideal 22 $\times$ 6 slab, and E_{bulk} is the energy per Au atom in the bulk. E_{bulk} is obtained by the procedure described in Refs. [169, 170] using a 6$\times$6 slab varying layers from 7 to 12. From our calculations ΔE is -1.33 eV/unitcell, i.e., the herringbone reconstructed slab is more stable than the unreconstructed one, as expected.

6.1.2 Pyrphyrin and Cobalt-Pyrphyrin Adsorption on Reconstructed Au(111)

For the ball and stick sketches of Pyr and CoPyr, we refer to Figure 5.5 in Chapter 5. As already mentioned in Chapter 5, two nitrogens in pyridine rings, N_p, are protonated

in Pyr, while the protons are replaced by the Co(II) cation in CoPyr. In the gas phase, both molecules are planar and along the axis of the cyano groups the CoPyr is slightly shorter (11.78 Å) than Pyr (11.96 Å), due to the interactions between Co(II) and the electronegative nitrogens [87]. The lowest energy spin state of CoPyr is doublet, and the spin density is localized at the Co(II) center.

The adsorption of the monomers Pyr and CoPyr has been investigated by testing different possible adsorption sites. Each optimized structure is characterized in terms of a few structural parameters, describing the actual position and registry and the distortion of the molecule. The interaction is analyzed by considering the different energy contributions. The rearrangements of the electronic distribution are verified by means of the PDOS. The optimization is carried out by relaxing the molecular geometry and the three top-most layers of the Au slab, while the fourth layer is kept fixed at bulk coordinates. The adsorption energy (E_{ads}) is calculated as

$$E_{\mathrm{ads}} = [E_{\mathrm{complex}} - (E_{\mathrm{slab}} + n_{\mathrm{mol}} E_{\mathrm{monomer}})]/n_{\mathrm{mol}} \tag{6.2}$$

where E_{complex} is the total energy of the complex, E_{slab} is the energy of the optimized slab, E_{monomer} is the energy of the optimized molecule in vacuum, and n_{mol} is the number of molecules. For the adsorption of the monomer, n_{mol}=1. The dispersion contribution to the adsorption energy can also be determined by extracting only the vdW density functional term

$$E_{\mathrm{ads}}^{\mathrm{disp}} = [E_{\mathrm{complex}}^{\mathrm{disp}} - \left(E_{\mathrm{slab}}^{\mathrm{disp}} + n_{\mathrm{mol}} E_{\mathrm{monomer}}^{\mathrm{disp}}\right)]/n_{\mathrm{mol}} \tag{6.3}$$

The molecular distortion energy, ($E_{\mathrm{mol}}^{\mathrm{dist}}$) is the energy loss due to the geometrical changes induced by the interaction with the surface,

$$E_{\mathrm{mol}}^{\mathrm{dist}} = E_{\mathrm{mold}} - E_{\mathrm{monomer}} \tag{6.4}$$

where E_{mold} is the energy calculated in vacuum, but at the same coordinates of the molecule in the complex. In a similar way, $E_{\mathrm{slab}}^{\mathrm{dist}}$ is calculated by subtracting the energy of the optimised slab from the energy of the slab at the coordinates of the complex,

$$E_{\mathrm{slab}}^{\mathrm{dist}} = E_{\mathrm{slabd}} - E_{\mathrm{slab}} \tag{6.5}$$

The neat interaction energy is defined as

$$E_{\mathrm{int}}^{\mathrm{monomer}} = E_{\mathrm{complex}} - (E_{\mathrm{mold}} + E_{\mathrm{slabd}})\,. \tag{6.6}$$

The experimental study by Mette et al. [71] shows that the CoPyr molecules assemble and form a hexagonal super lattice with a lattice constant of a_{super}≈12.46 Å on the reconstructed Au(111) surface. This a_{super} corresponds to 4.33×a_{surf}, where a_{surf}≈2.88 Å is the surface lattice parameter. However, the relative orientation of the molecules can not be resolved, also because the STM images are obtained at room temperature and a substantial thermal mobility has to be taken into consideration. We have then modeled the CoPyr monolayer placing four molecule on the ideal 9×9 Au(111) slab, which is the smallest model approximately commensurate with the experimental superstructure (a'_{super}≈12.77 Å). Several possible configurations are tested by rotating the molecules with respect to each other, still trying to satisfy the criteria for the optimal adsorption registry. Each initial structure is optimized and its stability is evaluated in terms of two energetic parameters, the molecules–metal interaction ($E_{int}^{monolayer}$) and the distortion energy of the monolayer, ($E_{dist}^{monolayer}$), calculated as

$$E_{int}^{monolayer} = [E_{complex} - (E_{monolayerd} + E_{slabd})]/n_{mol} \tag{6.7}$$

and

$$E_{dist}^{monolayer} = [E_{monolayerd} - E_{monolayer}]/n_{mol} \tag{6.8}$$

respectively. In the above expressions, $E_{monolayer}$ is the energy of the monolayer computed as free standing and $E_{monolayerd}$ is the energy calculated in vacuum with the same coordinates of the monolayer in the complex. n_{mol} is the number of molecules in the simulation cell which is 4.

In order to simulate the metalation process, a similar model is used, where the monolayer is initially constituted of four Pyr molecules. After the equilibration at room temperature, which allows the optimal rearrangement of the molecules, one single Co atom is added, from above in the vicinity of the monolayer. By running AIMD from this initial configuration, we are able to simulate the direct metalation occurring upon Co deposition.

6.2 Results and Discussion

6.2.1 Monomer Adsorption On The Reconstructed Au(111) Surface

We first identify the most stable adsorption registry of Pyr and CoPyr on the fcc domain of the reconstructed Au(111) surface. The molecule is initially placed flat

above the surface, at about 4 Å. In both cases, five different orientations of the cyano group axis with respect to the [1$\bar{1}$0] surface axis are considered, i.e., at angles of 0°, 19°, 24°, 60°, and 73°. The top views of all the optimized geometries are shown in Figure 6.3 for Pyr/Au(111) and Figure 6.4 for CoPyr/Au(111).

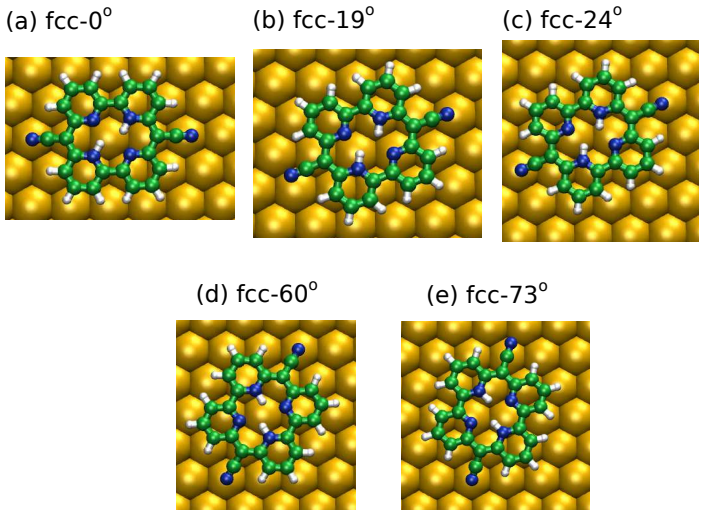

Figure 6.3: Five different optimized structures of the Pyr@Au complex. Pyr is adsorbed on fcc site of the reconstructed surface with 0°, 19°, 24°, 60°, and 73° tilted angles with espect to [1$\bar{1}$0] direction of the Au slab. Color code: blue: N, green: C, white: H, yellow: Au.

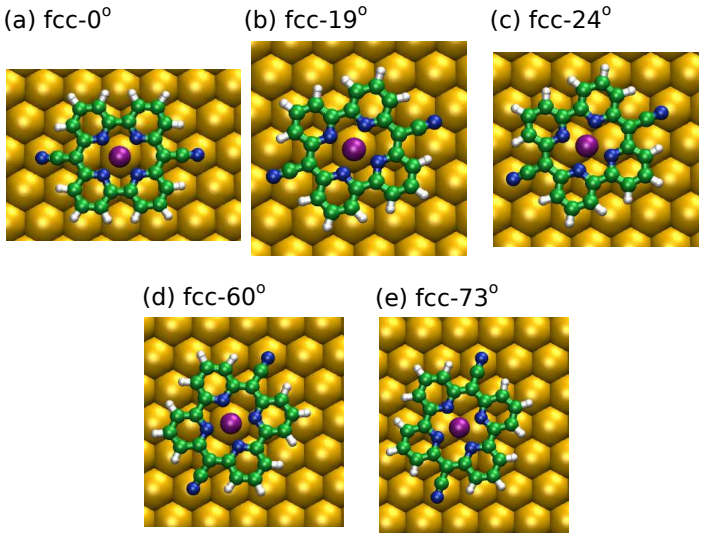

Figure 6.4: Five different optimized structures of the CoPyr@Au complex. CoPyr is adsorbed on fcc site with 0°, 19°, 24°, 60°, an Color code: blue: N, green: C, white: H, purple: Co, yellow: Au.

The corresponding computed adsorption energies and the separated contributions due to dispersion and distortion are reported in Table 6.1. The adsorption strength is

Table 6.1: Adsorption, interaction, dispersion, and distortion energies characterizing Pyr and CoPyr adsorbed with five different registries on the fcc domain.

Model	E_{ads}	$E_{\text{ads}}^{\text{disp}}$	$E_{\text{int}}^{\text{monomer}}$	$E_{\text{mol}}^{\text{dist}}$	$E_{\text{slab}}^{\text{dist}}$
			Pyr		
0°	-3.56	-3.56	-3.71	0.10	0.05
19°	-3.53	-3.62	-3.65	0.06	0.06
24°	-3.61	-3.66	-3.78	0.10	0.08
60°	-3.65	-3.54	-3.72	0.02	0.06
73°	-3.61	-3.58	-3.67	0.02	0.04
			CoPyr		
0°	-4.15	-3.92	-4.55	0.24	0.16
19°	-3.97	-3.88	-4.27	0.18	0.12
24°	-4.00	-3.94	-4.41	0.26	0.15
60°	-4.16	-3.91	-4.48	0.17	0.15
73°	-3.97	-3.98	-4.20	0.17	0.07

generally rather weak. The differences among the five orientations of both CoPyr and Pyr are small, suggesting that the molecules should be rather mobile at finite temperature, thus allowing rearrangements and the aggregation of assemblies, as indeed observed experimentally. The interaction strength is maximized by locating the cyano N atoms and the Co center on top of the closest surface Au atoms. For both Pyr and CoPyr, this is optimally obtained by minimal distortion of the molecule when the rotation angle is at 60°. The ball and stick sketches shown in Figure 6.6(a) and (b) show that the optimized molecules are only slightly bending along the cyano group axis to favor the interaction with the surface. In the case of CoPyr, Co atom is sitting on top of one Au atom, which is slightly lifted. The dominant attractive contribution is associated to the dispersion forces, strongly favoring the horizontal adsorption geometry. The presence of the Co atom in the molecular pocket determines the stronger binding of CoPyr with respect to Pyr, thanks to the partial electronic redistribution around the metallic center. The distortion of both molecule and metal are minimal, but still slightly larger in the case of CoPyr, due to the attractive Co-Au interaction. The most relevant structural parameters characterizing the optimized geometries, as the distance between the two cyano N atoms and the height of the molecule above

the surface, are summarized in Table 6.2. The graphical description of the measured distances shown in Table 6.2 is reported in Figure 6.5.

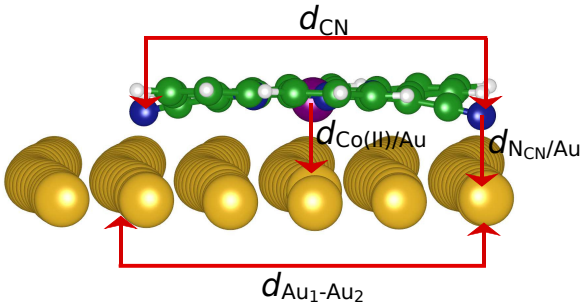

Figure 6.5: Ball and stick representation of CoPyr@Au showing reported distances in Table 6.2. d_{CN} is the distance between the two cyano N; $d_{Au_1\text{-}Au_2}$ is the distance between the two top Au atoms closest to the N_{CN}; $d_{N_{CN}/Au}$ is the distance between N_{CN} and the closest Au on the surface; $d_{Co(II)/Au}$ is the distance between Co and the closest Au on the surface. Only surface Au atoms are shown. Color code: blue: N, green: C, white: H, purple: Co, yellow: Au.

The d_{CN} values are in general smaller than in vacuum, because the two cyano groups tend to bend towards the metal in order to favor the interaction. This effect is more pronounced when the N_{CN} are closer to top Au sites, i.e., 0°, 24°, 60°. Indeed, these geometries are also characterized by stronger binding. $d_{Au_1\text{-}Au_2}$ varies depending on the orientation of the molecule, since only in the case of the 0° and 60° these two atoms belong to an atoms' row laying along a crystallographic axis. Moreover, upon relaxation, Au_1 and Au_2 may also move to favor the binding. In the case of CoPyr, the closest $d_{Co(II)\text{-}Au}$ distance is also a relevant parameter. Indeed, the larger variations in the interaction energy associated with the CoPyr registry may be attributed to the different position of Co relative to the closest Au atom.

Table 6.2: Structural parameters for the adsorbed Pyr and CoPyr over the fcc domain. d_{CN} is the distance between the two cyano N (11.78 Å in vacuum); $d_{Au_1\text{-}Au_2}$ is the distance between the two top Au atoms closest to the N_{CN}; $d_{N_{CN}\text{-}Au}$ is the distance between N_{CN} and the closest Au; $d_{Co(II)\text{-}Au}$ is the distance between Co and the closest Au on the surface; Δh_{Au} is the maximum vertical displacement the surface Au atoms; $h_{mol/slab}$ is the average height of the molecule over the surface, taking as reference the average height of the topmost Au atoms; μ_z is the vertical component of the molecular dipole moment (zero in vacuum). All distances are given in Å, the dipole in Debye.

Model	d_{CN}	$d_{Au_1\text{-}Au_2}$	$d_{N_{CN}\text{-}Au}$	$d_{Co(II)\text{-}Au}$	Δh_{Au}	$h_{mol/slab}$	μ_z
			Pyr				
0°	11.78	11.42	2.49, 2.70		0.05	3.19	0.191
19°	11.86	12.54	2.52, 3.04		0.10	3.17	0.191
24°	11.80	12.54	2.52, 2.53		0.08	3.14	0.190
60°	11.76	11.81	2.50, 2.52		0.05	3.19	0.191
73°	11.84	10.66	3.24, 3.25		0.04	3.16	0.191
			CoPyr				
0°	11.63	11.49	2.50, 2.54	2.73	0.20	3.08	0.187
19°	11.73	12.56	3.22, 3.27	2.72	0.20	3.09	0.188
24°	11.64	12.51	2.47, 2.55	3.02	0.11	3.06	0.187
60°	11.64	11.85	2.48, 2.54	2.74	0.20	3.08	0.187
73°	11.70	10.70	2.80, 2.87	3.16	0.01	3.03	0.186

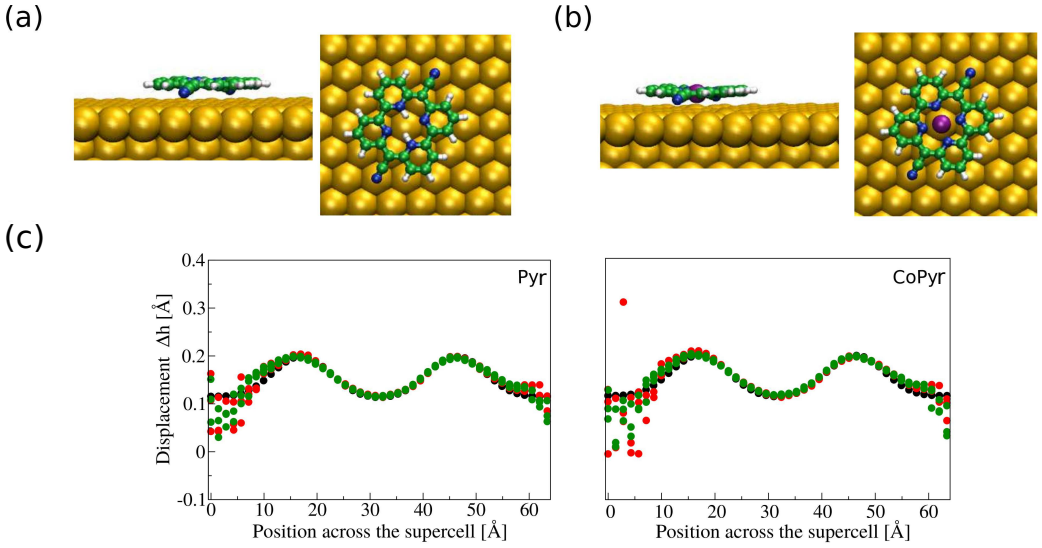

Figure 6.6: Side view and top views of the optimized structures of a) Pyr and b) CoPyr on the reconstructed Au(111) surface. (green: C, white: H, purple: Co, blue: N, and yellow: Au). c) Corrugation of the Au surface across the supercell upon Pyr and CoPyr adsorption. Red dots for 60° molecular alignment, green for 73°, and black for bare surface.

In order to better understand the role of the adsorption registry, we analyze in more detail two orientations, the one at 60° and the one at 73°. In spite of the fact that the total distortion energy of the Au slab is very small, we observe that locally the Au atoms in closer contact with the N_{CN} and Co (for CoPyr) undergo a measurable vertical displacement. When the cyano N are placed on top of the underneath Au atom, the molecule bends slightly, thus reducing the N-Au distance as well as d_{CN}. The surface responds to the interaction with small vertical displacements of the closest Au atoms (see Figure 6.6(c)). It is observed that in the fcc area, where the monomer is placed, a few Au atoms move inwards, due to the repulsive interaction with the most bulky part of the molecule. However, the Au atoms below the N_{CN} are slightly displaced upwards, and the effect is only marginally more pronounced in the case of the 60° orientation (red dots). The largest Au displacement, though, is clearly associated with the interaction with Co, and it occurs only if the metal center is placed at the atop site, i.e., when CoPyr is rotated by 60°. All over the rest of the super cell the corrugation profile remains unperturbed with respect to the bare reconstructed surface (back dots).

The PDOS on the N and Co reveal how the molecular states are redistributed due to the interaction with the metal, see Figure 6.7(a). The comparison with the PDOS computed for the molecule in vacuum (black thin line) shows the broadening of the occupied N_{CN} band, which is associated with the already discussed interaction of the cyano group with the surface. In particular, when the molecule is optimally aligned with the Au atomic row (60°), there is an additional down shift of the band, consistent with the stabilisation of the adsorption. The other relevant effect is the depletion of the highest occupied Co-3d states, pinned at the Fermi energy, suggesting a partial hybridization with the Au surface states. The rearrangement is expected to be more effective when the Co atom is at the atop site, however this does not appear evidently from the Co-3d PDOS. On the other hand, by restricting the Au-5d PDOS only to the atoms in closer contact with either the Co or the N_{CN} atoms and zooming-in close to the Fermi energy (Figure 6.7(b)), the expected increment associated with the interaction with the adsorbate becomes visible. This increment is, indeed, more pronounced in the case of the 60° molecular alignment.

The electron density difference maps confirm this picture. The cuts across $\Delta\rho(\mathbf{r})$ shown in Figure 6.7(c) confirm that the largest electronic rearrangements occur around the N_{CN} and Co atoms. The N_{CN} atoms are more electronegative than the Au atoms. This induces some density depletion above the surface, below N_{CN}, and the corre-

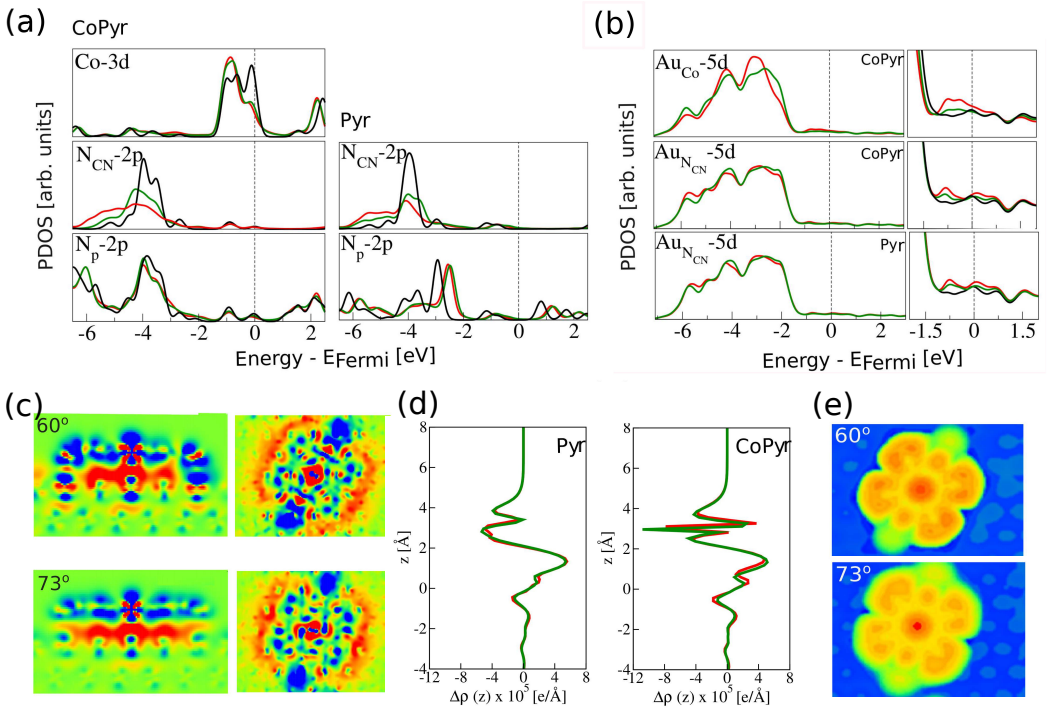

Figure 6.7: a) PDOS on Co (3d), for CoPyr, N_{CN} (2p), and N_p (2p) of CoPyr and Pyr. Red for the 60° molecular alignment, green for 73°, and black for CoPyr and Pyr in vacuum. b) PDOS on the Au atoms (5d) closest to Co, for CoPyr, and closest to N_{CN}, for both Pyr and CoPyr. The right panels show the zoom-in of the region around the Fermi energy. The distributions are normalized by the number of atoms. c) Cut across the electron density difference maps, $\Delta\rho(r)$, for 60° and 73° rotated CoPyr. The cutting planes pass through the molecular center along the cyano axis (left) and through the pyridine plane (right). The color scale indicates accumulation of charge with red (+0.027 e/Å^3) and depletion with blue (-0.027 e/Å^3). d) 2D integrated density difference, $\Delta\rho_{xy}(z)$, plotted along the slab's perpendicular axis for Pyr and CoPyr. e) Simulated STM images of CoPyr adsorbed on the reconstructed Au surface. The images have been generated with a bias potential of -0.8 eV, selecting the iso-density surface corresponding to 10^{-5} e/Å^3. The color scale from blue to red spans a height's change of 3.5 Å.

sponding accumulation around the cyano groups. On the other hand, the electrons around Co are polarized toward the surface, resulting in the charge accumulation below the molecule. From the $\Delta\rho(\mathbf{r})$ it is also observed that, while in 60° alignment only one Au atom is involved in the interaction with Co, with the 73° orientation two Au atoms are equally contributing.

The polarization along the vertical axis are quantified by calculating the 2D-integrated density difference, $\Delta\rho_{\mathrm{xy}}(z)$ see Equation 5.9 in Chapter 5, and shown in Figure 6.7(d). A dipole moment can be measured along the z axis, which is estimated as $\mu_{\mathrm{z}} = \int \rho_{\mathrm{xy}}(z) \cdot z dz$. The resulting μ_z is around 0.2 Debye. The simulated STM images of the CoPyr with the 60° and 73° orientation are also reported in Figure 6.7(e). We observe that the Co center and the pyrphyrin ligands look brighter for the 60° registry, which should be attributed to the more pronounced bending along the cyano axis and the associated electronic rearrangement.

Figure 6.8(a) and (b) show corresponding electron density difference maps of 60° and 73° oriented Pyr molecules on reconstructed Au surface. Electrons are slightly polarized and electron accumulation is observed on the surface under the pyridine rings. In 60° rotated configuration both $\mathrm{N_{CN}}$ atoms are involved in interaction with underneath Au atoms as in the case of CoPyr/Au(111). On the other hand, only one $\mathrm{N_{CN}}$ atom in 73° placed Pyr molecule has a direct interaction with surface Au atom.

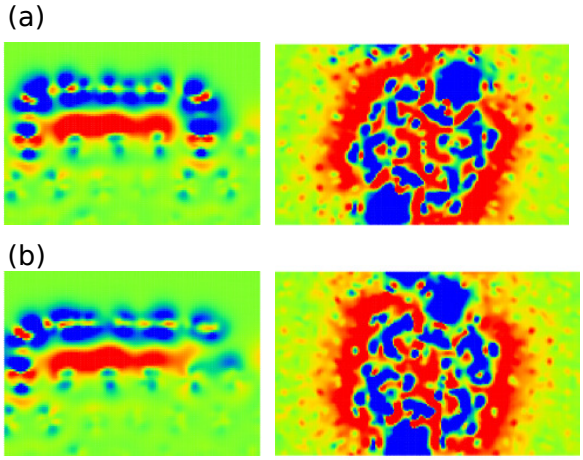

Figure 6.8: Electron density difference maps, $\Delta\rho(r)$, for (a) 60° and (b) 73° rotated Pyr. Side and top planes are shown in left and right panels, respectively. The color scale indicates accumulation of charge with red (+0.027 e/Å^3) and depletion with blue (-0.027 e/Å^3).

In the transition and hcp regions, the different in-plane Au-Au distances might have an effect on the optimal adsorption geometry. Also the less symmetric atomic

environment around the Au atoms in the transition region might have an influence. The resulting electronic rearrangement, as revealed by STM, has been, indeed, associated to a somewhat enhanced reactivity. These features combined with the XPS observation that molecules show different adsorption modes on the reconstructed surface, [162] might suggest that over the different areas of the reconstruction pattern the interaction with the metal present a different character. In order to clarify the role of the reconstruction, we have examined the adsorption configurations also at the hcp and transition areas, finding, though, that the 60° orientation still corresponds to the lowest energy. The variation in interaction energy is minimal (0.03 eV) among the three geometries, over the fcc, transition and hcp areas. Actually, once Pyr or CoPyr are adsorbed, the lateral position of the directly involved Au atoms slightly relaxes, and this evens up the initially different interatomic distances. From the inspection of the PDOS, the electronic rearrangements occurring upon adsorption result to be substantially equivalent over the three areas.

From these results, we conclude that the optimal adsorption geometry is not significantly affected by the specific reconstruction's domain. On the other hand, the misalignment of the molecule with respect to the preferred orientation can explain the variations in the XPS signals, due to the modification of the registry with respect to the surface. From the evaluation of the adsorption energy, it appears that the rotation of the molecules with respect to the underlying surface is not that unlikely. It is reasonable to assume that during the assembly of the molecular monolayer at room temperature, the intermolecular interactions prevail in determining the internal arrangement. The packing's optimisation at high coverage maximise the dominant vdW contributions. Under these conditions, only a subset of molecules are going to be effectively aligned with the 60° orientation. In addition, above room temperature rotational movements and partial rearrangements play also a role.

6.2.2 CoPyr Self Assembly

Under high coverage conditions (1ML), the Pyr molecules self-assemble into a hexagonally-ordered molecular superstructure, where each molecule covers an area associated with 17.5 Au atoms [71]. After Co evaporation and annealing, the LEED pattern shows a substantial change in the molecular ordering. The CoPyr monolayer is characterized by a hexagonal unit cell, with vectors aligned with the Au high-symmetry axes [71]. We propose a model of the CoPyr monolayer consisting of four

molecules per supercell over a 9×9 Au(111) slab, each molecule covering an area corresponding to 18.7 Au atoms. We employ an unreconstructed Au(111) surface, since we demonstrated that the reconstruction does not affect the geometry of the adsorbate. On the other hand, the relative orientation of the molecules within the monolayer might play an important role, and cannot be unambiguously resolved experimentally. Therefore, four different molecular patterns have been optimized and compared. The initial structure is constructed by placing the first molecule (label (1) in Figure 6.10a) with the optimal registry in the 60° orientation. Taking the center of molecule 1 as the origin of the 2D supercell, the other three molecular centers are located at the remaining three vertexes. Molecule 2 is the one on the same row as 1 and it is also initially positioned with the 60° orientation. However, neither Co nor N_{CN} are optimally located at top sites. Molecules 3 and 4 form the second row. They are initially positioned such to avoid strong repulsive interactions between N_{CN}, but still trying to favor as much as possible the atop sites. Depending on the relative orientation of the neighboring molecules, the formation of weak N_{CN}-H hydrogen bonds (HB) is also possible. The resulting four monolayers are: model-a (25°– 60°), model-b (80°– 60°), model-c (120°– 60°), and model-d (145°– 60°), where in parenthesis the initial orientation angles for top and bottom rows are given. Each model has been relaxed in vacuum as well as over the Au(111) surface.

Optimized CoPyr Molecules in Gas Phase

The optimization of the 2D assembly in vacuum is useful to investigate independently the role of the interaction between molecules. Optimization of CoPyr molecules (four molecules, 172 atoms) in gas phase is carried out by four different initial configurations. As molecules are free standing, we used same initial configurations of the CoPyr designed for the adsorbed phase, to investigate the effects of the substrate. The models are namely model-a (25°-60°), model-b (80°-60°), model-c (120°-60°), and model-d (145°-60°) in which case first and second angles define rotations of first and second molecular rows with respect to $[1\bar{1}0]$ direction of Au surface, respectively. Inter-molecular interactions are characterized by calculating E_{mols},

$$E_{\mathrm{mols}} = [E_{\mathrm{monolayer}} - n_{\mathrm{mol}} E_{\mathrm{monomer}}]/n_{\mathrm{mol}}, \tag{6.9}$$

respectively. In the above expression, $E_{\mathrm{monolayer}}$ is the energy of the monolayer computed as free standing and E_{monomer} is the energy of one molecule at vacuum. n_{mol} is equal to 4. Optimized molecular configurations in gas phase are depicted in Figure 6.9.

As a general observation, the repulsive forces between the N_{CN}'s lone pairs and the formation of N_{CN}-H HB induce some rotational movements and displacements. The most stable assembly is obtained starting from model-b, which relaxes to an assembly with all molecules on equivalent position. The resulting nearest N_{CN}-N_{CN} distance is 6.0 Å and each N_{CN} forms two equivalent HBs (2.34 Å) with the two closest molecules in the next row, see Table 6.3. The aggregation energy, with respect to the monomer in vacuum, amounts to -0.6 eV per molecule. The other three models maintain the double-row pattern, with different orientation angles. Fine adjustments are observed, which improve the HB-contacts, which are in average less than two HBs per N_{CN}. As a consequence, the aggregation strength per molecule is also reduced.

Model-a has the lowest E_{mols} which is -0.42 eV/molecule among all the models considered. Model-c and model-d have E_{mols} as -0.52 and -0.56 eV/molecule, respectively. While there is no significant changes in coordinates with respect to initial positions of model-a and model-d, rotations of both first and second molecular rows are observed in optimized configurations of model-b and model-c. In model-a, the shortest N_{CN}-N_{CN} and N_{CN}-H atom pairs of neighboring molecules become 4.24 Å and 2.40 Å. Neighboring Co-Co distances relax and minimum and maximum distances become 13.15 Å and 13.29 Å, respectively, which are initially set to 12.77 Å.

In model-b, effects of dipole-dipole and hydrogen bonding interactions are investigated by setting the neighboring N_{CN}-N_{CN} and N_{CN}-H distances to 2.56 Å and 1.95 Å, respectively. However these initial distances are very short, especially for N_{CN}-N_{CN}, so repulsive interactions play crucial role which result in rotations of the molecular rows. As a result optimized N_{CN}-N_{CN} and N_{CN}-H distances become 6.0 Å and 2.34 Å, respectively.

Model-c is designed to maximize interactions of the network with the surface, since monomer adsorption results show that CoPyr prefers to adsorb with 60° (or 120°) alignment. However having 1.51 Å of N_{CN}-H is very short, so that repulsive interactions separate molecules from each other and relax the N_{CN}-H distance to 2.36 Å. Finally in model-d, one of the N_{CN}-H distance relaxes to 2.45 Å from 2.11 Å. Since the shortest N_{CN}-N_{CN} distance is 5.69 Å, we do not observe rotations of the molecules due to the N_{CN}-N_{CN} lone pair repulsion.

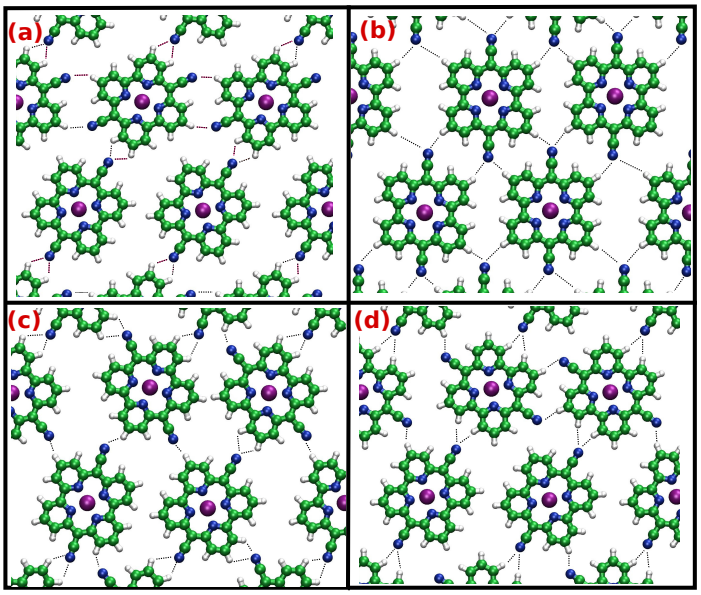

Figure 6.9: Optimized structures of four different CoPyr configurations, namely model-a (a), model-b (b), model-c (c), and model-d (d), in gas phase. Molecules in neighboring cells are also depicted to clarify inter molecular interactions. Dashed lines indicate hydrogen bonds between N_{CN} atoms and neighboring molecules. For color code, see previous figures.

CoPyr Monolayer on Au(111)

The structures adsorbed on the slab are shown in Figure 6.10. The optimization of the adsorbed monolayer turns out to produce very similar structures, as those obtained in vacuum. Table 6.3 shows minimum distances of neighboring N_{CN}-N_{CN} ($d^{min}_{N_{CN}\text{-}N_{CN}}$) and N_{CN}-H ($d^{min}_{N_{CN}\text{-}H}$) atom pairs after geometry optimization both in gas phase and also on surface for all the models. While in models a and b we do not observe significant changes with respect to gas phase and adsorbed coordinates of the atoms, in models c and d adsorbed CoPyr network shows shifting from gas phase coordinates due to presence of the Au slab. In model-c the two molecules in the second row are rotated at 100° and 120°. Co atoms diffuses on the surface to maximize the interactions with the underneath Au atoms. On the other hand, N_{CN} atoms rotate on the surface to keep Co metal center in Pyr core stable, maximize hydrogen bonding, and increase interactions with the slab.

Structural parameters characterizing four distinct monolayer configurations are reported in Table 6.4. As it is shown in Figure 6.10, in models-a, c, and d, molecule 1 is still at 60° and well positioned with N_{CN} and Co at atop sites, whereas the others are less effectively binding to the surface. The average adsorption energy, as reported

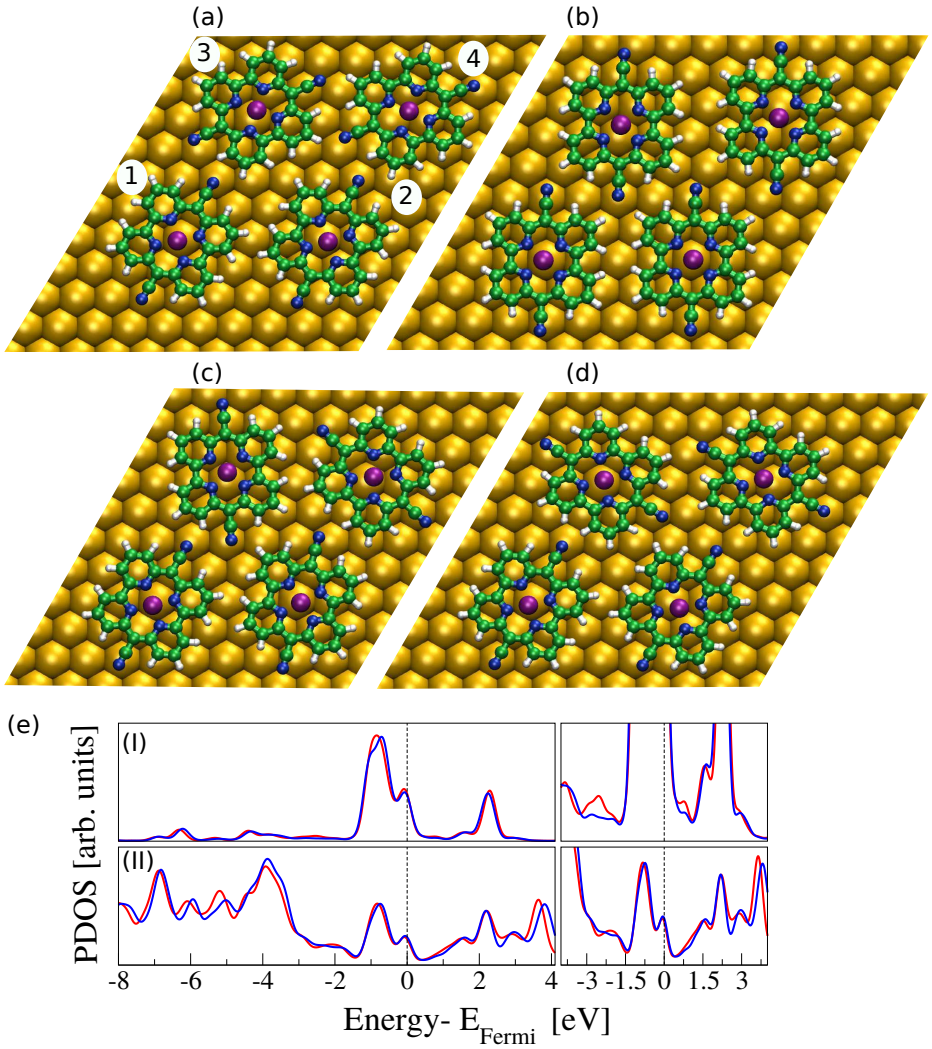

Figure 6.10: Optimised CoPyr monolayer adsorbed on the ideal Au(111) surface. The four structures refer to the model-a (a), model-b (b), model-c (c), and model-d (d) (see text). The molecules are labeled from 1 to 4, forming two rows along the $[1\bar{1}0]$ direction, as shown in (a). The colour code is the same used in previous figures. e) PDOS on molecule 1 (red) and 4 (blue) of model-a. The top panels (I) display the Co(3d)-PDOS. The bottom panels (II) display the total CoPyr-PDOS. The PDOS are normalised dividing by the number of considered atoms. The right panels are magnified views of the ±4 eV interval around the Fermi energy.

in Table 6.5, is around -4 eV/mol for all four models. The molecule/metal interaction, $E_{\text{int}}^{\text{monolayer}}$, is weaker than for the isolated monomer, because by assembling the optimal registry conditions are overruled. The attractive intermolecular interactions and the vdW term guarantee anyway the stabilization of the monolayer. Model-a

Table 6.3: Optimized intermolecular distances both in gas phase and on ideal Au surface for all models. All distances are given in Å.

Model	Environment	$d^{\min}_{\mathrm{N_{CN}\text{-}N_{CN}}}$	$d^{\min}_{\mathrm{N_{CN}\text{-}H}}$
a	Gas Phase	4.24	2.40
	Surface	3.93	2.32
b	Gas Phase	6.00	2.34
	Surface	5.83	2.32
c	Gas Phase	3.80	2.36
	Surface	3.88	2.28
d	Gas Phase	5.69	2.45
	Surface	5.21	2.25

is characterized by the strongest $E^{\mathrm{monolayer}}_{\mathrm{int}}$, thanks to the rather favorable registry of molecule 1 and 2 determining the smallest average N_{CN}-Au distance. However, E_{ads} is slightly more positive, because of the less attractive molecule/molecule interactions, due to the reduced number of intermolecular HBs. In model-b, all molecules are equally oriented at 90°, and none is placed with an optimal atop registry of both the N_{CN} atoms. However, the Co-Au distances are short, which strengthen the binding, making this the most stable assembly.

Table 6.4: Structural parameters characterizing the four distinct monolayer configurations. $d^{\min}_{\mathrm{Co\text{-}Au}}$ and $d^{\mathrm{avg}}_{\mathrm{Co\text{-}Au}}$ are minimum and average Co-Au distances, respectively; $h^{\mathrm{avg}}_{\mathrm{Au}}$ is average vertical position change of Au atom which is the closest one to Co center; $d^{\min}_{\mathrm{N_{CN}\text{-}Au}}$ and $d^{\max}_{\mathrm{N_{CN}\text{-}Au}}$ are minimum and average N_{CN}-Au distances, respectively; $d^{\mathrm{avg}}_{\mathrm{N_{CN}}}$ is average N_{CN}-N_{CN} distance of a molecule after adsorption showing degree of bending of CoPyr towards the Au surface. All the distances are given in Å.

Model	$d^{\min}_{\mathrm{Co\text{-}Au}}$	$d^{\mathrm{avg}}_{\mathrm{Co\text{-}Au}}$	$h^{\mathrm{avg}}_{\mathrm{Au}}$	$d^{\min}_{\mathrm{N_{CN}\text{-}Au}}$	$d^{\mathrm{avg}}_{\mathrm{N_{CN}\text{-}Au}}$	$d^{\mathrm{avg}}_{\mathrm{N_{CN}}}$
a	2.80	2.96	0.16	2.61	3.03	11.73
b	2.76	2.85	0.21	3.05	3.24	11.76
c	2.79	2.88	0.21	2.64	3.17	11.74
d	2.78	2.87	0.20	2.94	3.19	11.76

The PDOS computed for molecule 1 and 4 of the optimized model-a are compared in Figure 6.10(e) to verify the effects on the electronic distribution as a function of the

Table 6.5: Adsorption, interaction, dispersion, and distortion energies characterizing the four models of the CoPyr monolayer adsorbed on Au(111). Energies are in eV/molecule.

Model	E_{ads}	$E_{\mathrm{int}}^{\mathrm{monolayer}}$	$E_{\mathrm{dist}}^{\mathrm{monolayer}}$	$E_{\mathrm{ads}}^{\mathrm{disp}}$
a	-3.98	-4.12	0.49	-3.93
b	-4.11	-4.10	0.52	-3.87
c	-4.02	-3.95	0.37	-3.90
d	-4.06	-3.91	0.33	-3.87

registry within the monolayer. Indeed, these two molecules are apparently the ones with the best and the worst adsorption registry. In particular, the shortest Co(II)-Au distances are 2.80 Å and 3.31 Å, respectively. As expected, the Co(3d)-PDOS shows some differences between the two molecules around the Fermi energy. The increased density of Co(3d) states at about -2.5 eV and at about +1 eV is specific of the molecule that is more strongly binding to Au. This confirms that the heterogeneous Co environment within the monolayer results in clear electronic signatures, which might also explain the experimentally observed shift of the Co XPS signals.

6.2.3 The Metalation Process

The metalation process has a stabilisation effect on the monolayer, thanks to the interaction of Co with Au. This introduces additional constraints to the position and orientation of the molecules, which are supposed to be the reason of the experimentally observed reconstruction of the molecular lattice. However, the metalation itself is not as straightforward as expected. Upon the post-deposition of atomic Co, on top of the already formed Pyr-monolayer, only a fraction of molecules is metalated and most of the metalated molecules appear to be trapped in some intermediate state, whereas most of the Co is adsorbed in clusters on the Au(111) surface. Only after a prolongated annealing at 423 K, ≈90% of the molecular lattice are CoPyr complexes with Co atoms occupying the central, four-fold nitrogen coordinated site. This behavior is at odds with the fast metalation of porphyrins on metallic substrates [171].

In order to shed some light on the reaction mechanism, and to identify the intermediate states that might hinder the direct formation of CoPyr, we simulate the process by AIMD. In particular, one Co atom is placed above the monolayer, as in the first stage of the deposition, and the system is thermalized at 350 K.

First the Pyr-monolayer has been shortly equilibrated at room temperature, starting from a (25°– 60°) configuration, in analogy with the model-a used for the CoPyr-monolayer. The molecules turn out to be quite mobile at this temperature, and wobble over the surface, forming and breaking N_{CN}-Au and N_{CN}-H contacts, while their orientation keeps changing. Once the Co atom is added, in order to be able to observe the relevant processes within a relative short simulation time, the dynamics is accelerated by applying the metadynamics scheme. Two CVs are employed. CV1 keeps track of the coordination of Co with respect to any N atom present in the simulation cell. Its value is expected to increase from ∼0, when Co is far from any molecule, to ∼4, when it is inserted at the molecular center. CV2 follows the coordination in the molecular pocket between the N and H atoms. Using a cutoff radius of about 2.5 Å, the initial average coordination is about two. This value is expected to decrease, when the H atoms of one molecule are replaced by the Co atom. Though, since the average is taken over the four molecules and only one is going to be metalated, the final value is going to be larger than 1.5.

The run is started by positioning the Co atom above the monolayer at about 3 Å. During the first 18 ps, the Co atom coordinates to the center of one pyridine ring, at an average distance of about 2.6 Å from the closest N_p, with fluctuation of about 1 Å. The coordination number varies between 1 and 2, being the next closest N_p between 4 and 4.8 Å, i.e., in the outer part of the coordination sphere. This state represents a stable intermediate and, indeed, it can be obtained as stable structure by the geometry optimization carried out from one MD snapshot extracted from the trajectory at about 15 ps (Figure 6.11(a) and (b)). We infer that this intermediate acts as a bottleneck along the metalation process. This state is stabilized by the overlap between the p orbitals of the six-member ring and the d orbitals of the Co metal. The simulated STM image of the optimized intermediate in Figure 6.11(c) shows a bright protrusion at the position of the coordinated Co atom. As discussed in our recent work [71], we know that the presence of an intermediate state can be defined by these bright protrusions in STM images that are differ from the signature of the Pyr an is in agreement with the experimental images taken ahead of full metalation upon deposition of Co, showing features that differ from the signature of the Pyr and CoPyr [71]. Therefore, STM image in Figure 6.11(c) can be interpreted as an intermediate state, the presence of distorted Pyr molecules interacting with the deposited Co atoms.

The evolution of the two CVs along the MTD trajectory is reported in Figure 6.12(a). The large fluctuations of CV1 are determined by the strong distortion of the molecule,

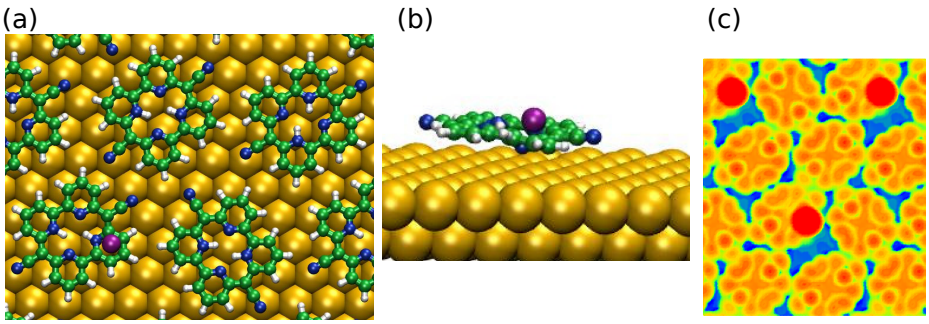

Figure 6.11: (a) Geometry optimization of one MD snapshot extracted from the trajectory at around 15 ps. Co is at the center of one of the pyridine ring and spends more time on the ring instead of quickly coordinating with the Pyr core. While top view is shown in (a), side view of the optimized structure is shown in (b). For clarity only one Pyr molecule with Co ontop is shown in (b). This structure is determined to be intermediate state and acts as a bottleneck along the metalation process. The color code is the same used in previous figures. (c) Simulated STM of the optimized intermediate state. The image has been generated with a bias potential of -1.0 eV, setting the iso-density surface to a value of 10^{-5} e/Å^3. The color scale from blue to red spans a height change of 3.5 Å.

while the Co atom is coordinating with the pyridine ring. The CV1 value is directly related to the distance of Co from the closest N atoms, i.e., the closest N_p, the next N_p, and the closest N_{CN} of the same molecule, which are plotted in Figure 6.12(b).

During the first 20 ps, the CV1's value increases beyond 2, when the closest cyano group flips upwards, such that the N_{CN} also coordinates to Co. These rearrangements are associated with a significant molecular distortion, as also verified by the fluctuation in the N_{CN}-N_{CN} distance, in Figure 6.12(c). However, the definitive increase in coordination occurs between 23 and 24 ps, when the Co atom moves away from the pyridine ring, towards the molecular center. The four Co-N_p become all equal ∼2 Å, while the Co-N_{CN} increases to ∼6 Å. The Co insertion pushes away the H atoms at the center of the molecule, thus determining the decrease in the CV2's value. For the rest of the simulation, the removed hydrogens are adsorbed at the gold surface. Over a sufficiently long time scale, the H diffuse over the surface, recombine and desorb as molecular hydrogen. After the replacement has taken place, the molecule recovers its basically planar geometry. The N_{CN}-N_{CN} distance gets the characteristic shorter length of CoPyr, and the Co-N distances show much smaller fluctuations. The molecule rotates and slides on the surface, until the Co atom is located approximately atop one surface Au atom. The top view of four snapshots extracted from the tra-

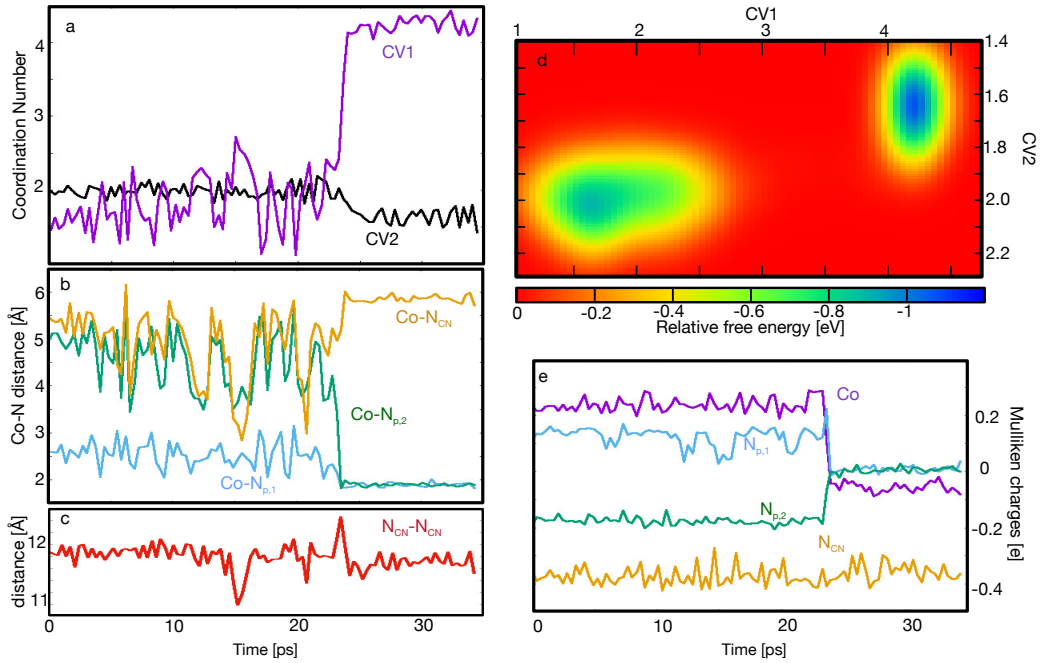

Figure 6.12: (a) Time evolution of CV1 and CV2 along the MTD run. (b) Distance between the Co atom and some close N atoms: the closest N_p (labeled as Co–$N_{p,1}$) , the next N_p (Co–$N_{p,2}$), and the closest N_{CN} (Co–N_{CN}) of the same molecule. (c) N_{CN}–N_{CN} distance in the molecule interacting with Co. (d) Free energy surface as function of the two CVs, as determined from the MTD potential added during the 35 ps run. (e) Mulliken charges of Co, N_{CN}, $N_{p,1}$, and $N_{p,2}$.

jectory at the beginning and after 20, 23, and 35 ps are displayed in Figure 6.13. From the last snapshot the reorientation of the molecule induced by the metalation can be clearly observed. After about 35 ps, the process can be considered completed and the MTD simulation has been interrupted. A further prolongation should lead also to the reverse process, thus providing a better estimate of the depth of the free energy minimum corresponding to the metalated state. However, it would require significantly larger computational resources. Even if the constructed free energy surface, reported in Figure 6.12(d), underestimates the difference between the two end states, it clearly shows the presence of the stable intermediate. The basin of attraction of the intermediate is broader than the one of the final state, indicating a larger flexibility of the molecular structure. The barrier separating the intermediate from the metalated state turns out to be around 1.0 eV. The metalation process is also accompanied by the electronic redistribution within the molecule. In Figure 6.12(e), we report the Mulliken charges calculated for the Co atom and three N atoms. These

are the closest N_p, bound to one central H at the beginning of the simulation, the N_p next to it, with no H, and the closest N_{CN}. Despite the absolute value of the Mulliken charges is not an accurate indicator of the oxidation state, its variations characterize the structural changes, as it is the case for the charge of Co and of the two N_p that abruptly change upon Co insertion.

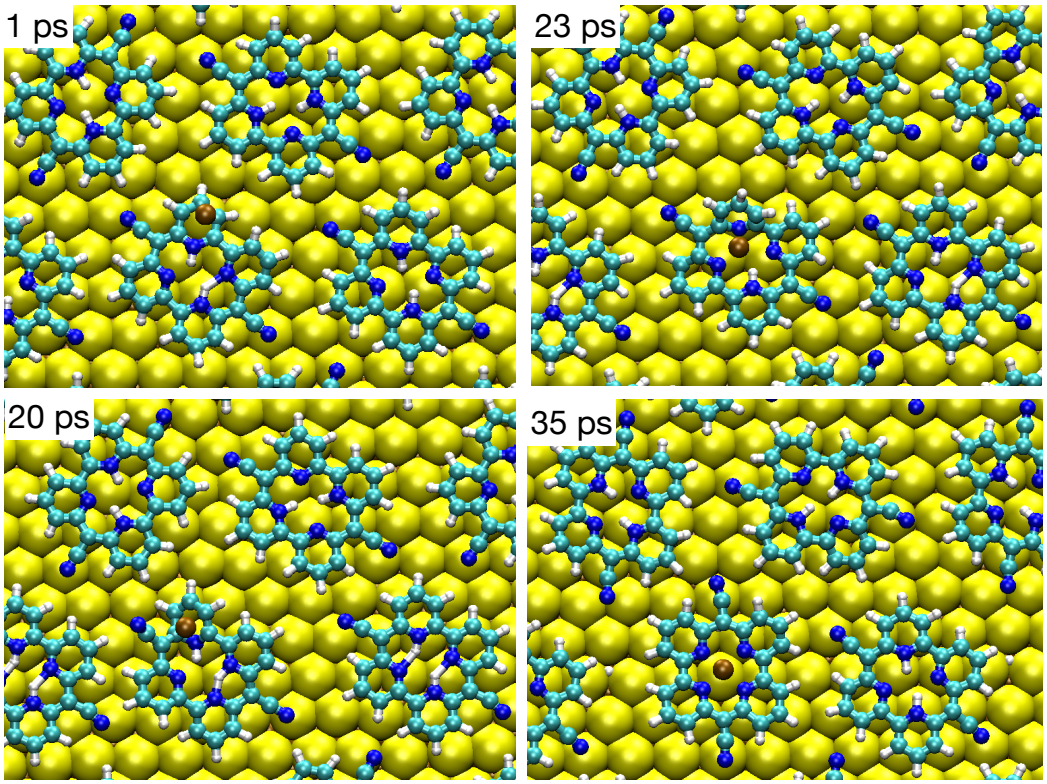

Figure 6.13: The top views of four snapshots extracted from the trajectory at the beginning and after 20, 23, and 35 ps during metalation process. Color code: cyan: C, white: H, brown: Co, blue: N, and yellow: Au.

These results confirm that the the metalation pathway upon Co deposition is not straightforward. The interaction with the pyridine rings, but also with the underlying Au(111) surface, compete with the insertion into the molecular center. Thanks to the wider exposed area, the intermediate states are entropically favored. From the pyridine-coordinated state, the Co atom could also be adsorbed to the Au(111) surface and the metalation could then occur from below. The investigation of this other possible pathway can be the subject of an extension of the present study. A new MTD run would be needed, starting with Co adsorbed on the surface and using a different set of collective variables. Moreover, once on the gold surface, Co can also aggregate into clusters, as shown from experiment, which could also be investigated

adding more Co atoms on the surface. Here we just compare the total potential energy of some foreseen intermediate states. We find that the coordination of Co to one pyridinic ring stabilizes the gas phase atom by 3.4 eV. The successive insertion of Co with the transfer of the two H atoms to the surface leads to a further decrese in potential energy of -3.9 eV, while the desorption of molecular hydrogen corresponds to an additional stabilization of 0.2 eV. By optimizing a state where the Co atom is co-adsorbed on Au(111), we find that one cyano N coordinates to the Co ad-atom and this stabilizes the i intermediate, which is indeed lower in energy with respect to the state with Co coordinated to the pyridine ring by 3.6 eV. We have previously evaluated the relative stability of Co in the different situations, comparing the co-adsorbed Co atom and the Pyr monomer on Au(111) to the metalated state. These data are discussed in our recent publication [71]. It turns out that separately co-adsorbed Co and Pyr on Au(111) (no interactions with the cyano group) is less stable by 1.3 eV than the formation of the CoPyr-2H complex, in which Co is inserted into the Pyr core from below, but the two hydrogens are still attached to the N_p atoms. Anyway, the intermediate state shown in Figure 6.11 (considering only the monomer) is also 0.9 eV less stable than separately co-adsorbed Co and Pyr on Au(111) complex, thus confirming that the Co-Au attractive interactions are stronger than the interactions between Co atom and pyridine ring. In general we can confidently state that the most stable state is, indeed, the CoPyr on Au(111) surface plus molecular hydrogen in the gas phase.

6.3 Conclusions

We have investigated the adsorption of Pyr and CoPyr monomers on the reconstructed Au(111) surface, by considering the role of the herringbone reconstruction and of the adsorption registry in determining the geometry and the electronic properties of the adsorbate. To this end, we have augmented the PBE energy functional with the dispersion correction approach that most accurately reproduce the characteristic corrugation pattern of the herringbone reconstruction, i.e., the rVV10 scheme. We have also verified that other schemes are not sensitive enough to the local environment geometry, as the Grimme-D3 correction, or are too weakly binding, as the DRSLL.

Our results indicate that the molecule/metal binding strength is maximized when the N_{CN} atoms and, if present, the Co center are located at atop sites. Over the fcc

domain, this condition is at best satisfied when the molecule is oriented with the cyano axis at 60° with respect to to the $[1\bar{1}0]$ crystallographic direction. Energetical and structural parameters, as well as the PDOS reveal that the herringbone reconstruction does not have a significant effect on molecule/metal interactions. On the other hand, comparing the adsorption of Co(II) center (for CoPyr) and/or N_{CN} on atop and bridge positions, we remark significant differences in energetical/structural parameters and also in the re-hybridization of the molecular orbitals. We conclude that the adsorption registry has an influence while the herringbone reconstruction does not.

Another important aspect is the aggregation of the molecules to form a monolayer. Starting from the experimental observation of the superstructure constituted by the CoPyr assembly, we could determine the most probable relative orientation of the molecules in the lattice and identify the relevant molecule/molecule interactions. In particular, we observe that the molecule rotate to avoid the repulsive cyano/cyano interactions, while tend to form weak N_{CN}-H bonds. The fact that the registry on the Au surface within the monolayer is not homogenous, induces the presence of differently adsorbed molecules in the assembly. This fact most probably determines the different electronic signatures revealed experimentally by XPS. Hence, the splitting of the core binding energy should be attributed to the local variation in the position of the Co center with respect to the closest underlying atom, and not to the location on a different region of the Au(111) reconstructed surface.

Recent experimental findings point out that contrary to traditional porphyrins which can be metalated even at room temperature, activation barrier for metalation of Pyr is rather high and the process is temperature driven [71]. The metalation process has been investigated by means of ab initio molecular dynamics. One Co atom deposited over the already formed Pyr monolayer at 350 K explores the available configurational space until it is inserted into one molecular pocket. The simulation show the presence of at least one intermediate state, where Co is coordinated to one pyridine ring. This hinders the move toward the molecular center and the replacement of the internal H atoms. The stabilization of this intermediate is attributed to the overlap between the p orbitals of the six-membered ring and the d orbitals of the Co metal.

The simulation of the metalation reaction by placing initially the Co atom from above, in the vicinity of the monolayer wants to reproduce the early stage of the process, soon after the deposition. However, the direct metalation might fail and the Co atoms can be transferred to the Au surface and aggregate into clusters. The

further metalation can then be activated by annealing, as it is indeed observed in experiment. A possible extension of this study should consider the second stage of the process, by simulating the diffusion of the Co atoms over the Au surface until they coordinate with one molecular center and replace the H atoms from below.

7 Conclusions

Emergent technologies and the demand for alternative energy sources which do not produce greenhouse gases as byproduct, lead to a growing awareness in using those renewable sources already provided by nature, such as sunlight. Generating renewable fuels by taking advantage of solar-light by storing its energy in chemical bonds has become the main challenge of today's energy science. Recently, researchers have become aware of the potential of photo-catalytic water splitting for sustainable production of molecular hydrogen, the latter representing an efficient carrier for energy storage and conversion into common liquid fuels. In this respect, Co-based poly-pyridyl complexes represent an efficient, robust, and promising water reduction catalysts towards H_2 production. Fast development in designing ligand environment around Co center yields in applicability of these catalysts both in homogeneous and heterogeneous environments. In particular, immersing Co-centered catalysts in water solution together with efficient photosensitizers or immobilizing these ligands on oxide and metal surfaces, and investigating their tunable electronic properties and H_2 production performances have gained significant attention in recent years.

Our research have been carried out under the URPP LightChEC program at the University of Zurich which promotes the close collaboration among theoretical and experimental scientists. Therefore, we always combine our theoretical simulations with experimental observations to explore the potentials, properties, and performances of H_2 production systems under consideration. In order to increase the accuracy of our electronic structure calculations, we use hybrid density functionals together with nonlocal van der Waals electron correlation. The dynamical properties, on the other hand, are obtained using ab-initio molecular dynamics and metadynamics rather than classical Newtonian dynamics. Thanks to the applied high level simulation techniques, our models explain the probable reasons of experimental findings rather good and predict the structures and properties which could not be resolved due to the insufficiency of the experimental techniques.

As already suggested by the discussions provided in each chapter our research can proceed in many directions. Concerning the homogeneous Co-based poly-pyridyl catalysts, the irreversible ligand switch occurring after the first electron injection might substantially change the H_2 production mechanism. Therefore, each catalytic cycle should be reconsidered and simulated for the catalyst that undergoes a ligand switch. Besides, how proton diffuses to the Co center and how the coordination sphere around Co affects this diffusion are still open questions that should be addressed. Regarding the Co complexes adsorbed on TiO_2 surface, a possible extension can be considering the co-adsorption of water and hydrogen on the oxide surface and possible reaction mechanisms leading to the production of molecular hydrogen. Furthermore, we expect that by functionalizing pyrphryin with different linkers a further tuning of the coupling with the oxide is possible and improved water splitting performance can be achieved. A possible extension of the catalyst immobilized on Au(111) surface should consider the another stage of the metalation process, by simulating the diffusion of the Co atoms over the Au surface until they coordinate with one molecular center and replace the H atoms from the below.

The results of this study together with the possible extensions provide a complete picture of the photo-catalytic H_2 production from homogeneous to heterogeneous environments. The presented work is a solid contribution to the literature filling many fundamental gaps. We hope that these results inspire many researchers to develop efficient and scalable H_2 production catalysts that benefit from solar-light.

Bibliography

[1] W. T. Eckenhoff, R. Eisenberg. Molecular systems for light driven hydrogen production. *Dalton Transactions* **2012**, *41*, 13004–13021.

[2] N. Armaroli, V. Balzani. The Future of Energy Supply: Challenges and Opportunities. *Angewandte Chemie International Edition* **2007**, *46*, 52–66.

[3] M. Carmo, D. L. Fritz, J. Mergel, D. Stolten. A comprehensive review on PEM water electrolysis. *International Journal of Hydrogen Energy* **2013**, *38*, 4901–4934.

[4] T. L. LeValley, A. R. Richard, M. Fan. The progress in water gas shift and steam reforming hydrogen production technologies – A review. *International Journal of Hydrogen Energy* **2014**, *39*, 16983–17000.

[5] E. Seker. The catalytic reforming of bio-ethanol over SiO_2 supported ZnO catalysts: The role of ZnO loading and the steam reforming of acetaldehyde. *International Journal of Hydrogen Energy* **2008**, *33*, 2044–2052.

[6] A. T. Ashcroft, A. K. Cheetham, J. S. Foord, M. L. H. Green, C. P. Grey, A. J. Murrell, P. D. F. Vernon. Selective oxidation of methane to synthesis gas using transition metal catalysts. *Nature* **1990**, *344*, 319–321.

[7] S. G. Avcioglu, E. Ozgur, I. Eroglu, M. Yucel, U. Gunduz. Biohydrogen production in an outdoor panel photobioreactor on dark fermentation effluent of molasses. *International Journal of Hydrogen Energy* **2011**, *36*, 11360–11368.

[8] H. Junge, Z. Codolà, A. Kammer, N. Rockstroh, M. Karnahl, S.-P. Luo, M.-M. Pohl, J. Radnik, S. Gatla, S. Wohlrab, J. Lloret, M. Costas, M. Beller. Copper-based water reduction catalysts for efficient light-driven hydrogen generation. *Journal of Molecular Catalysis A: Chemical* **2014**, *395*, 449–456.

[9] M. Wang, Y. Na, M. Gorlov, L. Sun. Light-driven hydrogen production catalysed by transition metal complexes in homogeneous systems. *Dalton Transactions* **2009**, p. 6458–6467.

[10] A. J. Esswein, D. G. Nocera. Hydrogen Production by Molecular Photocatalysis. *Chemical Reviews* **2007**, *107*, 4022–4047.

[11] S. Losse, J. G. Vos, S. Rau. Catalytic hydrogen production at cobalt centres. *Coordination Chemistry Reviews* **2010**, *254*, 2492–2504.

[12] C. H. Lee, D. K. Dogutan, D. G. Nocera. Hydrogen Generation by Hangman Metalloporphyrins. *Journal of the American Chemical Society* **2011**, *133*, 8775–8777.

[13] A. Bhattacharjee, E. S. Andreiadis, M. Chavarot-Kerlidou, M. Fontecave, M. J. Field, V. Artero. A Computational Study of the Mechanism of Hydrogen Evolution by Cobalt(Diimine-Dioxime) Catalysts. *Chemistry–A European Journal* **2013**, *19*, 15166–15174.

[14] E. Joliat, S. Schnidrig, B. Probst, C. Bachmann, B. Spingler, K. K. Baldridge, F. von Rohr, A. Schilling, R. Alberto. Cobalt complexes of tetradentate, bipyridine-based macrocycles: their structures, properties and photocatalytic proton reduction. *Dalton Transactions* **2016**, *45*, 1737–1745.

[15] M. Guttentag, A. Rodenberg, R. Kopelent, B. Probst, C. Buchwalder, M. Brandstätter, P. Hamm, R. Alberto. Photocatalytic H_2 Production with a Rhenium/Cobalt System in Water under Acidic Conditions. *European Journal of Inorganic Chemistry* **2012**, *2012*, 59–64.

[16] X. Hu, B. S. Brunschwig, J. C. Peters. Electrocatalytic Hydrogen Evolution at Low Overpotentials by Cobalt Macrocyclic Glyoxime and Tetraimine Complexes. *Journal of the American Chemical Society* **2007**, *129*, 8988–8998.

[17] B. H. Solis, A. G. Maher, T. Honda, D. C. Powers, D. G. Nocera, S. Hammes-Schiffer. Theoretical Analysis of Cobalt Hangman Porphyrins: Ligand Dearomatization and Mechanistic Implications for Hydrogen Evolution. *American Chemical Society Catalysis* **2014**, *4*, 4516–4526.

[18] S. Soman. Molecular Systems for Solar H2: Path to a Renewable Future. *Comments on Inorganic Chemistry* **2015**, *35*, 82–120.

[19] Z. Han, R. Eisenberg. Fuel from Water: The Photochemical Generation of Hydrogen from Water. *Accounts of Chemical Research* **2014**, *47*, 2537–2544.

[20] S. Berardi, S. Drouet, L. Francas, C. Gimbert-Surinach, M. Guttentag, C. Richmond, T. Stoll, A. Llobet. Molecular artificial photosynthesis. *Chemcal Society Reviews* **2014**, *43*, 7501–7519.

[21] A. Rodenberg, M. Orazietti, B. Probst, C. Bachmann, R. Alberto, K. K. Baldridge, P. Hamm. Mechanism of Photocatalytic Hydrogen Generation by a Polypyridyl-Based Cobalt Catalyst in Aqueous Solution. *Inorganic Chemistry* **2015**, *54*, 646–657.

[22] Y. Sun, J. P. Bigi, N. A. Piro, M. L. Tang, J. R. Long, C. J. Chang. Molecular cobalt pentapyridine catalysts for generating hydrogen from water. *Journal of the American Chemical Society* **2011**, *133*, 9212–9215.

[23] C. F. Leung, S. M. Ng, C. C. Ko, W. L. Man, J. Wu, L. Chen, T. C. Lau. A cobalt(ii) quaterpyridine complex as a visible light-driven catalyst for both water oxidation and reduction. *Energy and Environmental Science* **2012**, *5*, 7903–7907.

[24] C. Bachmann, M. Guttentag, B. Spingler, R. Alberto. 3d element complexes of pentadentate bipyridine-pyridine-based ligand scaffolds: Structures and photocatalytic activities. *Inorganic Chemistry* **2013**, *52*, 6055–6061.

[25] B. Probst, M. Guttentag, A. Rodenberg, P. Hamm, R. Alberto. Photocatalytic H_2 production from water with rhenium and cobalt complexes. *Inorganic Chemistry* **2011**, *50*, 3404–3412.

[26] M. Guttentag, A. Rodenberg, C. Bachmann, A. Senn, P. Hamm, R. Alberto. A highly stable polypyridyl-based cobalt catalyst for homo- and heterogeneous photocatalytic water reduction. *Dalton Transactions* **2013**, *42*, 334–337.

[27] R. S. Khnayzer, V. S. Thoi, M. Nippe, A. E. King, J. W. Jurss, K. A. El Roz, J. R. Long, C. J. Chang, F. N. Castellano. Towards a comprehensive understanding of visible-light photogeneration of hydrogen from water using cobalt(ii) polypyridyl catalysts. *Energy and Environmental Science* **2014**, *7*, 1477–1488.

[28] C. Kutal. Photochemical conversion and storage of solar energy. *Journal of Chemical Education* **1983**, *60*, 882–887.

[29] C. G. Garcia, J. F. de Lima, N. Y. M. Iha. Energy conversion: From the ligand field photochemistry to solar cells. *Coordination Chemistry Reviews* **2000**, *196*, 219–247.

[30] C. F. Goodeve, J. A. Kitchener. The mechanism of photosensitisation by solids. *Transactions of the Faraday Society* **1938**, *34*, 902–908.

[31] A. Fujishima, K. Honda. Electrochemical photolysis of water at a semiconductor electrode. *Nature* **1972**, *238*, 37–38.

[32] S. Fujiyoshi, T.-A. Ishibashi, H. Onishi. Fourth-order raman spectroscopy of wide-band gap materials. *The Journal of Physical Chemistry B* **2005**, *109*, 8557–8561.

[33] M. Iman-Amir, N. Julkapli, S. Bagheri, A. T. Yousefi. TiO_2 hybrid photocatalytic systems: Impact of adsorption and photocatalytic performance. *Reviews in Inorganic Chemistry* **2015**, *35*, 151–178.

[34] L.-L. Li, E. W.-G. Diau. Porphyrin-sensitized solar cells. *Chemical Society Reviews* **2013**, *42*, 291–304.

[35] M. Ni, M. K. Leung, D. Y. Leung, K. Sumathy. A review and recent developments in photocatalytic water-splitting using for hydrogen production. *Renewable and Sustainable Energy Reviews* **2007**, *11*, 401–425.

[36] H. Imahori, S. Kang, H. Hayashi, M. Haruta, H. Kurata, S. Isoda, S. E. Canton, Y. Infahsaeng, A. Kathiravan, T. Pascher, P. Chábera, A. P. Yartsev, V. Sundström. Photoinduced Charge Carrier Dynamics of Zn–Porphyrin–TiO_2 Electrodes: The Key Role of Charge Recombination for Solar Cell Performance. *The Journal of Physical Chemistry A* **2011**, *115*, 3679–3690.

[37] A. L. Linsebigler, G. Lu, J. T. Yates. Photocatalysis on TiO_2 surfaces: Principles, mechanisms, and selected results. *Chemical Reviews* **1995**, *95*, 735–758.

[38] A. J. Bard, M. A. Fox. Artificial photosynthesis: Solar splitting of water to hydrogen and oxygen. *Accounts of Chemical Research* **1995**, *28*, 141–145.

[39] O. Bikondoa, C. L. Pang, R. Ithnin, C. A. Muryn, H. Onishi, G. Thornton. Direct visualization of defect-mediated dissociation of water on TiO_2(110). *Nature Materials* **2006**, *5*, 189–192.

[40] S. Wendt, J. Matthiesen, R. Schaub, E. K. Vestergaard, E. Lægsgaard, F. Besenbacher, B. Hammer. Formation and splitting of paired hydroxyl groups on reduced TiO_2(110). *Physical Review Letters* **2006**, *96*, 66107–66110.

[41] Z. Y. Zhao. Single Water Molecule Adsorption and Decomposition on the Low-Index Stoichiometric Rutile TiO_2 Surfaces. *The Journal of Physical Chemistry C* **2014**, *118*, 4287–4295.

[42] K. R. Hahn, A. Tricoli, G. Santarossa, A. Vargas, A. Baiker. First Principles Analysis of H_2O Adsorption on the (110) Surfaces of SnO_2, TiO_2 and Their Solid Solutions. *Langmuir* **2012**, *28*, 1646–1656.

[43] D. A. H. Hanaor, M. H. N. Assadi, S. Li, A. Yu, C. C. Sorrell. Ab initio study of phase stability in doped TiO_2. *Computational Mechanics* **2012**, *50*, 185–194.

[44] Y. Zhang, D. S. Kilin. Computational modeling of wet TiO_2 (001) anatase surfaces functionalized by transition metal doping. *International Journal of Quantum Chemistry* **2012**, *112*, 3867–3873.

[45] S.-T. Zhang, C.-M. Li, H. Yan, M. Wei, D. G. Evans, X. Duan. Density functional theory study on the metal-support interaction between Ru cluster and anatase TiO_2(101) surface. *The Journal of Physical Chemistry C* **2014**, *118*, 3514–3522.

[46] J. Graciani, J. J. Plata, J. F. Sanz, P. Liu, J. A. Rodriguez. A theoretical insight into the catalytic effect of a mixed-metal oxide at the nanometer level: The case of the highly active metal/CeO_x/TiO_2(110) catalysts. *The Journal of Chemical Physics* **2010**, *132*, 104703–104710.

[47] M. Pastore, F. De Angelis. First-principles modeling of a dye-sensitized TiO_2/IrO_2 photoanode for water oxidation. *Journal of the American Chemical Society* **2015**, *137*, 5798–5809.

[48] F. Lakadamyali, E. Reisner. Photocatalytic H_2 evolution from neutral water with a molecular cobalt catalyst on a dye-sensitised TiO_2 nanoparticle. *Chemical Communications* **2011**, *47*, 1695–1697.

[49] M. Yin, S. Ma, C. Wu, Y. Fan. A noble-metal-free photocatalytic hydrogen production system based on Cobalt(III) complex and eosin Y-sensitized TiO_2. *The Royal Society of Chemistry Advances* **2015**, *5*, 1852–1858.

[50] F. Lakadamyali, A. Reynal, M. Kato, J. R. Durrant, E. Reisner. Electron Transfer in Dye-Sensitised Semiconductors Modified with Molecular Cobalt Catalysts: Photoreduction of Aqueous Protons. *Chemistry – A European Journal* **2012**, *18*, 15464–15475.

[51] D. Achey, S. Ardo, G. J. Meyer. Increase in the Coordination Number of a Cobalt Porphyrin after Photo-Induced Interfacial Electron Transfer into Nanocrystalline TiO_2. *Inorganic Chemistry* **2012**, *51*, 9865–9872.

[52] A. Monti, J. M. de Ruiter, H. J. M. de Groot, F. Buda. A dynamic view of proton-coupled electron transfer in photocatalytic water splitting. *The Journal of Physical Chemistry C* **2016**, *120*, 23074–23082.

[53] R. L. Milot, G. F. Moore, R. H. Crabtree, G. W. Brudvig, C. A. Schmuttenmaer. Electron Injection Dynamics from Photoexcited Porphyrin Dyes into SnO_2 and TiO_2 Nanoparticles. *The Journal of Physical Chemistry C* **2013**, *117*, 21662–21670.

[54] S. Ogawa, R. Narushima, Y. Arai. Aza Macrocycle that selectively binds lithium ion with color change. *Journal of the American Chemical Society* **1984**, *106*, 5760–5762.

[55] S. Ogawa, T. Uchida, T. Uchiya, T. Hirano, M. Saburi, Y. Uchidac. Lithium complexation of configurational isomers of tetra-aza macrocycle containing 2,2[prime or minute]-bipyridine. X-Ray molecular structure of the trans-isomer of a dibutyl dicyano macrocycle. *Journal Chemical Society, Perkin Transactions 1* **1990**, p. 1649–1653.

[56] C. Pierre, J.-M. Vincent, J.-B. Verlhac, C. Courseille, A. Dautant, C. Mathoniere. First synthesis and crystal structure of a Mn3+ complex derived from the Ogawa porphyrin-like ligand. *New Journal of Chemistry* **2001**, *25*, 522–524.

[57] Z. Zhu, K. Takano, A. Furuhama, S. Ogawa, S. Tsuchiya. Theoretical Study of Geometries and Electronic Transition of Color-Switching Molecules: Tetra-Aza Macrocycle and Its Zinc Complexes. *Bulletin of the Chemical Society of Japan* **2007**, *80*, 686–693.

[58] R. Ibrahim, S. Tsuchiya, S. Ogawa. A Color-Switching Molecule: Specific Properties of New Tetraaza Macrocycle Zinc Complex with a Facile Hydrogen Atom. *Journal of the American Chemical Society* **2000**, *122*, 12174–12185.

[59] J. M. Gottfried. Surface chemistry of porphyrins and phthalocyanines . *Surface Science Reports* **2015**, *70*, 259–379.

[60] L. A. Fendt, M. Stöhr, N. Wintjes, M. Enache, T. A. Jung, F. Diederich. Modification of supramolecular binding motifs induced by substrate registry: Formation of self-assembled macrocycles and chain-like patterns. *Chemistry–A European Journal* **2009**, *15*, 11139–11150.

[61] Auwärter Willi, Ecija David, Klappenberger Florian, Barth Johannes V. Porphyrins at interfaces. *Nature Chemistry* **2015**, *7*, 105–120.

[62] T. Yokoyama, S. Yokoyama, T. Kamikado, Y. Okuno, S. Mashiko. Selective assembly on a surface of supramolecular aggregates with controlled size and shape. *Nature* **2001**, *413*, 619–621.

[63] Y. Li, J. Xiao, T. E. Shubina, M. Chen, Z. Shi, M. Schmid, H.-P. SteinrÃ¼ck, J. M. Gottfried, N. Lin. Coordination and Metalation Bifunctionality of Cu with 5,10,15,20-Tetra(4-pyridyl)porphyrin: Toward a Mixed-Valence Two-Dimensional Coordination Network. *Journal of the American Chemical Society* **2012**, *134*, 6401–6408.

[64] J. Mielke, F. Hanke, M. V. Peters, S. Hecht, M. Persson, L. Grill. Adatoms underneath Single Porphyrin Molecules on Au(111). *Journal of the American Chemical Society* **2015**, *137*, 1844–1849.

[65] B. Hulsken, R. V. Hameren, J. W. Gerritsen, T. Khoury, P. Thordarson, M. J. Crossley, A. E. Rowan, R. J. M. Nolte, J. A. A. W. Elemans, S. Speller. Real-time single-molecule imaging of oxidation catalysis at a liquid-solid interface. *Nature Nanotechnology* **2007**, *2*, 285–289.

[66] H. Lv, Z. Xi, Z. Chen, S. Guo, Y. Yu, W. Zhu, Q. Li, X. Zhang, M. Pan, G. Lu, S. Mu, S. Sun. A New Core/Shell NiAu/Au Nanoparticle Catalyst with Pt-like Activity for Hydrogen Evolution Reaction. *Journal of the American Chemical Society* **2015**, *137*, 5859–5862.

[67] J. V. Barth, H. Brune, G. Ertl, R. J. Behm. Scanning tunneling microscopy observations on the reconstructed au(111) surface: Atomic structure, long-range superstructure, rotational domains, and surface defects. *Physical Review B* **1990**, *42*, 9307–9318.

[68] M. Graf, G. Mette, D. Leuenberger, Y. Gurdal, M. Iannuzzi, W.-D. Zabka, S. Schnidrig, B. Probst, J. Hutter, R. Alberto, J. Osterwalder. The impact of metalation on adsorption geometry, electronic level alignment and UV-stability of organic macrocycles on TiO_2(110). *Nanoscale* **2017**, *9*, 8756–8763.

[69] U. Diebold, J. Lehman, T. Mahmoud, M. Kuhn, G. Leonardelli, W. Hebenstreit, M. Schmid, P. Varga. Intrinsic defects on a TiO_2(110)(1×1) surface and their reaction with oxygen: A scanning tunneling microscopy study. *Surface Science* **1998**, *411*, 137–153.

[70] C. Wang, Q. Fan, Y. Han, J. I. Martinez, J. A. Martin-Gago, W. Wang, H. Ju, J. M. Gottfried, J. Zhu. Metalation of tetraphenylporphyrin with nickel on a TiO_2(110)-1×2 surface. *Nanoscale* **2016**, *8*, 1123–1132.

[71] G. Mette, D. Sutter, Y. Gurdal, S. Schnidrig, B. Probst, M. Iannuzzi, J. Hutter, R. Alberto, J. Osterwalder. From porphyrins to pyrphyrins: Adsorption study and metalation of a molecular catalyst on Au(111). *Nanoscale* **2016**, *8*, 7958–7968.

[72] F. Buchner, V. Schwald, K. Comanici, H.-P. SteinrÃ¼ck, H. Marbach. Microscopic evidence of the metalation of a free-base porphyrin monolayer with iron. *Chemical Physics and Physical Chemistry* **2007**, *8*, 241–243.

[73] P. Hohenberg, W. Kohn. Inhomogeneous electron gas. *Physical Review* **1964**, *136*, B864–B871.

[74] W. Kohn, L. J. Sham. Self-consistent equations including exchange and correlation effects. *Physical Review* **1965**, *140*, A1133–A1138.

[75] P. Giannozzi, S. Baroni, N. Bonini, M. Calandra, R. Car, C. Cavazzoni, D. Ceresoli, G. L. Chiarotti, M. Cococcioni, I. Dabo, A. D. Corso, S. de Gironcoli, S. Fabris, G. Fratesi, R. Gebauer, U. Gerstmann, C. Gougoussis, A. Kokalj, M. Lazzeri, L. Martin-Samos, N. Marzari, F. Mauri, R. Mazzarello, S. Paolini, A. Pasquarello, L. Paulatto, C. Sbraccia, S. Scandolo, G. Sclauzero, A. P. Seitsonen, A. Smogunov, P. Umari, R. M. Wentzcovitch. Quantum espresso: a modular and open-source software project for quantum simulations of materials. *Journal of Physics: Condensed Matter* **2009**, *21*, 395502–395520.

[76] G. Lippert, J. Hutter, M. Parrinello. A hybrid gaussian and plane wave density functional scheme. *Molecular Physics* **1997**, *92*, 477–488.

[77] M. Iannuzzi, J. Hutter. Comparative study of the nature of chemical bonding of corrugated graphene on Ru(0001) and Rh(111) by electronic structure calculations. *Surface Science* **2011**, *605*, 1360–1368.

[78] A. D. Becke. A new mixing of hartree-fock and local density-functional theories. *The Journal of Chemical Physics* **1993**, *98*, 1372–1377.

[79] J. P. Perdew, W. Yue. Accurate and simple density functional for the electronic exchange energy: Generalized gradient approximation. *Physical Review B* **1986**, *33*, 8800–8802.

[80] J. P. Perdew, K. Burke, M. Ernzerhof. Generalized gradient approximation made simple. *Physical Review Letters* **1996**, *77*, 3865–3868.

[81] C. Lee, W. Yang, R. G. Parr. Development of the colle-salvetti correlation-energy formula into a functional of the electron density. *Physical Review B* **1988**, *37*, 785–789.

[82] M. Iannuzzi, F. Tran, R. Widmer, T. Dienel, K. Radican, Y. Ding, J. Hutter, O. Gröning. Site-selective adsorption of phthalocyanine on h-BN/Rh(111) nanomesh. *Physical Chemistry Chemical Physics* **2014**, *16*, 12374–12384.

[83] N. V. Skorodumova, R. Ahuja, S. I. Simak, I. A. Abrikosov, B. Johansson, B. I. Lundqvist. Electronic, bonding, and optical properties of CeO_2 and Ce_2O_3 from first principles. *Physical Review B* **2001**, *64*, 115108–115116.

[84] M. V. Ganduglia-Pirovano, J. L. F. Da Silva, J. Sauer. Density-functional calculations of the structure of near-surface oxygen vacancies and electron localization on ceo$_2$(111). *Physical Review Letters* **2009**, *102*, 026101–026104.

[85] R. Evarestov, Y. Zhukovskii. Four-faceted nanowires generated from densely-packed TiO_2 rutile surfaces: Ab initio calculations . *Surface Science* **2013**, *608*, 226–240.

[86] L. Kavan, M. Grätzel, S. E. Gilbert, C. Klemenz, H. J. Scheel. Electrochemical and Photoelectrochemical Investigation of Single-Crystal Anatase. *Journal of the American Chemical Society* **1996**, *118*, 6716–6723.

[87] Y. Gurdal, S. Luber, J. Hutter, M. Iannuzzi. Non-innocent adsorption of Co-pyrphyrin on rutile(110). *Physical Chemistry Chemical Physics* **2015**, *17*, 22846–22854.

[88] J. C. Slater. A simplification of the hartree-fock method. *Physical Review* **1951**, *81*, 385–390.

[89] J. L. F. Da Silva, M. V. Ganduglia-Pirovano, J. Sauer, V. Bayer, G. Kresse. Hybrid functionals applied to rare-earth oxides: The example of ceria. *Physical Review B* **2007**, *75*, 045121–045130.

[90] J. Heyd, G. E. Scuseria, M. Ernzerhof. Hybrid functionals based on a screened Coulomb potential. *The Journal of Chemical Physics* **2003**, *118*, 8207–8215.

[91] A. V. Krukau, O. A. Vydrov, A. F. Izmaylov, G. E. Scuseria. Influence of the exchange screening parameter on the performance of screened hybrid functionals. *The Journal of Chemical Physics* **2006**, *125*, 224106–224110.

[92] M. Ernzerhof, G. E. Scuseria. Assessment of the perdew–burke–ernzerhof exchange-correlation functional. *The Journal of Chemical Physics* **1999**, *110*, 5029–5036.

[93] T. L. Bahers, M. Rérat, P. Sautet. Semiconductors Used in Photovoltaic and Photocatalytic Devices: Assessing Fundamental Properties from DFT. *The Journal of Physical Chemistry C* **2014**, *118*, 5997–6008.

[94] F. Ambrosio, G. Miceli, A. Pasquarello. Redox levels in aqueous solution: Effect of van der waals interactions and hybrid functionals. *The Journal of Chemical Physics* **2015**, *143*, 244508–244522.

[95] F. Schiffmann, J. VandeVondele, J. Hutter, R. Wirz, A. Urakawa, A. Baiker. Protonation-Dependent Binding of Ruthenium Bipyridyl Complexes to the Anatase(101) Surface. *The Journal of Physical Chemistry C* **2010**, *114*, 8398–

8404.

[96] S. Grimme, J. Antony, S. Ehrlich, H. Krieg. A consistent and accurate ab initio parametrization of density functional dispersion correction (DFT-D) for the 94 elements H-Pu. *The Journal of Chemical Physics* **2010**, *132*, 154104–154122.

[97] F. Tran, J. Hutter. Nonlocal van der Waals functionals: The case of rare-gas dimers and solids. *The Journal of Chemical Physics* **2013**, *138*, 204103–204111.

[98] O. A. Vydrov, T. Van Voorhis. Nonlocal van der waals density functional made simple. *Physical Review Letters* **2009**, *103*, 63004–63007.

[99] R. Sabatini, T. Gorni, S. de Gironcoli. Nonlocal van der waals density functional made simple and efficient. *Physical Review B* **2013**, *87*, 41108–41111.

[100] M. Dion, H. Rydberg, E. Schröder, D. C. Langreth, B. I. Lundqvist. Van der waals density functional for general geometries. *Physical Review Letters* **2004**, *92*, 246401–246404.

[101] O. A. Vydrov, T. V. Voorhis. Nonlocal van der waals density functional: The simpler the better. *The Journal of Chemical Physics* **2010**, *133*, 244103–244111.

[102] J. Tersoff, D. R. Hamann. Theory of the scanning tunneling microscope. *Physical Review B* **1985**, *31*, 805–813.

[103] D. Marx, J. Hutter. *Ab initio molecular dynamics*. Cambridge University Press, 2009.

[104] R. N. Barnett, U. Landman. Born-oppenheimer molecular-dynamics simulations of finite systems: Structure and dynamics of $(h_2o)_2$. *Physical Review B* **1993**, *48*, 2081–2097.

[105] A. Laio, M. Parrinello. Escaping free-energy minima. *Proceedings of the National Academy of Sciences* **2002**, *99*, 12562–12566.

[106] R. Koitz, J. Hutter, M. Iannuzzi. Formation and properties of a terpyridine-based 2d mof on the surface of water. *2D Materials* **2016**, *3*, 25026–25031.

[107] L. A. Harris, A. A. Quong. Molecular chemisorption as the theoretically preferred pathway for water adsorption on ideal rutile $tio_2(110)$. *Physical Review Letters* **2004**, *93*, 86105–86108.

[108] J. Wilhelm, P. Seewald, M. Del Ben, J. Hutter. Large-scale cubic-scaling random phase approximation correlation energy calculations using a gaussian basis. *Journal of Chemical Theory and Computation* **2016**, *12*, 5851–5859.

[109] H. Xu, R. Q. Zhang, A. M. C. Ng, A. B. Djurišić, H. T. Chan, W. K. Chan, S. Y. Tong. Splitting water on metal oxide surfaces. *The Journal of Physical*

Chemistry C **2011**, *115*, 19710–19715.

[110] Y. Gurdal, J. Hutter, M. Iannuzzi. How coordination pocket and ligand type affect the water reduction mechanism of Cobalt-based polypyridyl catalysts. In preparation, 2017.

[111] J. VandeVondele, M. Krack, F. Mohamed, M. Parrinello, T. Chassaing, J. Hutter. Quickstep: Fast and accurate density functional calculations using a mixed Gaussian and plane waves approach . *Computer Physics Communications* **2005**, *167*, 103–128.

[112] S. Goedecker, M. Teter, J. Hutter. Separable dual-space gaussian pseudopotentials. *Physical Review B* **1996**, *54*, 1703–1710.

[113] J. VandeVondele, J. Hutter. Gaussian basis sets for accurate calculations on molecular systems in gas and condensed phases. *The Journal of Chemical Physics* **2007**, *127*, 114105–114113.

[114] G. Bussi, D. Donadio, M. Parrinello. Canonical sampling through velocity rescaling. *The Journal of Chemical Physics* **2007**, *126*, 14101–14107.

[115] J. Blumberger, L. Bernasconi, I. Tavernelli, R. Vuilleumier, M. Sprik. Electronic structure and solvation of copper and silver ions: A theoretical picture of a model aqueous redox reaction. *Journal of American Chemical Society* **2004**, *126*, 3928–3938.

[116] F. Ambrosio, G. Miceli, A. Pasquarello. Structural, dynamical, and electronic properties of liquid water: A hybrid functional study. *The Journal of Physical Chemistry B* **2016**, *120*, 7456–7470.

[117] M. Guidon, J. Hutter, J. VandeVondele. Auxiliary Density Matrix Methods for Hartree–Fock Exchange Calculations. *Journal of Chemical Theory and Computation* **2010**, *6*, 2348–2364.

[118] M. Guidon, J. Hutter, J. VandeVondele. Robust Periodic Hartree–Fock Exchange for Large-Scale Simulations Using Gaussian Basis Sets. *Journal of Chemical Theory and Computation* **2009**, *5*, 3010–3021.

[119] M. Guidon, F. Schiffmann, J. Hutter, J. VandeVondele. Ab initio molecular dynamics using hybrid density functionals. *The Journal of Chemical Physics* **2008**, *128*, 214104–214118.

[120] J. Cheng, M. Sulpizi, M. Sprik. Redox potentials and pKa for benzoquinone from density functional theory based molecular dynamics. *The Journal of Chemical Physics* **2009**, *131*, 154504–154523.

[121] M. Del Ben, M. Schönherr, J. Hutter, J. VandeVondele. Bulk liquid water at ambient temperature and pressure from MP2 theory. *The Journal of Physical Chemistry Letters* **2013**, *4*, 3753–3759.

[122] P. L. Silvestrelli, M. Parrinello. Structural, electronic, and bonding properties of liquid water from first principles. *The Journal of Chemical Physics* **1999**, *111*, 3572–3580.

[123] K. Laasonen, M. Sprik, M. Parrinello, R. Car. "Ab initio" liquid water. *The Journal of Chemical Physics* **1993**, *99*, 9080–9089.

[124] L. B. Skinner, C. Huang, D. Schlesinger, L. G. M. Pettersson, A. Nilsson, C. J. Benmore. Benchmark oxygen-oxygen pair-distribution function of ambient water from X-ray diffraction measurements with a wide Q-range. *The Journal of Chemical Physics* **2013**, *138*, 74506–74517.

[125] M. E. Tuckerman. *Statistical mechanics: Theory and molecular simulation.* Oxford University Press, 2010.

[126] J. Blumberger, I. Tavernelli, M. L. Klein, M. Sprik. Diabatic free energy curves and coordination fluctuations for the aqueous Ag^{+}/Ag^{2+} redox couple: A biased Born-Oppenheimer molecular dynamics investigation. *The Journal of Chemical Physics* **2006**, *124*, 64507–64518.

[127] J. Cheng, X. Liu, J. VandeVondele, M. Sulpizi, M. Sprik. Redox potentials and acidity constants from density functional theory based molecular dynamics. *Accounts of Chemical Research* **2014**, *47*, 3522–3529.

[128] J. Blumberger, M. Sprik. Quantum versus classical electron transfer energy as reaction coordinate for the aqueous Ru^{2+}/Ru^{3+} redox reaction. *Theoretical Chemistry Accounts* **2006**, *115*, 113–126.

[129] F. H. Hodel, S. Luber. Dehydrogenation free energy of Co^{2+}(aq) from density functional theory-based molecular dynamics. *Journal of Chemical Theory and Computation* **2017**, *13*, 974–981.

[130] Y. Gurdal, M. Iannuzzi. DFT-based theoretical simulations for photocatalytic applications using TiO_2. In Titanium Dioxide, Editor: M. Janus, INTECH publishing, accepted, 2017.

[131] Luttrell Tim, Halpegamage Sandamali, Tao Junguang, Kramer Alan, Sutter Eli, Batzill Matthias. Why is anatase a better photocatalyst than rutile? - Model studies on epitaxial TiO_2 films. *Scientific Reports* **2014**, *4*, 4043–4050.

[132] J. Chen, Y.-F. Li, P. Sit, A. Selloni. Chemical Dynamics of the First Proton-Coupled Electron Transfer of Water Oxidation on TiO_2 Anatase. *Journal of the American Chemical Society* **2013**, *135*, 18774–18777.

[133] A. G. Thomas, K. L. Syres. Adsorption of organic molecules on rutile TiO_2 and anatase TiO_2 single crystal surfaces. *Chemical Society Reviews* **2012**, *41*, 4207–4217.

[134] A. J. Cohen, P. Mori-Sánchez, W. Yang. Insights into current limitations of density functional theory. *Science* **2008**, *321*, 792–794.

[135] J. Muscat, V. Swamy, N. M. Harrison. First-principles calculations of the phase stability of tio$_2$. *Physical Review B* **2002**, *65*, 224112–224126.

[136] F. Labat, P. Baranek, C. Adamo. Structural and Electronic Properties of Selected Rutile and Anatase TiO_2 Surfaces: An ab Initio Investigation. *Journal of Chemical Theory and Computation* **2008**, *4*, 341–352.

[137] H. Xiao, J. Tahir-Kheli, W. A. Goddard. Accurate Band Gaps for Semiconductors from Density Functional Theory. *The Journal of Physical Chemistry Letters* **2011**, *2*, 212–217.

[138] C. J. Howard, T. M. Sabine, F. Dickson. Structural and thermal parameters for rutile and anatase. *Acta Crystallographica Section B* **1991**, *47*, 462–468.

[139] J. K. Burdett, T. Hughbanks, G. J. Miller, J. W. Richardson, J. V. Smith. Structural-electronic relationships in inorganic solids: Powder neutron diffraction studies of the rutile and anatase polymorphs of titanium dioxide at 15 and 295 K. *Journal of the American Chemical Society* **1987**, *109*, 3639–3646.

[140] H. Perron, J. Vandenborre, C. Domain, R. Drot, J. Roques, E. Simoni, J. J. Ehrhardt, H. Catalette. Combined investigation of water sorption on TiO_2 rutile (110) single crystal face: XPS vs. periodic DFT . *Surface Science* **2007**, *601*, 518–527.

[141] H. Perron, C. Domain, J. Roques, R. Drot, E. Simoni, H. Catalette. Optimisation of accurate rutile TiO_2 (110), (100), (101) and (001) surface models from periodic DFT calculations. *Theoretical Chemistry Accounts* **2007**, *117*, 565–574.

[142] U. Diebold. The surface science of titanium dioxide . *Surface Science Reports* **2003**, *48*, 53–229.

[143] C. Lun Pang, R. Lindsay, G. Thornton. Chemical reactions on rutile TiO_2(110). *Chemical Society Reviews* **2008**, *37*, 2328–2353.

[144] S.-C. Li, U. Diebold. Reactivity of TiO_2 Rutile and Anatase Surfaces toward Nitroaromatics. *Journal of the American Chemical Society* **2010**, *132*, 64–66.

[145] T. R. Esch, I. Gadaczek, T. Bredow. Surface structures and thermodynamics of low-index of rutile, brookite and anatase – A comparative DFT study. *Applied Surface Science* **2014**, *288*, 275–287.

[146] S. Fujiyoshi, T.-A. Ishibashi, H. Onishi. Fourth-Order Raman Spectroscopy of Wide-Band Gap Materials. *The Journal of Physical Chemistry B* **2005**, *109*, 8557–8561.

[147] A. T. Paxton, L. Thiên-Nga. Electronic structure of reduced titanium dioxide. *Physical Review B* **1998**, *57*, 1579–1584.

[148] L.-H. Han, C.-R. Zhang, J.-W. Zhe, N.-Z. Jin, Y.-L. Shen, W. Wang, J.-J. Gong, Y.-H. Chen, Z.-J. Liu. Understanding the electronic structures and absorption properties of porphyrin sensitizers YD2 and YD2-o-C8 for dye-sensitized solar cells. *International Journal of Molecular Sciences* **2013**, *14*, 20171–20188.

[149] S. Suzuki, Y. Yamaguchi, H. Onishi, T. Sasaki, K. Fukui, Yasuhiro Iwasawa. Study of pyridine and its derivatives adsorbed on a TiO_2(110)-(1×1)surface by means of STM, TDS, XPS and MD calculation in relation to surface acid/base interaction. *Journal Chemical Society, Faraday Transactions* **1998**, *94*, 161–166.

[150] S. M. Pratik, A. Datta. Computational design of concomitant type-I and type-II porphyrin sensitized solar cells. *Physical Chemistry Chemical Physics* **2013**, *15*, 18471–18481.

[151] G. Lovat, D. Forrer, M. Abadia, M. Dominguez, M. Casarin, C. Rogero, A. Vittadini, L. Floreano. Hydrogen capture by porphyrins at the TiO_2(110) surface. *Physical Chemistry Chemical Physics* **2015**, *17*, 30119–30124.

[152] R. F. W. Bader, C. F. Matta. Atomic charges are measurable quantum expectation values: A rebuttal of criticisms of qtaim charges. *The Journal of Physical Chemistry A* **2004**, *108*, 8385–8394.

[153] N. Ishida, D. Fujita. Adsorption of Co-Phthalocyanine on the rutile TiO_2(110) surface: A scanning tunneling microscopy/spectroscopy study. *The Journal of Physical Chemistry C* **2012**, *116*, 20300–20305.

[154] Y. Gurdal, J. Hutter, M. Iannuzzi. Insight into (Co)Pyrphyrin Adsorption on Au(111): Effects of Herringbone Reconstruction and Dynamics of Metalation. *The Journal of Physical Chemistry C* **2017**, *121*, 11416–11427.

[155] Y. Wang, N. S. Hush, J. R. Reimers. Simulation of the Au(111)-(22 × $\sqrt{3}$) surface reconstruction. *Physical Review B* **2007**, *75*, 233416–233419.

[156] M. El-Batanouny, S. Burdick, K. M. Martini, P. Stancioff. Double-sine-gordon solitons: A model for misfit dislocations on the au(111) reconstructed surface. *Physical Review Letters* **1987**, *58*, 2762–2765.

[157] R. Ravelo, M. El-Batanouny. Molecular-dynamics study of the reconstructed au(111) surface: Low temperature. *Physical Review B* **1989**, *40*, 9574–9589.

[158] N. Takeuchi, C. T. Chan, K. M. Ho. Au(111): A theoretical study of the surface reconstruction and the surface electronic structure. *Physical Review B* **1991**, *43*, 13899–13906.

[159] F. Reinert, G. Nicolay. Influence of the herringbone reconstruction on the surface electronic structure of au(111). *Applied Physics A* **2004**, *78*, 817–821.

[160] U. Tartaglino, E. Tosatti, D. Passerone, F. Ercolessi. Bending strain-driven modification of surface reconstructions: Au(111). *Physical Review B* **2002**, *65*, 241406–241409.

[161] R. Gaspari, C. A. Pignedoli, R. Fasel, M. Treier, D. Passerone. Atomistic insight into the adsorption site selectivity of stepped au(111) surfaces. *Physical Review B* **2010**, *82*, 41408–41411.

[162] Y. Bai, M. Sekita, M. Schmid, T. Bischof, H.-P. Steinruck, J. M. Gottfried. Interfacial coordination interactions studied on cobalt octaethylporphyrin and cobalt tetraphenylporphyrin monolayers on Au(111). *Physical Chemistry Chemical Physics* **2010**, *12*, 4336–4344.

[163] J. Hutter, M. Iannuzzi, F. Schiffmann, J. VandeVondele. CP2K: atomistic simulations of condensed matter systems. *Wiley Interdisciplinary Reviews: Computational Molecular Science* **2014**, *4*, 15–25.

[164] F. Hanke, J. Björk. Structure and local reactivity of the Au(111) surface reconstruction. *Physical Review B* **2013**, *87*, 235422–235427.

[165] D. A. Egger, Z.-F. Liu, J. B. Neaton, L. Kronik. Reliable Energy Level Alignment at Physisorbed Molecule-Metal Interfaces from Density Functional Theory. *Nano Letters* **2015**, *15*, 2448–2455.

[166] Y. Wang, N. S. Hush, J. R. Reimers. Simulation of the Au(111)-(22 × $\sqrt{3}$) surface reconstruction. *Physical Review B* **2007**, *75*, 233416–233419.

[167] W. Chen, V. Madhavan, T. Jamneala, M. F. Crommie. Scanning tunneling microscopy observation of an electronic superlattice at the surface of clean gold.

Physical Review Letters **1998**, *80*, 1469–1472.

[168] Ž. Crljen, P. Lazić, D. Šokčević, R. Brako. Relaxation and reconstruction on (111) surfaces of Au, Pt, and Cu. *Physical Review B* **2003**, *68*, 195411–195418.

[169] J. C. Boettger. Nonconvergence of surface energies obtained from thin-film calculations. *Physical Review B* **1994**, *49*, 16798–16800.

[170] V. Fiorentini, M. Methfessel. Extracting convergent surface energies from slab calculations. *Journal of Physics: Condensed Matter* **1996**, *8*, 6525–6529.

[171] T. E. Shubina, H. Marbach, K. Flechtner, A. Kretschmann, N. Jux, F. Buchner, H. P. Steinrück, T. Clark, J. M. Gottfried. Principle and mechanism of direct porphyrin metalation: Joint experimental and theoretical investigation. *Journal of the American Chemical Society* **2007**, *129*, 9476–9483.